Development of a Feasible Elastography Framework for Portable Ultrasound

by

Bonghun Shin

A thesis
presented to the University of Waterloo
in fulfillment of the
thesis requirement for the degree of
Doctor of Philosophy
in
Mechanical and Mechatronics Engineering

Waterloo, Ontario, Canada, 2017

Examining Committee Membership

The following served on the Examining Committee for this thesis. The decision of the Examining Committee is by majority vote.

External Examiner	Il Yong Kim Professor
Co-supervisor	Hyock Ju Kwon Professor
Co-supervisor	Soo Jeon Professor
Internal Member	John Medley Professor
Internal Member	Baris Fidan Professor
Internal-external Member	Youngki Yoon Professor

I hereby declare that I am the sole author of this thesis. This is a true copy of the thesis, including any required final revisions, as accepted by my examiners.

I understand that my thesis may be made electronically available to the public.

Abstract

Portable wireless ultrasound is emerging as a new ultrasound device due to the advantages such as small size, lightweight and affordable price. Its high portability allows practitioners to make diagnostic and therapeutic decisions in real-time without having to take the patients out of their environment. Recent portable ultrasound devices are equipped with sophisticated processors and image processing algorithms providing high image quality. Some of them are able to deliver multiple ultrasound modes including color Doppler, echocardiography, and endovaginal examination. Nevertheless, they are still lack of elastography functions due to the limitations in computational performance and data transfer speed via wireless communication. In order to implement the elastography function in the wireless portable ultrasound devices, this thesis proposes a new strain estimation method to significantly reduce the computation time and a compressive sensing framework to minimize the data transfer size.

Firstly, a robust phase-based strain estimator (RPSE) is developed to overcome the limited hardware performance of portable ultrasound. The RPSE is not only computationally efficient but also robust to variations of the speed of sound, sampling frequency and pulse repetition. The RPSE has been compared with other representative strain estimators including time-delay, displacement-gradient, and conventional phase-based strain estimators (TSE, DSE and PSE, respectively). It has been shown that the RPSE is superior in several elastographic image quality measures, including signal-to-noise (SNRe) and contrast-to-noise (CNRe), and the computational efficiency. The study indicates that the RPSE method can deliver the acceptable level of elastography and fast computational speed for the ultrasound echo data sets from the numerical and experimental phantoms. According to the results from the numerical phantom experiment, RPSE can achieve highest values of SNRe and CNRe (around 5.22 and 47.62 dB) among all strain estimators tested, and almost 100 times higher computational efficiency than TSE and DSE (around 0.06 vs. 5.76 seconds per frame for RPSE and TSE, respectively).

Secondly, as a means to reduce the large amount of ultrasound measurement data that has to be transmitted via wireless communication, the compressive sensing (CS) framework has been applied to elastography. The performance of CS is highly dependent on the

selection of model basis to represent the sparse expansion as well as the reconstruction algorithm to recover the original data from the compressed signal. Therefore, it is essential to compose the optimal combination of model basis and reconstruction algorithm for CS framework to achieve the best CS performance in terms of image quality and the maximum data reduction. In this thesis, three model bases, discrete Fourier transform (FT), discrete cosine transform (DCT), and wave atoms (WA), along with two reconstruction algorithms, L1 minimization (L1) and Block sparse Bayesian learning (BSBL) are tested. Using B-mode and elastogram images of simulated numerical phantoms, the quality of CS reconstruction is assessed in terms of three image quality measures, mean absolute error (MAE), SNRe, and CNRe, at varying data reduction (subsampling) rates. The results illustrate that BSBL-based CS frameworks can generally deliver much higher image quality and subsampling rate compared with L1-based ones. In particular, the CS frameworks adopting DCT and BSBL offer the best CS performance. The results also suggests that the maximum subsampling rates without causing image degradation are 40% for L1-based framework and 60% for BSBL-based framework, respectively.

The contributions of this thesis help realize elastography functionality in portable ultrasound, thereby significantly expanding its utility. For example, the diagnosis of malignant lesions, even when a patient cannot be moved to hospital immediately, is possible with the portable ultrasound. Furthermore, the SPSE method and the CS framework can be individually employed for the conventional ultrasound device as well as other telemedicine applications, to enhance computational efficiency and image quality.

Acknowledgements

I would like to express my deepest gratitude to my supervisors: Professor Hyock Ju Kwon and Professor Soo Jeon who gave me the opportunity to work their lab, and to work in such an interesting bio-medical research field. Particularly, their support and guidance through the PhD study was instrumental to my research. I would like to thank the other members of my committee - Professor John Medley, Professor Baris Fidan, Professor Youngki Yoon, and Professor Il-yong Kim - for serving on my comprehensive examination committee and final defense committee, reviewing my thesis as well as giving helpful comments and suggestions. I am indebted to Professor Il-yong Kim, who agreed to travel to Waterloo to attend my defense in person, given his busy schedule.

Life as a PhD student would be so difficult without friends and lab mates, even though PhD study itself is doing research individually. Sincere thanks go out to my friends and colleagues at the office: Hyunki, Jiwon, Ku-Jin, Shiyi, Yajun, and Moslem. Especially, I would like to thank Hyunki and Jiwon who shared their ideas and friendship. I would also like to offer gratitude to my project supports at Healcerion Inc: Su-yeol Lee and Dr. Jeong-won Ryu who shared their experience and taught me how to measure the raw RF echo signal from the portable ultrasound device. Special thanks to Dr. Sangtak Park who gave me advice about my career planning. In addition, I want to thank Albert Chen for teaching me what the ultrasound hardware system is at the first stage of this study.

Finally, I would like to thank my four lovely children: Chaehong, Chaelin, Yule, and Chaeha, for showing me your great smiles and happiness during my PhD study. I would like to express my appreciation to my graceful wife, Jeongsoon, for her unconditional love, moral support, and understanding. I would not have been able to make this achievement far without your love and support.

Table of Contents

List of Tables

List of Figures

Nomenclature

ACM	Angular correlation method
BO	Bound optimization
BP	Basis pursuit
BSBL	Block sparse Bayesian Learning
CAM	Combined autocorrelation method
CNRe	Elastographic contrast-to-noise ratio
CS	Compressive sensing
CT	Computed tomography
DIC	Digital image correlation
DCT	Discrete cosine transform
DSE	Displacement-based strain estimation
ECG	Electrocardiogam
FEA	Finite element analysis
FNCC	Fast normalized cross-correlation
FT	Discrete Fourier transform
MAE	Mean absolute eroor
MAP	Maximum a posteriori
MRI	Magnetic resonance imaging
NCC	Normalized cross-correlation
NP-24	Numerical phantom for a portable ultrasound device with 24 active elements
NP-64	Numerical phantom for a conventional ultrasound device with 64 active elements
PAT	Photoacoustic tomography

PRS	Phase root seeking
PSE	Phase-based strain estimation
RIP	Restrict isometry property
RF	Radio frequency echo signal
SAD	Sum of absolute differences
SNRe	Elastographic signal-to-noise ratio
SPSE	Simple phase-based strain estimation
SR	Subsampling rate (or data compression rate)
SSD	Sum of squared differences
Sub-sample	between samples; a fraction of the sample spacing
TSE	Time-based strain estimation
WA	Wave atoms transform

Chapter 1

Introduction and Background

1.1 Elastography

Ultrasound elastography has emerged as a noninvasive screening modality to detect and classify pathological lesions by visualizing mechanical properties of soft biological tissues. Using the palpation principle that pathological lesions are stiffer than benign tissues under compression [1] (Table 1.1), elastography facilitates precise detection of malignant lesions in various soft biological tissues i.e., breast, prostate, thyroid, etc.

In 1991, Ophir et al. [2] introduced a compression elastography utilizing a comparison of ultrasound radio-frequency data sets from a tissue before and after a modest compression. The principle of the elastography is based on the stress-strain relationship under a simple uniaxial (one-dimensional) displacement [3]. Figure 1.1 illustrates the typical ultrasound elastography process. Biological tissues examined by the elastography are modeled as a series of springs (Figure 1.1(a)). When an ultrasound probe is moved slightly up and down (Figure 1.1(b)), deformation in the gray circle (hard spring) is relatively smaller than those in the surrounding materials (soft spring). Due to the different deformations in hard and soft tissues, displacements (shift of the spring) are induced in the tissues (Figure 1.1(c)). The displacements are estimated by comparing the echo data sets between pre- and post-compression by using correlation methods (Figure 1.1(c), left). The strain is the

slope of the displacement (Figure 1.1(c), middle), and the field of the strain is displayed as color-coded strain map (Figure 1.1(c), right). This process is illustrated in Figure 1.1(c).

Since elastography can quantitatively visualize mechanical properties of soft biological tissues, stiffness of the tissue measured by elastography can offer more accurate clinical information than conventional manual palpation. Thus, elastography is popularly used as a new screening method for detecting malignant lesions in breast [2, 4, 5, 6, 7, 8, 9] and prostate [10, 11, 12], as well as for providing various clinical Information. It is also useful to monitor thermal changes and ablation [13], to assess tendon motion [14], and to measure the stiffness of muscle and tendon [15, 16]. The high resolution strain image generated by elastography is called the elastograms [9]. The elastogram generally depicts the axial or lateral strains that are useful in various clinical applications described above.

Table 1.1: Young's modulus of breast tissue (unit: kPa)(Krouskop et al. 1998)

Breast Tissue Type	5% compression		20% compression	
	0.1 Hz	1.0 Hz	0.1 Hz	1.0 Hz
Normal tissue	18±7	19±7	20±8	20±6
Normal glandular tissue	28±14	33±11	48±15	57±19
Fibrous tissue	96±34	107±31	218±87	232±60
Ductal carcinoma in situ	22±8	25±4	291±67	301±58
Invasive and infiltrating ductal carcinoma	106±32	93±33	558±108	490±112

1.2 Portable Ultrasound

Recently, portable ultrasound is emerging as a new ultrasound device that is much smaller and lighter than the conventional console style ultrasound machines (Figure 1.2). Its high portability and durability allow practitioners to make diagnostic and therapeutic decisions in real-time without having to take the patients out of their environment, which makes the portable ultrasound an attractive medical modality particularly for harsh and remote sites [17].

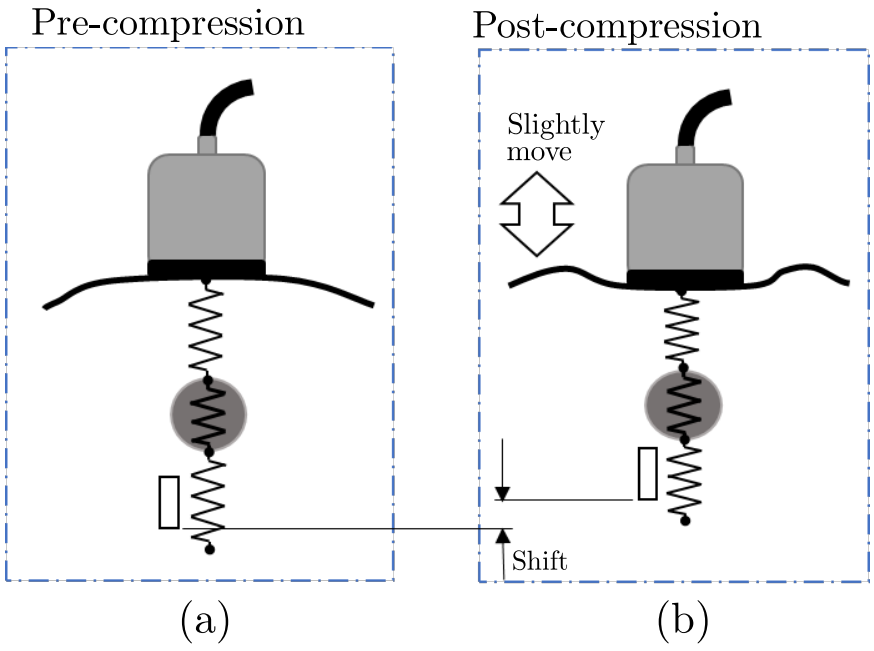

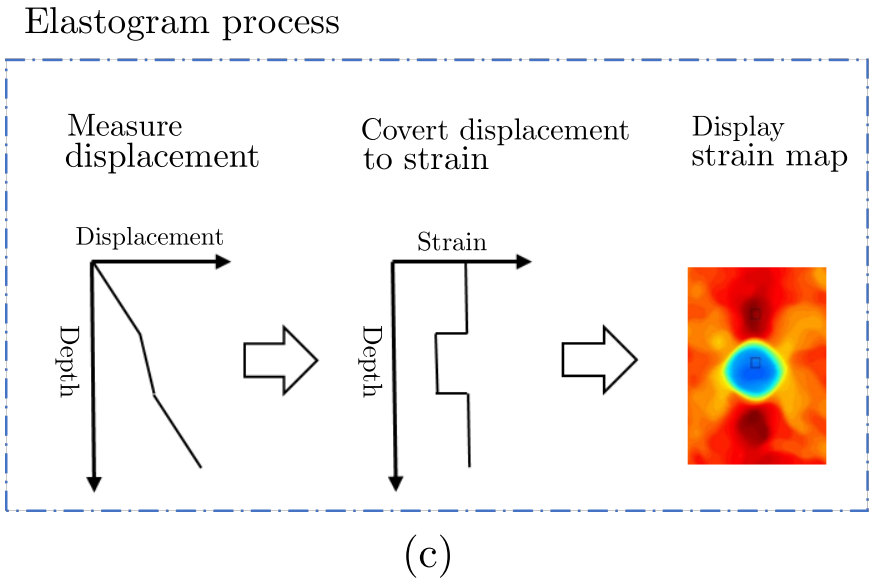

Figure 1.1: Schematic of a typical elastography process

In the early 1960s, the first direct contact ultrasound transducer was developed; however, it was difficult to maneuver into desirable views of the organ due to the rigid arm. In the mid-1970s, this limitation was overcome by using transducers with flexible cable. Later on real-time dynamic scanning was realized through the 1970s and the 1980s. More compact, portable ultrasound machines were first introduced in the 1980s; however, they were not adequate to be used in austere or remote environment. In February 1995, the U.S. Defense Advanced Research Project Administration (DARPA) had launched a two-year program to develop a highly portable ultrasound device for use on the battlefield or in natural or man-made disasters to diagnose victims of severe trauma. Through this program, SonoSight (now FUJIFILM SonoSite) and its research collaborators developed a prototype of the first handheld ultrasound device for both medical field and military purpose [18]. Until the late 1990s many other companies also began implementing general purpose portable ultrasound devices.

The modern portable ultrasound devices and their weight are summarized in Table 1.2. Typically the weight of portable ultrasound devices are under 2.7 kg, and they are often the size of a laptop computer or smaller, or can be hand-carried to the patient's beside in or out of hospital environment. These lightweight units, therefore, now have attractive uses in wide range including prehospital, austere and remote ultrasound. Prehospital ultrasound has been being increasingly adopted in North America and around the world with a continuously growing list of diagnostic applications [19]. The enhanced technology enables prehospital professionals to answer focused clinical questions, which translate into faster and more accurate diagnosis and care of patients presenting with time-sensitive emergency conditions. In austere sites, ultrasound may be the only available imaging modality; therefore, it can be used to rapidly assess patients during triage and evacuation decision making. Ultrasound performs well in the diverse environments of space, swamp, jungle, mountain, and desert [20]. Telemedicine is the most cutting edge applications of portable ultrasound. In telemedicine, the obtained ultrasound images can be transmitted via satellite and cellular transmission. This technology can be a powerful tool to increase the expert's efficiency because it delivers pictures, movies and other information to the experts; thus, avoiding the need of bringing the expert to the information [17].

Figure 1.2: A portable ultrasound with mobile phone (Sonon 300C, Healcerion Inc., Korea)

Table 1.2: Portable ultrasound devices

Model	Manufacturer	Weight
SonoSite 180	FUJIFILM (Bothell, WA, USA)	2.4 kg
SonoSite 180PLUS	FUJIFILM (Bothell, WA, USA)	2.4 kg
SonoSite Elite	FUJIFILM (Bothell, WA, USA)	2.6 kg
SonoSite SonoHeart	FUJIFILM (Bothell, WA, USA)	2.4 kg
Philips Optigo	Philips (Andover, MA, USA)	3.4 kg
Agilent Optigo	Philips (Andover, MA, USA)	2.5 kg
GE V Scan	GE Healthcare (Little Chalfont, UK)	0.39 kg
Micros Q.V.	Advanced Medical System (Banbury, UK)	0.9 kg
Primedic Handyscan	Metrax GmbH (Rottweil,Germany)	2.2 kg
Esoate Tringa Linear VET	Esoate (Genova,Italy)	0.8 kg
Sonon 300C	Healcerion (Seoul, Korea)	0.39 kg

1.3 Motivation and Challenges

Despite recent portable ultrasound devices capable of offering high image quality and multiple ultrasound modes, none of them offers elastography function, mainly due to the limitations of hardware performance and data transfer speed via wireless communication.

Particularly, a typical strain estimation process using signal correspondence function and elastographic image processing requires high computational complexity, which is hard to achieve in portable ultrasound devices. Note that conventional console style ultrasound device performs the considerable amount of computation for elastography function using its own hardware system that is specially designed to process the substantial data acquisition (i.e. 192 channels of echo data with 28 MHz sampling rate) and sophisticated image processing procedures. However, portable ultrasound devices cannot carry out such data processing computation using a dedicated computing hardware. To compensate for the limited system performance insufficient for the sizable computation, portable ultrasound devices utilize a wireless-connected mobile device or laptop computer. Although computation power of modern general purpose computers has been being increased rapidly, it cannot be compared to that of dedicated hardware.

In addition, the wireless data transfer speed of the portable devices is insufficient to deliver a large amount of raw ultrasound RF echo data set for the ultrasound elastography computation. One of the reasons requiring large amount of data measurement in conventional ultrasound is to illustrate more precise image for facilitating accurate medical diagnosis. For that reason, ultrasound sampling rate of conventional ultrasound devices is typically over 4 times larger than that of the minimum requirement by Shannon-Hartley theorem: the sampling rate must be at least twice the maximum frequency presented in the recorded signal. Note that the raw RF echo data for one B-mode image with 50 mm depth has 128 A-lines $\times$ 1,819 samples at 28 MHz sampling rate. In that case, the transmitted ultrasound data size is approximately over 14 Mbit/frame; thus, the wireless data communication speed using IEEE 802.11b/g/n protocol whose data transfer rate are 11, 54, 72 Mbit/s, respectively, might be insufficient to generate the real-time elastograms requiring 10 to 15 frame/sec.

1.4 Thesis Contributions

The principal research objective is to accomplish the elastography function in the portable ultrasound device without significantly improving or changing the hardware system. In doing so, the thesis has developed a new computationally efficient strain estimation method and proposed a feasible compressive sensing framework to reduce the data transfer size. These new approaches are intended to overcome two challenges caused by high computational complexity of strain estimation algorithm and large amount of the ultrasound data.

Specially, the thesis makes the following main contributions:

- Robust Phase-based Strain Estimation Algorithm

  A new phase-based strain estimation that is computationally efficient and robust to variations of speed of sound and sampling interval has been developed, implemented, and tested. This is described in detail in Chapter 3 after a concise overview of the current literature in Chapter 2.

- Compressive Sensing Framework for Elastography

  A feasible compressive sensing framework to reduce the large amount of raw ultrasound echo data for elastography, has been proposed and tested. This is described in detail in Chapter 5 after a concise overview of the current literature in Chapter 4.

Chapter 2

Overview of Elastography

2.1 Ultrasound Imaging

General background on ultrasound imaging is introduced to help readers understand the medical ultrasound imaging, before describing ultrasound elastography. Ultrasonics is the science of elastic waves in solids, liquids, and gases which have high frequencies above 20 kHz (the nominal limit of human hearing). Ultrasonics has been applied to various fields including industrial and medical applications. In industry, it is commonly used to detect a defect which is either a discrete feature of an object such as a crack or a region of faulty material [21]. Ultrasound medical imaging, generally called diagnostic sonography, is used for evaluating the condition of internal organs and tissues, imaging internal body structures, and measuring blood flow. In ultrasound medical imaging, the transmitted ultrasound signals, ranging from 1 MHz to 18 MHz, generated by a ultrasonic transducer with multiple piezoelectric elements are propagated into the image field. The echoes partially reflected by the objects in the image field are received by the same ultrasound transducer. The received acoustic echo signals are transformed back to electrical signals. After receiving the electrical signals from the image field, several signal processing techniques including beamforming filter, interpolation, log compression, contrast enhancement, speckle reduction are often used to produce more clearer echo fields [22].

Ultrasound medical imaging offers several different types of images. B-mode ultrasound

displays the acoustic impedance of a two-dimensional cross-section of tissue and is the most commonly used operation mode. C-mode ultrasound (or color Doppler imaging) combines anatomical information derived by ultrasonic pulse-echo techniques with velocity information from ultrasonic Doppler techniques to generate color-coded maps of tissue velocity superimposed on grey-scale image of tissue anatomy [23]. The most common use of C-mode ultrasound is to visualize the movement of blood through the heart, arteries and veins. M-mode ultrasound displays and records moving echoes from moving organs such as heart. The motion of tissue can be interpreted in terms of myocardial and valvular function. However, these kinds of ultrasound imaging could not provide a quantitative imaging of strain and elastic modulus distribution in the image field that can be produced by ultrasound elastography.

2.2 Strain estimation in elastography

Many strain estimation methods for elastography have been developed to assess map of the strain distribution induced by an applied compression. Depending on signal sources for correspondence function of each method, strain estimation methods in elastography can be classified into three main categories: time-based, phase-based and displacement-based estimators. These three major strain estimators are discussed in more detail in the following sections. Fundamental mathematical operations that extract signal correspondence from two signals, and displacement estimation techniques that find time delay or displacement value from a pair of ultrasound echo signals are also further described in Appendix A and B, respectively.

2.2.1 Time-based strain estimation

Time-based strain estimation methods (TSE) [2, 24], also called as time delay strain estimator (TDE) is the process of determining the time shift between a reference signal and delayed signal. In medical ultrasound, time delay estimation (TDE) is used in blood flow estimation, tissue elasticity estimation, radiation force imaging, and a number of other

algorithms. The process of time-delay estimation generally is concerned with the determination of the one-dimensional (1-D) shift between two 1-D signals, using pattern matching algorithms such as normalized cross-correlation (NCC) [2, 24]. Sum-of-absolute differences (SAD) [25], sum of squared differences (SSD) [26] and other various methods are also used as a pattern matching algorithm to find the signal correspondence. Mathematical definitions of NCC, SAD, and SSD are described in Appendix B.1. In elastography, the TDE estimates the time delays between two data sets acquired at different time points, i.e. pre- and post-compression radio frequency (RF) echo signals. Then, strains are calculated from the time delays (Figure 2.1), i.e.

$$\varepsilon_1 = \frac{(t_{1b} - t_{1a}) - (t_{2b} - t_{2a})}{t_{1b} - t_{1a}}, \tag{2.1}$$

where t_{1a} and t_{1b} are the arrival times of the pre-compression echoes from the two reference windows (proximal and distal), respectively, and t_{2a} and t_{2b} are the arrival times of the post-compression echoes from the same windows, respectively.

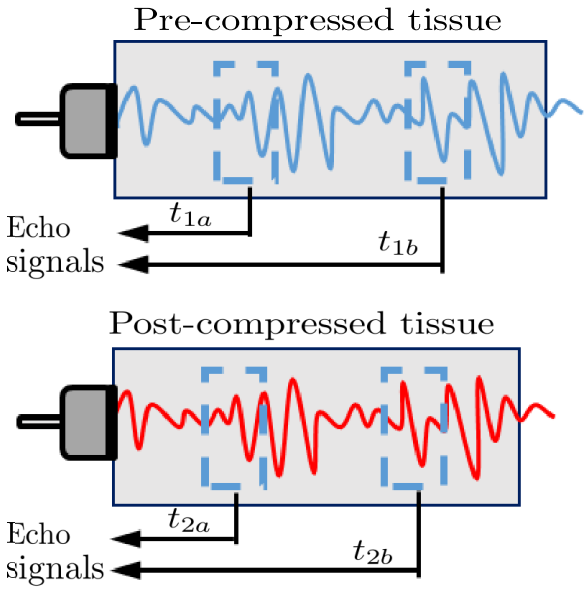

Figure 2.1: Principles of time-based strain estimation (TSE)

Since the RF signals received by transducer are not continuous but an array of pulses,

TSE performance is limited fundamentally by the sampling interval. The time delay estimates will be quantified at this interval, resulting in estimator bias and variance that are significantly higher than theoretically achievable limits. The impact of finite sampling interval can be reduced by using signal interpolation before computing the signal correspondence, or performing interpolation on the results from the signal correspondence function. This approach, called sub-sample method, allows finer estimation of the true delay in sub-sample precision [27] using various interpolation methods. Parabolic, cosine, and spline fitting algorithms that use three nearest points for interpolation are generally used for sub-sample methods [28]. More details regarding sub-sample methods will be described in Section 2.3.1. However, the computational cost of sub-sample method in addition to pattern matching algorithm can be significant.

Strain conversion methods in elastography are typically based on gradient estimation [2, 29] or direct slope estimation such as least-squares methods [30]. In gradient-based methods, strain is calculated as the local gradient of displacement estimates. The distance between the samples used for estimating the gradient significantly affects the SNR of these methods. Due to high sensitivity of noise in gradient operator, low-pass filtering such as median filtering is usually carried out before computing gradients. On the other hand, direct slope estimation methods (least-squares methods) estimate strain directly as the slope of the displacement with respect to depth [3]; therefore, they are less sensitive to noises.

Random noises in echo signals and the external forces nonuniformly transmitted to the inside tissues degrades the performance of the time-based strain estimation. Particularly, echo signal decorrelation is the major cause of the artifacts. The applied external force causes the compressive deformation in the tissues. If the deformation is excessive and the signals from the same region before and after the compression (signals in dotted box in Figure 2.1(a)) do not show enough accordance, signal correspondence function fails to match the pattern in pre- and post-compression data, and the decorrelation error occurs. The relative displacement of scatterers in three dimensions due to the external compression exacerbates decorrelation errors. To compensate for the degradation due to the echo signal decorrelation, stretching/companding the post-compression signal is generally used [31]. These stretching/companding of the post-compression ultrasound echo signals can reduce

the effects of the mechanical compression on the signal, thereby, significantly improve the image quality of strain estimation for small strain (around 1%) [31, 32, 33].

Although the standard TSE methods have been commonly used in ultrasound strain imaging, the massive computational load of the standard TSE is the major obstacle to accomplish the ultrasound elastography in real time. This is caused by the high computational load of the signal correspondence functions for finding time delay and signal interpolation for the sub-sample. For real time elastography implementation based on TSE methods, "Time domain cross correlation with prior estimates" (TDPE) [24] have been developed to achieve the real-time elastography. In order to speed up computation, TDPE uses previously calculated displacements of neighboring windows to guide the search to a very small area. As a result, TDPE is much faster than the standard TSE method and may be used for real time applications.

2.2.2 Displacement-based strain estimation

In displacement-based strain estimation method (DSE), strains are directly estimated in spatial domain using ultrasound B-mode images, by applying digital image correlation (DIC) technique [4, 5]. DIC is a non-contact optical sensing method mainly used for measuring in-plane strain field [34]. DIC has also been applied to deformation in soft biological tissues and biomaterials such as arterial tissues due to noncontact nature of testing protocol [35]. As shown in Figure 2.2(a), DIC measures the displacement in compressed tissues from a predefined search region between pairs of windowed ultrasonic B-mode images. A series of ultrasonic B-mode images are taken by a conventional medical ultrasound scanner while compressing the examined organ with an ultrasound probe or an external loading device. Video signals from the ultrasound scanner can be transformed to B-mode image files that are recorded on the computer. Spatial deformation between the pairs of B-mode images is estimated by the DIC using a block-matching algorithm. One of the most common block-matching algorithms is normalized cross correlation (NCC) algorithm [36], which estimates the degree of similarity between two compared images. Let $f(x, y)$ be the intensity value of the $M \times N$ image f at the pixel (x, y) where $x \in 0, \ldots, M-1, y \in 0, \ldots, N-1$. Similarly, let $g(x, y)$ be the intensity value of $m \times n$ reference template g where $m \leq M$ and $n \leq N$.

The normalized cross correlation coefficient used for finding matches is given as:

$$NCC(u,v) = \frac{\Sigma_{x,y}(f(x,y) - \bar{f}_{u,v})(g(x-u,y-v) - \bar{g})}{\left[\Sigma_{x,y}(f(x,y) - \bar{f}_{u,v})^2 \Sigma_{x,y}(g(x-u,y-v) - \bar{g})^2\right]^{1/2}}, \tag{2.2}$$

where $u \in 0,\ldots,M-m, v \in 0,\ldots,N-n$ is the mean value of the reference template g, and $\bar{f}$ is the mean value of the image f in the region under g. However, $NCC(u,v)$ requires a significant amount of computation time that increases dramatically with the size of sub-image. To reduce the computation time, the fast normalized cross-correlation (FNCC) proposed by Lewis [37] is frequently adopted. The mathematical definition of FNCC is provided in Appendix B.2.

Strains are estimated by taking the gradients of the displacements (Figure 2.2(b)):

$$\varepsilon_1 = \frac{(x_{1b} - x_{1a}) - (x_{2b} - x_{2a})}{x_{1b} - x_{1a}}, \varepsilon_2 = \frac{(y_{1b} - y_{1a}) - (y_{2b} - y_{2a})}{y_{1b} - y_{1a}}, \tag{2.3}$$

where (x_{1a}, y_{1a}) and (x_{1b}, y_{1b}) are the coordinates of the proximal and distal windows in the pre-compression image, respectively, and (x_{2a}, y_{2a}) and (x_{2b}, y_{2b}) are the coordinates of the same windows in the post-compression image, respectively. Once strain field is obtained, elastographic processing similar to TDE is performed to generate the elastograms [4]. The accuracy of DIC is limited to the size of a pixel because its operation is based on digital images composed of pixels. Furthermore, the signal noise is inevitable while acquiring and transmitting the ultrasound signals. Thus, data reconstruction should be conducted to enhance the quality of displacement and strain field. To overcome this, the penalized least-square regression method has been proposed by [4, 5]. The main drawback of DSE lies in the heavy computation load. To reduce the computation time, TDPE [24] or decoupled cross-correlation (DCC) algorithm [38] have been proposed. However, their computation speeds are still not fast enough to achieve real-time elastography.

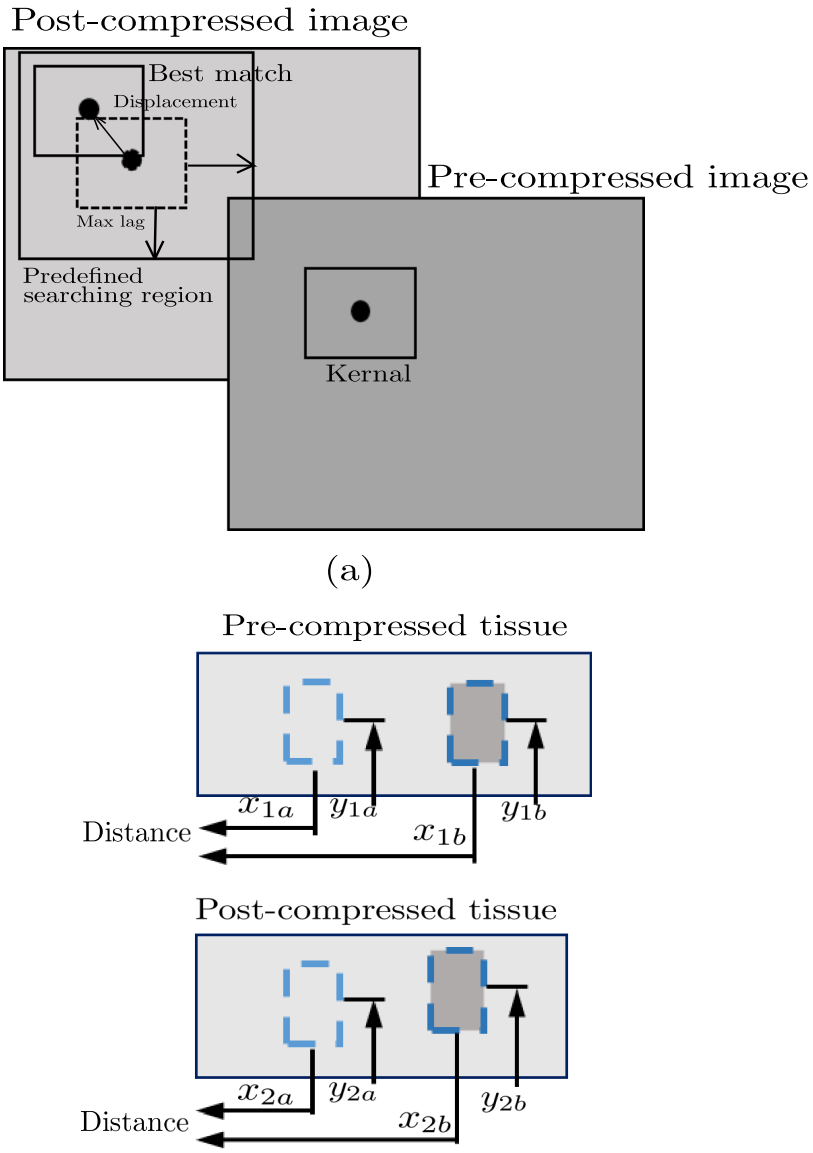

Figure 2.2: Principles of: (a) digital image correlation (DIC) for displacement estimation and (b) displacement-based strain estimation method (DSE).

2.2.3 Phase-based strain estimation

Doppler ultrasound has become indispensable as a noninvasive tool for the diagnosis and management of cardiovascular disease [39]. Typical Doppler ultrasound instruments emit a narrow-band radio frequency (RF) pulse and process the backscattered echoes by means of phase quadrature demodulation, using the pulse's central frequency as the reference sinusoid, followed by integration over the extent of the range gate [40].

In phase-based strain estimation (PSE) methods, the strain can be obtained from the measure of strain rate acquired by Doppler tissue imaging techniques, as temporal integration of the strain rate is equivalent to the spatial derivative of the velocity [41]. Utilizing the velocity measures at each point in the region of interest, the amount of the deformation of tissues and the speed of the deformation caused by an applied external compression can be estimated. Typically, the axial differentiation of velocity field is calculated by autocorrelation algorithm [42] based on the assumption that the speed of sound, sampling interval, and the pulse repetition period are the known constants. Assume that an ultrasonic transducer transmits waves toward an object moving at the instantaneous velocity V as depicted in Figure 2.3. If a segment is defined as the region of axial length L_0, and the change in the length of the segment $\Delta L = T_{PR}(V_2 - V_1)$ (Figure 2.3), the axial strain from PSE is rewritten as:

$$\varepsilon = \frac{T_{PR}}{L_0}(V_2 - V_1), \tag{2.4}$$

where V_i is the instantaneous velocity at both endpoints of the segment, and T_{PR} is the sampling interval along the frame, respectively.

Since temporal integration of the strain rate is equivalent to the spatial derivative of the velocity, strain also can be obtained from the measure of strain rate acquired by Doppler tissue imaging techniques [41]. Depending on the velocity measures at each point in region of interest, amounts of the deformation of tissues and the speed of the deformation due to an applied external compression can be estimated. In the phase-based strain estimation (PSE) [42, 43, 44, 45, 46] methods, the axial differentiation of velocity field is typically calculated by one-dimensional autocorrelation [43] or two-dimensional autocorrelation [42].

Subsequently, gradient operators or least squares estimation methods are also utilized to compute the strain values.

For implementing real-time elastography, the computational efficiency and the image quality of such algorithms are considered as two important factors for choosing the feasible algorithm. Because of the fast computation speed, many research groups have selected PSE methods as a real time elastography algorithm. However, aliasing is the most problematic issue of PSE methods. To avoid aliasing, several techniques have been developed. Phase unwrapping methods [47] have been introduced to extend the aliasing limit from a quarter to one-half of wavelength. Subsequently, "Phase Root Seeking" (PRS) [44] and "Combined Autocorrelation Method" (CAM) [45] have also been proposed for the further improvement of the limit. Using Newton iterations to find the zero-phase position from point to point, PRS compensates the phase shift. CAM combines a phase seeking technique with the envelope correlation coefficient to estimate the compensated phase shift. However, all phase unwrapping methods commonly suffer from line errors called dropout [48] due to dependency of the accuracy on the previous position's phase shift estimation. "Angular correlation method" (ACM) [46] which estimates each phase shift independently of other positions has been developed as an improvement of the dropout error.

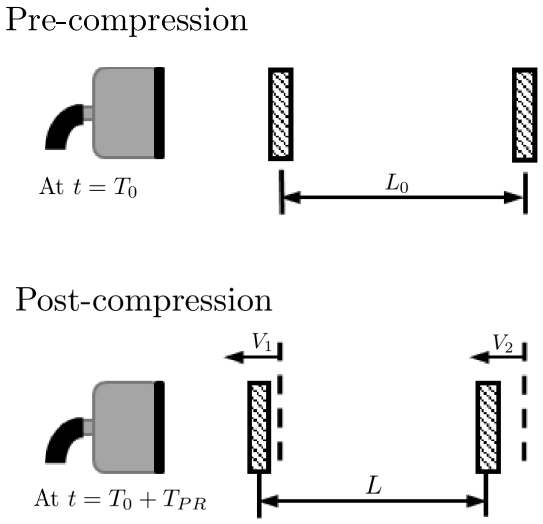

Figure 2.3: Principle of strain estimation in PSE.

2.3 Sub-sample methods

2.3.1 Sub-sample Methods for 1D Time Domain

The sub-sample time delay estimation can be applied to the time delay measures to achieve better accuracy by using interpolation methods. In this section, common 1D sub-sample methods are briefly discussed to find the optimal time delay estimates .

Parabolic Fitting Method

Parabolic fitting method fits a second order polynomial of the form $y_c(x) = ax^2 + bx + c$ around the peak of the "correlation" function, $y_c(0)$, and its two neighbors $y_c(-1)$ and $y_c(1)$. Given the peak and its two neighbors, the estimated sub-sample shift is defined as [28]:

$$\hat{\xi}_{parabolic} = \frac{y_c(-1) - y_c(1)}{2(y_c(-1) - 2y_c(0) + y_c(1))}. \tag{2.5}$$

Despite its simple use and computational efficiency, parabolic fitting provides biased estimates of time delays [28].

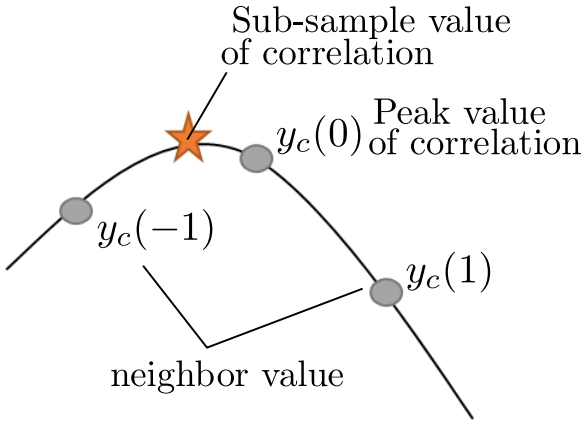

Figure 2.4: Principle of sub-sample methods using 3 points.

Cosine Fitting Method

Cosine curves can be used to estimate the sub-sample time delay. Given the peak of the "correlation" function, $y_c(0)$, and its two neighbors $y_c(-1)$ and $y_c(1)$, the estimated sub-sample time delay is given by [28]:

$$\hat{\xi}_{cosine} = -\frac{\beta_c}{\alpha_c}, \tag{2.6}$$

where α_c and β_c are coefficients defined as:

$$\begin{aligned} \alpha_c &= \arccos \frac{y_c(-1) + y_c(1)}{2y_c(0)}, \\ \beta_c &= \arctan \frac{y_c(-1) - y_c(1)}{2y_c(0)\sin\alpha}. \end{aligned} \tag{2.7}$$

This method produces relatively low bias and variance compared with parabolic fitting method. However, signal aliasing exceeding the Nyquist limit and high computational cost are the drawbacks of this method.

Spline Fitting Method

Spline fitting method fits between the data points from the pattern-matching function curve using a smooth cubic function given by [28]:

$$y_c(x) = ax^3 + bx^2 + cx + d, \tag{2.8}$$

where a, b, c and d are coefficients determined by the best fit to the pattern-matching function. By searching the optimal value of x, the sub-sample time delay estimate will be calculated. Although its computational cost is higher than parabolic interpolation, the spline fitting method generates more accurate estimates.

2.3.2 Sub-sample Method for 2D Space

The accuracy of displacement estimates from digital image correlation (DIC) using the 2D image block matching algorithm is limited to the size of a pixel due to the intrinsic

nature of discontinuities of digital envelope data. To overcome this problem, the sub-sample algorithm based on the quadratic interpolation can be implemented [49]. By fitting a second order polynomial to the optimal value of data correspondence and its neighbor data and searching the local extremum of the polynomial, the two dimensional sub-sample precision can be accomplished. Depending on the position of the local extremum, the displacement estimation from the correlation function is optimized.

Assume Y is the second order polynomial fitted to the maximum value from the correlation function and its 8 surrounding data. The second order polynomial is defined as:

$$\begin{bmatrix} u_{-1,-1} & u_{0,-1} & u_{1,-1} \\ u_{-1,0} & u_{0,0} & u_{1,0} \\ u_{-1,1} & u_{0,1} & u_{1,1} \end{bmatrix} = \begin{bmatrix} Y(-1,-1) & Y(0,-1) & Y(1,-1) \\ Y(-1,0) & Y(0,0) & Y(1,0) \\ Y(-1,1) & Y(0,1) & Y(1,1) \end{bmatrix}, \tag{2.9}$$

where $Y(x,y) = A + Bx + Cy + Dxy + Ex^2 + Fy^2$.

For matrix form, Eq. (2.9) can be rewritten as:

$$u = \phi X$$

$$\begin{bmatrix} u_{-1,-1} \\ u_{0,-1} \\ u_{1,-1} \\ u_{-1,0} \\ u_{0,0} \\ u_{1,0} \\ u_{-1,1} \\ u_{0,1} \\ u_{1,1} \end{bmatrix} = \begin{bmatrix} 1 & -1 & -1 & 1 & 1 & 1 \\ 1 & -1 & 0 & 0 & 1 & 0 \\ 1 & -1 & 1 & -1 & 1 & 1 \\ 1 & 0 & -1 & 0 & 0 & 1 \\ 1 & 0 & 0 & 0 & 0 & 0 \\ 1 & 0 & 1 & 0 & 0 & 1 \\ 1 & 1 & -1 & -1 & 1 & 1 \\ 1 & 1 & 0 & 0 & 1 & 0 \\ 1 & 1 & 1 & 1 & 1 & 1 \end{bmatrix} \begin{bmatrix} A \\ B \\ C \\ D \\ E \\ F \end{bmatrix}. \tag{2.10}$$

The least square solution X can be solved by using pseudo-inverse matrix calculation.

$$X = (\phi^T \phi)^{-1} \phi^T u \tag{2.11}$$

Differentiating the approximate Y with respect to x and y, the coordinates of the

extremum are obtained through the partial derivatives:

$$\begin{aligned} \frac{\partial Y}{\partial x} &= B + Dy_{ex} + 2Ex_{ex} = 0, \\ \frac{\partial Y}{\partial y} &= C + Dx_{ex} + 2Fy_{ex} = 0, \end{aligned} \tag{2.12}$$

where x_{ex} and y_{ex} are the coordinates of the extremum.

2.4 Image Quality Measures

Varghese and Ophir [50, 51] was proposed the strain filter (SF) which characterizes the elastographic system. The SF provides the range of strain by specifying the elastographic image measures such as the elastographic signal-to-noise (SNRe), sensitivity, and the strain dynamic range at a given resolution. The range of strain can be used as a performance measure predicting the elastogram quality. The filtering process is performed in strain domain, and then the qualified elastogram of a limited range is obtained. The range of strain allowed by a SF process is often limited by the limitations of ultrasound acoustic parameters, and the signal processing parameters [9].

Elastography can be typically evaluated using the elastographic signal-to-noise ratio (SNRe) and contrast-to-noise ratio (CNRe) that are employed as metrics for the quality of the elastograms. The elastographic SNRe identifies the quantitative measurement of the accuracy and precision of the elastograms, and is defined as [52]

$$\text{SNRe} = \frac{m_s}{\sigma_s}, \tag{2.13}$$

where m_s is the mean value of the strain, and σ_s is the standard deviation of the measured strain. The trade-off between SNRe and resolution of all strains are illustrated in Figure 2.5(a).

By combining SF and the elastic contrast properties (CTE) of tissue, the CNRe can be predicted (Figure 2.5(b)). The CNRe is an important parameter to determine the detectability of a stiff lesion in elastograms and is defined as [52]

$$\text{CNRe} = \frac{2(m_o - m_i)^2}{\sigma_o^2 + \sigma_i^2}, \tag{2.14}$$

where m_i, m_o, σ_i^2, and σ_o^2 are the mean and the variance values for the inside (subscript i) and the outside (subscript o) of the lesion, respectively. The maximum CNRe implies that the differences in mean strain values are large or the sums of variances of the strain are small. Therefore, if modulus contrast is small, CNRe would be improved when strain variances is small. In contrast, at high modulus, CNRe is improved when the difference of strain means is large.

2.5 Elastographic Processing

Strain imaging is highly sensitive to even small deviations of the displacements and signal noises in ultrasound data acquisition and transmission, and thus often fails to detect a malignant region in tissue or depicts the low contrast images. Decorrelation error or called false peak error showing large negative or positive values [24, 43] and the speckle noise generated by small particles in the tissue or liquid which reflect ultrasonic wave [53] are the major causes of the strain degradation in ultrasound elastography. In order to avoid the false peaks and reduce the signal noise like speckle noise in ultrasound images, elastographic processing or called post-processing methods are necessary so that ultrasound elastography produces the high contrast strain images which facilitate the detection of malignant region.

A typical elastographic post-processing is comprised of statistical thresholding and data smoothing processes [42]. In the statistical threshold process, the mean (μ_s) and the standard deviation (σ_s) of a strain image are calculated and the strain magnitudes are threshed to the range $\mu_s \pm 3\sigma_s$. First, false peak errors from the decorrelation can be threshed through the statistical threshold process. Afterward, the data smoothing processes [4, 42] using de-noising filters; i.e., median filter, Gaussian filter, Wiener filter, and penalized least square regression are used to reduce the signal noises or to recover the de-noising images. Median filter replacing a pixel value with the median of the pixel in an m_{med} by n_{med} neighborhood of the pixel is widely used as a simple post-processing technique [42].

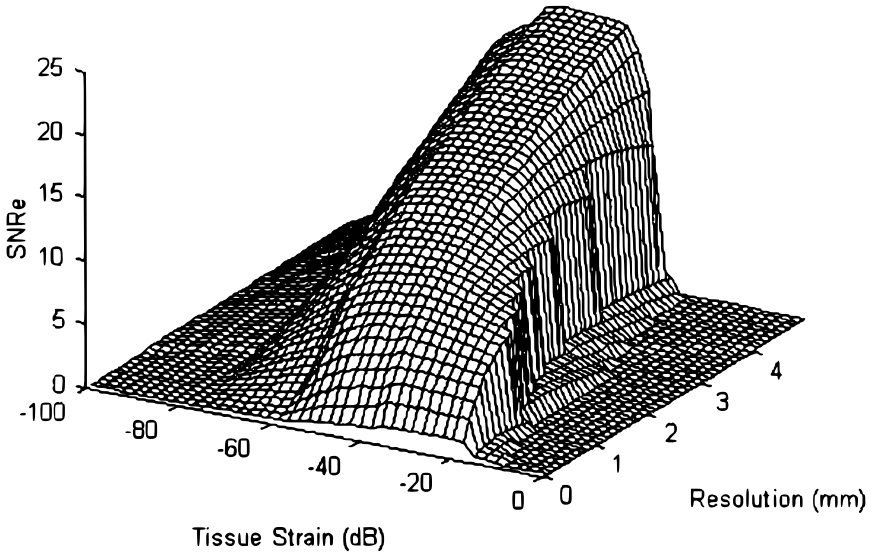

(a)

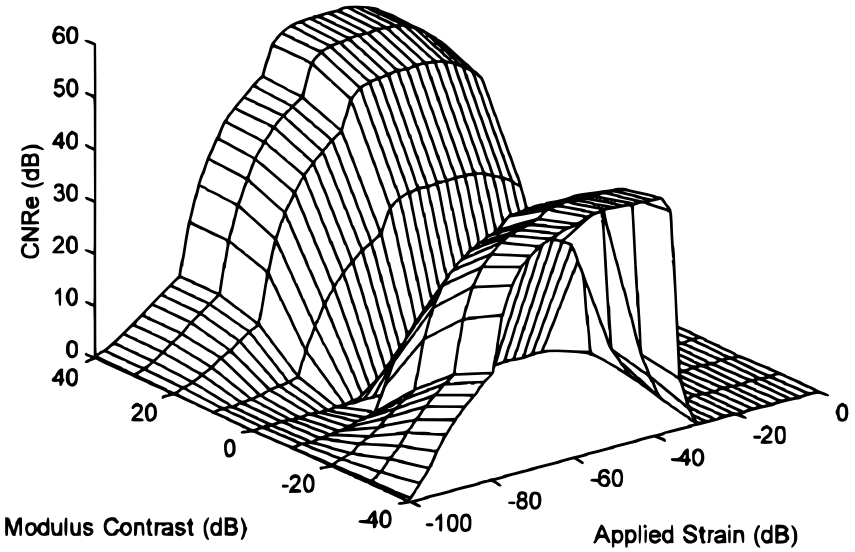

(b)

Figure 2.5: Three-dimensional typical appearance of SF: (a) trade-off between strain dynamic range, sensitivity, and SNRe, (b) plot of CNRe curves (Ophir et al. 1999).

Chapter 3

Robust Phase-based Strain Estimation

3.1 Introduction

Portable wireless ultrasound is recently emerging as a new ultrasound device due to its unique advantages including small size, lightweight, wireless connectivity and affordability. Modern portable ultrasound devices with sophisticated processors and image processing algorithms offer high image quality and some of them provide multiple ultrasound modes including color Doppler, echocardiography, and endovaginal examination. However, none of the portable ultrasound devices provides elastography function due to the limitations in computational performance and data transfer speed of wireless communication. Motivated by potential demands of elastography in portable ultrasound, this research aims to develop a suitable elastography method for portable ultrasound, called the robust phase-based strain estimator (RPSE), that can achieve fast strain estimation, while not losing elastogram quality. Performance and suitability of RPSE for portable ultrasound were compared with time-delay strain estimator (TSE), phase-based strain estimator (PSE) and displacement-gradient strain estimator (DSE) that are widely used in current ultrasound elastography. Three types of raw RF data sets were used for the test: The first two sets were generated from numerical phantoms composed by an open ultrasonic simulation code

(Field II) and a commercial FEA (Abaqus). The last data set was acquired experimentally with a commercial portable ultrasound device using a gelatin-based phantom containing a stiff cylindrical inclusion in soft matrix. To assess image quality of elastograms, signal-to-noise (SNRe) and contrast-to-noise (CNRe) ratios were measured on the elastograms produced by the three strain estimators. The computational efficiency of each method was also estimated and compared together.

3.2 Theory

3.2.1 Velocity Estimation

The fundamental Doppler equation expresses the frequency shift Δf of acoustic energy scattered from a target moving at some velocity V in terms of the frequency of the incident wave f_c, the speed of sound c in the propagation medium, and the angle θ between the direction of motion and the direction of sound propagation as [54]

$$\Delta f = 2\frac{f_c}{c} V \cos\theta. \tag{3.1}$$

This implies that the frequency shift carries information about the axial velocity $V_a (= V\cos\theta)$ of the moving reflector. If the axial velocity is sufficiently slower than speed of the sound c in the propagation, the axial velocity can be obtained as

$$V_a = \frac{c}{2}\frac{\Delta f}{f_c}. \tag{3.2}$$

In the practice for elastography, the wave direction is usually identical to the moving direction, so θ can be regarded as zero. Therefore, the axial velocity V_a can be estimated by determining only the frequency shift Δf, while assuming that c and f_c are known and constant. Since this conventional Doppler method uses information from a relatively narrow band of frequencies to measure the phase changes in the carrier frequency, it is also called narrowband Doppler. However, due to stochastic nature of the RF signal, derived V_a usually exhibits large fluctuations [55].

To reduce the variance of the velocity estimates, Wilson [56] proposed broadband pulsed Doppler based on 2D fast Fourier transform by considering RF data as a 2D function of depth and time. He showed that the 2D FFT of RF data from a moving target forms a line whose slope is proportional to the target velocity. Loupas et al. [57, 58] extended Wilson's work to discrete limited-duration signals by examining the case of an ideal point target. They showed that 2D spectrum of a discrete version of backscattered RF signal is zero apart from a line passing though the origin of the 2D frequency plane with a slope equal to [57]

$$\frac{F}{f} = \frac{2V}{c}\frac{T_{PR}}{T_s}, \tag{3.3}$$

where T_s and T_{PR} are sampling interval and pulse repetition period (fast- and slow-time sampling rates), respectively, and f and F are normalized RF and Doppler frequencies, respectively. Expressed in absolute RF and Doppler frequencies ($f_{RF} = f/T_s$ and $F_D = F/T_{PR}$), Eq. (3.3) becomes [57]

$$\frac{F_D}{f_{RF}} = \frac{2V}{c}, \tag{3.4}$$

which is the same as conventional narrowband Doppler equation. Eq. (3.4) also implies that while the mean RF frequency $\overline{f}_{RF}$ may fluctuate randomly, the corresponding mean Doppler frequency $\overline{F}_D$ tracks these fluctuations so that their ratio is always constant and proportional to the mean axial velocity.

The frequency ratio in Eq. (3.3) can be estimated directly in the time domain by evaluating the phase of autocorrelation function $\gamma[m,k]$ at lags in fast-time ($m = 1, k = 0$) and slow-time ($m = 0, k = 1$) axes as [58]

$$\overline{f} = \frac{1}{2\pi}\arctan\frac{Im[\gamma(1,0)]}{Re[\gamma(1,0)]} = \frac{1}{2\pi}\arg\gamma[1,0], \tag{3.5}$$

$$\overline{F} = \frac{1}{2\pi}\arctan\frac{Im[\gamma(0,1)]}{Re[\gamma(0,1)]} = \frac{1}{2\pi}\arg\gamma[0,1], \tag{3.6}$$

where the phase of autocorelation function $\gamma[m,k]$ is further described in Appendix A.2. By combining Eq. (3.3), (3.5) and (3.6), the mean velocity $\overline{V}$ evaluated by 2D autocorrelator

can be expressed as [42]

$$\overline{V} = \frac{c}{2}\frac{T_s}{T_{PR}}\frac{\arg\gamma[0,1]}{\arg\gamma[1,0]} = \frac{c}{2}\frac{T_s}{T_{PR}}\Gamma, \tag{3.7}$$

where $\Gamma = \arg\gamma[1,0]/\arg\gamma[0,1]$.

3.2.2 Strain Estimation

The axial strain of a segment that has been deformed along loading direction is defined as

$$\varepsilon = \frac{\Delta L}{L} = \frac{L - L_0}{L_0}, \tag{3.8}$$

where ΔL is the difference between the final length L and initial length L_0 of the segment.

In elastography, it can be assumed that an ultrasonic transducer transmits waves toward an object moving with an instantaneous velocity V as depicted in Figure 3.1. If a segment is defined as the region of axial length L_0, and the upper and the lower endpoints of the segment are away from the transducer by the distance λ_1 and λ_2, respectively (Figure 3.1), the echo delays from the upper and the lower endpoints at time $T_0 + T_{PR}$ are

$$\tau_1 = \frac{2(\lambda_1' - \lambda_1)}{c} \text{ and } \tau_2 = \frac{2(\lambda_2' - \lambda_2)}{c}, \tag{3.9}$$

respectively. Since $L_0 = \lambda_2 - \lambda_1$ and $L = \lambda_2' - \lambda_1'$, the axial strain can be written with echo delays by combining Eq. (3.8) and (3.9) as

$$\varepsilon = \frac{c}{2L_0}(\tau_2 - \tau_1) = \frac{c}{2L_0}\Delta\tau. \tag{3.10}$$

The change in the length of the segment $\Delta L = T_{PR}(V_2 - V_1)$ (Figure 3.1), so the echo delay $\Delta\tau$ is related to the velocity as

$$\Delta\tau = \frac{2T_{PR}}{c}(V_2 - V_1). \tag{3.11}$$

By substituting Eq. (3.11) into (3.10), the speed of sound c is canceled and the axial strain can be rewritten as

$$\varepsilon = \frac{T_{PR}}{L_0}(V_2 - V_1), \tag{3.12}$$

Now let's consider an axial segment along single scan line. If the segment is centered at m depth samples with the upper and lower endpoints given by $m_1 = m - \Delta m/2$ and $m_2 = m + \Delta m/2$, the axial length of the segment is

$$L_0 = \Delta m \frac{c}{2} T_s, \tag{3.13}$$

where the tunable parameter m controls the length of the axial length of the segment. By substituting Eq. (3.13) into (3.12) and rewriting V_1 and V_2 using Eq. (3.7), the local axial strain can be simplified as

$$\varepsilon = \frac{T_{PR}}{\Delta m \frac{c}{2} T_s} \frac{c}{2} \frac{T_s}{T_{PR}} (\Gamma_2 - \Gamma_1) \tag{3.14}$$

that can be further simplified as

$$\varepsilon = \frac{\Gamma_2 - \Gamma_1}{\Delta m}, \tag{3.15}$$

where Γ_1 and Γ_2 are the 2D autocorrelation values at both endpoints of the segment.

Note that Eq. (3.15) contains only segment length Δm and the phase angle Γ at the upper and lower end points of the segment, thus it is not affected by sampling intervals along depth (T_s) and frame (T_{PR}). In portable ultrasound, sampling interval between frames (pulse repetition period) is equivalent to data-dumping interval via Wi-Fi network; therefore, it cannot be constant or stable as in console-style scanner. Eq. (3.15) indicates that although data dumping interval fluctuates, strain estimation accuracy is not degraded in the proposed RPSE method.

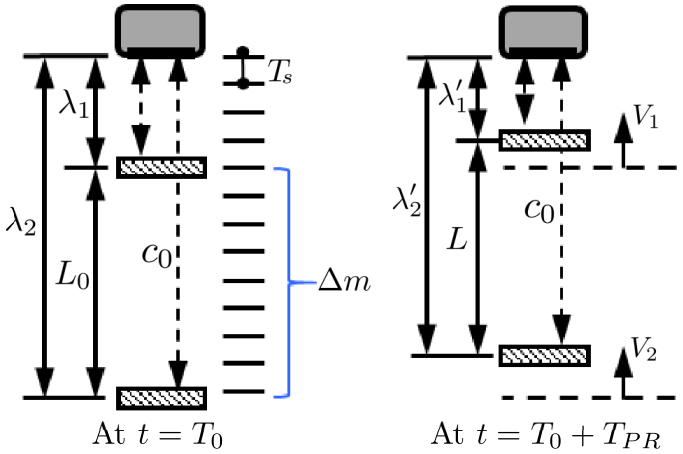

Figure 3.1: Principle of RPSE: ultrasonic transducer transmits waves toward a segment (left). The lower (farthest away from the transducer) and upper endpoints of the segment are moving with an instantaneous velocity V_2 and V_1, respectively (right). As a result, the segment length L0 at $t = T_0$ is changed to L at $t = T_0 + T_{PR}$.

3.2.3 Least-Squares Strain Estimation

The local axial strain estimator in Eq. (3.15) only uses the autocorrelation samples at the endpoints m_1 and m_2, which can cause strain estimate very sensitive to signal noise. Assuming that the 2D autocorrelator Γ in Eq. (3.7) is linear along the depth within the segment, where the segment is centered at depth m, then the autocorrelation relationship can be rewritten as

$$\Gamma[m] = a \cdot m + b, \tag{3.16}$$

where the index m is a natural number restricted by $m_1 \leqslant m \leqslant m_2$. The relationship can be rewritten by the matrix form as $\Gamma = A \begin{bmatrix} a \\ b \end{bmatrix}$. In case only the inaccurate (noisy) measured vector $\widehat{\Gamma}$ is known and the true vector Γ is unknown, the sum of the squared error between the linear model and the measured autocorrelation is minimized by the least-squares method, and the minimized $\widehat{a}$ can be regarded as the axial strain.

3.3 Methods

3.3.1 Numerical Phantom Data Sets

A numerical phantom of the size $40 \times 50 \times 10$ mm^3 with a stiff cylindrical inclusion (10 mm) in a soft matrix was modeled using commercial finite element analysis (FEA) code (Abaqus/CAE 6.10) (Figure 3.2, left). The FEA model was meshed with approximately 427,000 3D quadratic tetrahedron elements and 77,000 nodes. The nodes in the FEA model served as scatterers for reflecting ultrasound signal emitted from the numerical ultrasound transducer; therefore, dense mesh was applied to acquire the acceptable level of RF signals. The elastic modulus of the matrix and the inclusion was set to 20 kPa and 100 kPa, respectively, mimicking a carcinoma in a breast tissue. Poisson's ratio of 0.49 was applied to the whole phantom. The movement in the vertical direction at the bottom of the phantom was constrained while 0.1% axial compressive strain was applied to the top surface. 0.1% compression (0.05 mm, 0.11λ (wavelength)) was selected because

it was within the correlation range of all strain estimators. The coordinate of each node was saved to generate the deformation field data sets.

Field II code [59, 60], a MATLAB-based ultrasound simulation code, was used to add random scatters to the nodal displacements and generate the corresponding pre- and post-compression RF signal data from the numerical phantom (Figure 3.2, center). The amplitudes of the random scatters were kept constant throughout the phantom; thus the inclusion could not be detected in the RF signal or B-mode image. In order to simulate both the conventional and the portable ultrasound device, two kinds of linear probe were virtually modeled by Field II. The first one was modeled to have 192 ultrasound elements and 64 active elements to mimic conventional ultrasound device, while the other had 152 and 24 elements simulating portable ultrasound device. The numerical data sets acquired by these virtual probes are called NP-64 and NP-24, respectively, in the rest of the paper. Other acoustic parameters were set to the same values in both phantoms: the center frequency of the transducer was placed at 3.5 MHz and the sampling rate of RF signals was set to 28 MHz. The speed of sound through the phantom was set to 1540 m/s. In this setting, Field II generated 128 simulated RF lines (A-lines) and each RF line contained 2,589 samples for the phantom depth. Acoustic parameters used in the numerical phantoms are listed in Table 3.1.

Various strain estimation methods (RPSE, TSE, DSE and PSE) were applied to the simulated RF data sets to estimate the strain fields (Figure 3.2, right). The differences between the strain estimates and the true strains computed by the FEA were regarded as estimation errors.

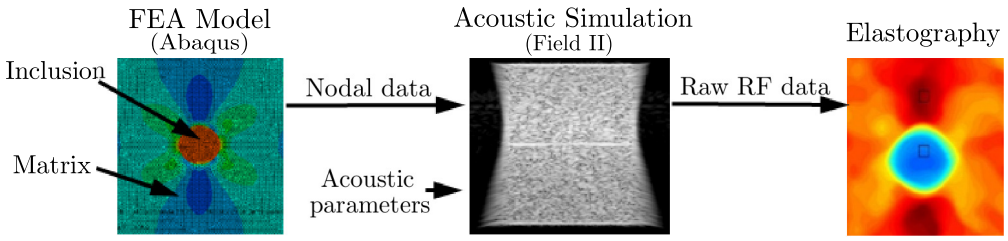

Figure 3.2: Numerical phantom modeled by FEA and Field II code.

Table 3.1: Acoustic parameters for numerical phantoms

	NP-64	NP-24
Phantom size	$40 \times 50 \times 10$ mm^3	$40 \times 50 \times 10$ mm^3
Center frequency	3.5 MHz	3.5 MHz
Sampling frequency	28 MHz	28 MHz
Width	0.44 mm	0.44 mm
Height	5 mm	5 mm
Kerf	0.022 mm	0.022 mm
Number of elements	192	152
Transmit elements	64	24
Receive signals considered	128	128
Transmit/receive focus	50 mm	50 mm

3.3.2 Gelatin-based Phantom Data Set

A gelatin-based phantom containing a stiffer cylindrical inclusion was fabricated to mimic a carcinoma in a normal tissue [4]. Following the protocol in Madsen et al. [61], the inclusion and the matrix were made with the same constituents to have the similar echogenicity, i.e., 1 wt% agarose (J.T. Baker, NJ, USA), 2 wt% glutaraldehyde (Sigma-Aldrich, MO, USA), 5 wt% n-propanol (Fisher-Scientific, NJ, USA), gelatin (Fluka, Germany) (20 wt% and 5 wt% for inclusion and matrix, respectively), and distilled water (the remaining wt%). Glutaraldehyde acted as a cross-linker resulting in a melting point of the materials in the phantom in excess of 68 °C and n-propanol promoted dissolving of materials. In addition, n-propanol and glutaraldehyde served as preservatives. The surrounding matrix was made first to fabricate the phantom. After water was heated up to 85 °C, agarose, gelatin, and n-propanol were added in order. After 3 minutes of solution time, glutaraldehyde was kept at an elevated temperate for 4 more minutes. The resulting solution was poured into a brick-shaped mold sized 90 mm (W) × 80 mm (D) × 140 mm (H) and kept at room temperature for 48 h for gelatin. For the cylindrical inclusion, a pipe (outer diameter of 12.67 mm) was inserted in the mold before pouring the solution (Figure 3.3(a)). Then, one side plate of the mold and the cylindrical pipe were taken out for preparing the inclusion insert (Figure 3.3(b)). In the same manner, the solution with 20 wt% gelatin content was prepared and poured into the cylindrical hole in the matrix gel when temperature decreased to 40 °C (Figure 3.3(c)). Then, the phantom was wrapped by the plastic film to prevent shrinkage and dehydration, and kept at room temperature for another 48 hours. To keep the mechanical property of the phantom, the resulting phantom was recommended to store in water and kept low temperature in a refrigerator. The fabricated phantom contained a cylindrical inclusion (12 mm diameter) five times stiffer than surrounding matrix (47 ± 2 kPa vs. 9 ± 1 kPa).

A commercial portable ultrasound scanner, Sonon 300C (Healcerion Ltd., Korea) with wireless connectivity via Wi-Fi IEEE 802.11 b/g/n, was used for the experiment on the gelatin phantom. SononPlayer, the debugging software for developers, provided the functions to record and export RF data of each ultrasound frame to a personal laptop computer for post-processing. Each recording consisted of 128 channels RF data (A-lines), acquired

using a 3.5 MHz convex probe with sampling frequency of 28 MHz.

Ultrasound RF data were acquired while the phantom was being compressed with a portable ultrasound probe fixed to a TA micro test machine (TA.xt Plus, Stable Micro Systems Ltd, UK) with a 5 kgf load cell (Figure 3.4). The portable ultrasound probe was connected to the personal computer via wireless connection. For the data acquisition, the portable ultrasound probe was moved downward to pre-compression position at which the curved probe perfectly touched the surface of the phantom. Then the probe was moved downward stepwise with the displacement at each step that is corresponding to 0.1% strain increase in the phantom. An ultrasound frame was acquired in the computer via wireless communication at each step. 0.1% strain (equivalent to 0.130 mm displacement) was chosen as a step size, because the corresponding phase change (0.29λ (wavelength)) was within the detectable limit of RPSE (0.5λ). This was repeated until 1% compressive strain was reached in the phantom (total 11 frames).

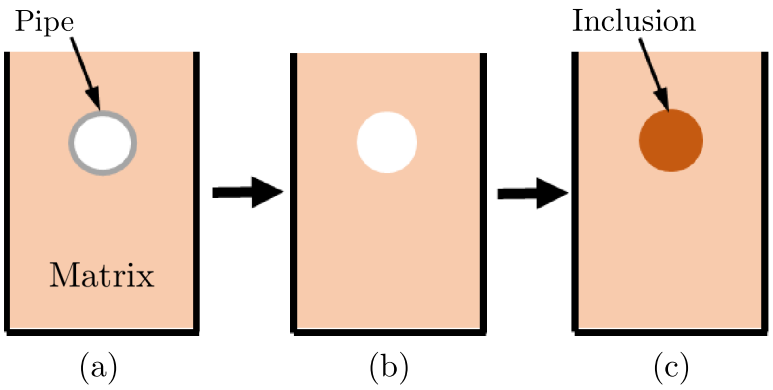

Figure 3.3: Schematic of phantom fabrication procedure: (a) 5% gelatin solution is poured into the mold with the pipe insert to form the matrix; (b) After gelatin is set, one side plate of mold and the insert are taken out; and (c) 20% gelatin solution containing is poured into the empty hole to form the inclusion.

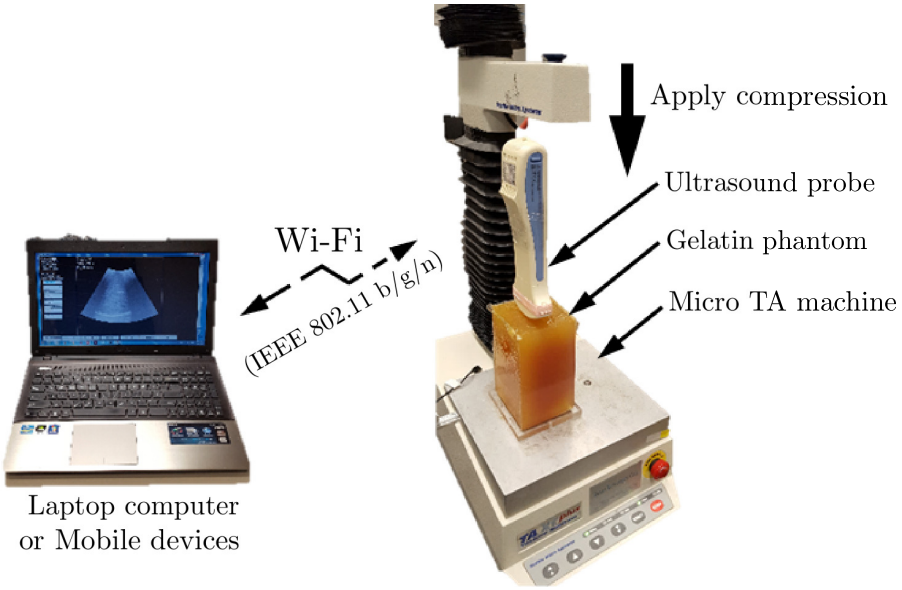

Figure 3.4: Experiment setup for the elastographic phantom test using portable ultrasound.

3.3.3 Implementation of Strain Estimators

TSE, PSE, RPSE and DSE were implemented using MATLAB (The MathWork Inc., MA, USA) as conceptually illustrated in Figure 3.5. The algorithms for each strain estimator are briefly described in this section.

TSE [2] was based on the time delay of raw RF signals (Figure 3.5(a)), which was found by the correlation function as the peak of correlation between the pre- and post-compression signals. Since FFT-based correlation is significantly faster and is also equivalent to linear convolution, it was selected as the TSE algorithm. Window size for correlation was chosen to be 45 samples (1.237 mm) for all data sets. In addition, sub-sample algorithm was implemented to enhance the estimation accuracy by adopting cosine fitting method using 3 points adjacent maximum correlation point. Least-squares strain estimation was also employed to compute the strain distribution that is the slope of fitted displacement curve.

For implementing PSE and RPSE, phase delay between a pair of ultrasound analytic signals formed with the RF data and its Hilbert transform was first estimated (Figure 3.5(b) and (c)). Since each data frame of both numerical and gelatin phantom data sets was acquired from time-independent systems (data was dumped at each displacement), pulse repetition period (T_{PR}) cannot be assigned as a constant value; thus the conventional PSE method can not be implemented. For the comparison with other strain estimators, pulse repetition periods of gelatin and numerical phantom were set to 11, 4 seconds, respectively, which produced the similar scale of strain values to other methods. In RPSE (Figure 3.5(c)), strains were directly estimated using 2D autocorrelation (Eq. (3.15)). Phase unwrapping function in MATLAB was performed to expand the phase limit of PSE and RPSE up to a half wavelength (0.5λ) by preventing aliasing. Least-square method was also utilized to compute the curve-fitted slope of phase delay and the corresponding strain distribution.

Since DSE directly estimates displacement distribution from the spatial domain, the raw RF data should be converted to B-mode image using Hilbert transform and log-compression (Figure 3.5(d)). In addition, bi-interpolation was conducted to increase data resolution of B-mode image because sampling interval in the axial direction is significantly higher than that in the lateral direction (typically more than 10 times) [25]. A block matching algorithm

based on 2D fast normalized cross-correlation (FNCC) calculated the displacements of the selected grids in a pair of pre- and post-compression B-mode images. 2D sub-sample method using a second order polynomial equation was used to enhance the accuracy of the displacement estimate. Then the strain distributions can be estimated by finding the 2D gradient function from the displacement field. The detailed block matching algorithm used in this study is provided in the reference [4]. The distances between grid points in both lateral and axial directions were set to 15 and 60 pixels, respectively, considering computation efficiency and image resolution. The side lengths of squared blocks centered at grid points for both the pre- and post-compression B-mode images were 45 and 68 pixels, respectively.

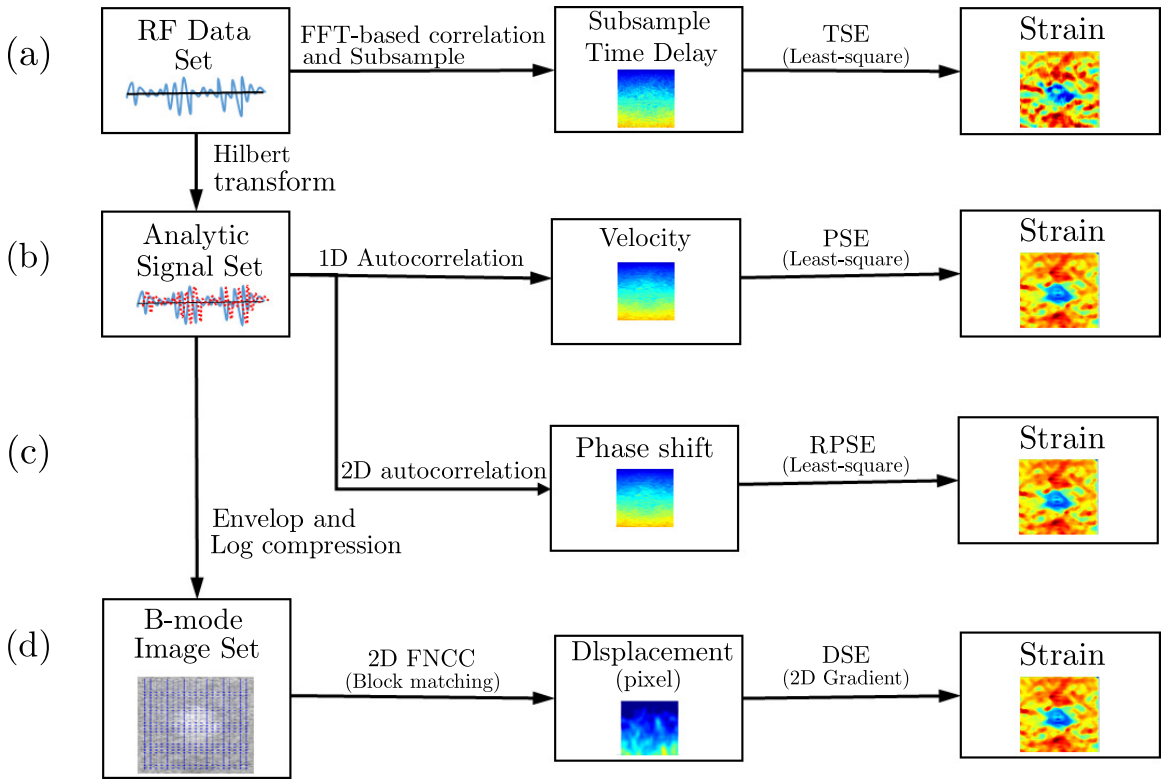

Figure 3.5: Flow chart of strain estimators: (a) time-based strain estimator (TSE), (b) phase-based strain estimator (PSE) (c) robust phase-based strain estimator (RPSE), and (d) displacement-based strain estimator (DSE).

3.4 Results and Discussion

RPSE, TSE, DSE and PSE were applied to the numerical data sets acquired from the numerical phantoms with virtual probes and the experimental data sets from the gelatin phantom with the portable ultrasound device. Displacement field and elastogram produced by each estimator were investigated to evaluate their estimation accuracy. Computational efficiency was also assessed by measuring the computation time spent by each algorithm to generate elastograms.

3.4.1 Displacement Estimation

The displacement fields for two types of numerical data sets (NP-64 and NP-24) estimated by RPSE, TSE, DSE and PSE are presented in Figure 3.6. The velocity fields by PSE are scaled to match with displacement fields from the other methods. Although the fields generated by RPSE (Figure 3.6(a) and 3.6(e)), TSE (Figure 3.6(b) and 3.6(f)) and PSE (Figure 3.6(d) and 3.6(h)) look similar, the RPSE shows more delicate and smoother patterns with less decorrelation errors than the others. On the other hand, DSE (Figure 3.6(c) and 3.6(g)) cannot generate the right pattern and the field around the circular inclusion is significantly mingled. No significant differences are found between the displacement fields from NP-64 (virtually acquired by conventional ultrasound) and NP-24 (portable ultrasound), but the ones for NP-24 (Figure 3.6(e)-(h)) show slightly lower resolutions and more decorrelation errors than those for NP-64 (Figure 3.6(a)-(d)), due to less number of active elements in portable ultrasound. The above results can be quantitatively represented using the displacement plots measured along the vertical centerline across the displacement fields (Figure 3.7). Note that the FEA plot was formed using the true data from FEA, while the other plots were produced from the data in which slight random noises were introduced by Field II. RPSE, TSE and PSE plots show relatively good agreement with the FEA plot, with slight variations caused by the random noises. The DSE plot presents the smoothest trend; however, it is deviated from the FEA plot in some regions. The displacement plots from NP-64 (Figure 3.7(a)) and NP-24 (Figure 3.7(b)) show similar trends over all, although slightly higher variations are observed in NP-24 plot.

The displacement fields in the gelatin phantom were also analyzed (Figure 3.8). Since the experimental data contained higher level of signal noises than the numerical data, the estimated displacement fields are generally nosier and coarser than those for numerical phantom. The displacement field generated by RPSE (Figure 3.8(a)) shows smooth and continuous pattern and the inclusion in the center is discernable with smaller displacement than the surrounding matrix at the same depth. Both TSE and PSE displacement field (Figure 3.8(b) and 3.8(d)) poses similar behavior to RPSE field, but much noisier patterns are observed. A short black line in the middle of the image indicates a spot where decorrelation occurs. The result from DSE (Figure 3.8(c)) shows blurred and mingled pattern, especially in the soft matrix region under the inclusion.

The above behaviors are also demonstrated by the displacement plots in Figure 3.8(e) where RPSE and TSE generate similar plots except a local peak around the middle of the depth in TSE. DSE plot is the smoothest, but slightly deviates from the others in some regions, which is consistent with the trends observed in Figure 3.6. The displacement plot for PSE converted from velocity shows much higher variations than the others, particularly after 35mm depth.

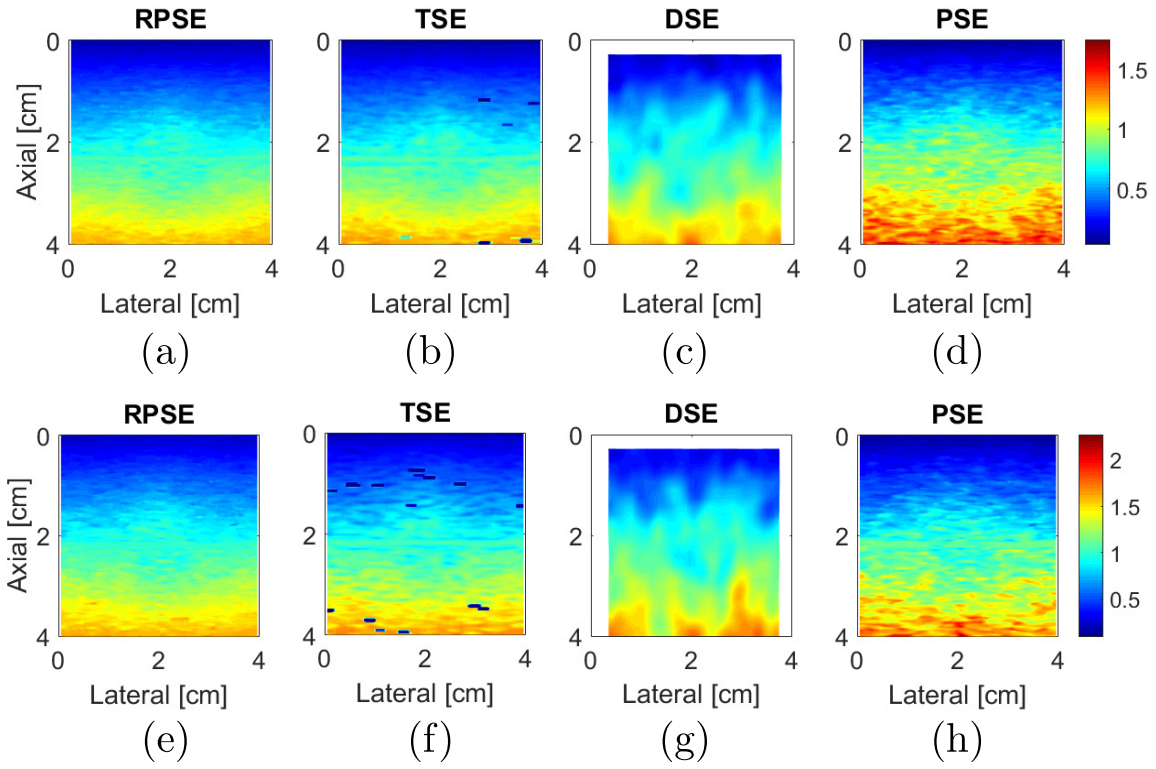

Figure 3.6: Displacement fields of NP-64 numerical phantom estimated by: (a) RPSE, (b) TSE, (c) DSE, and (d) PSE; displacement fields of NP-24 estimated by (e) RPSE, (f) TSE, (g) DSE and (h) PSE, respectively.

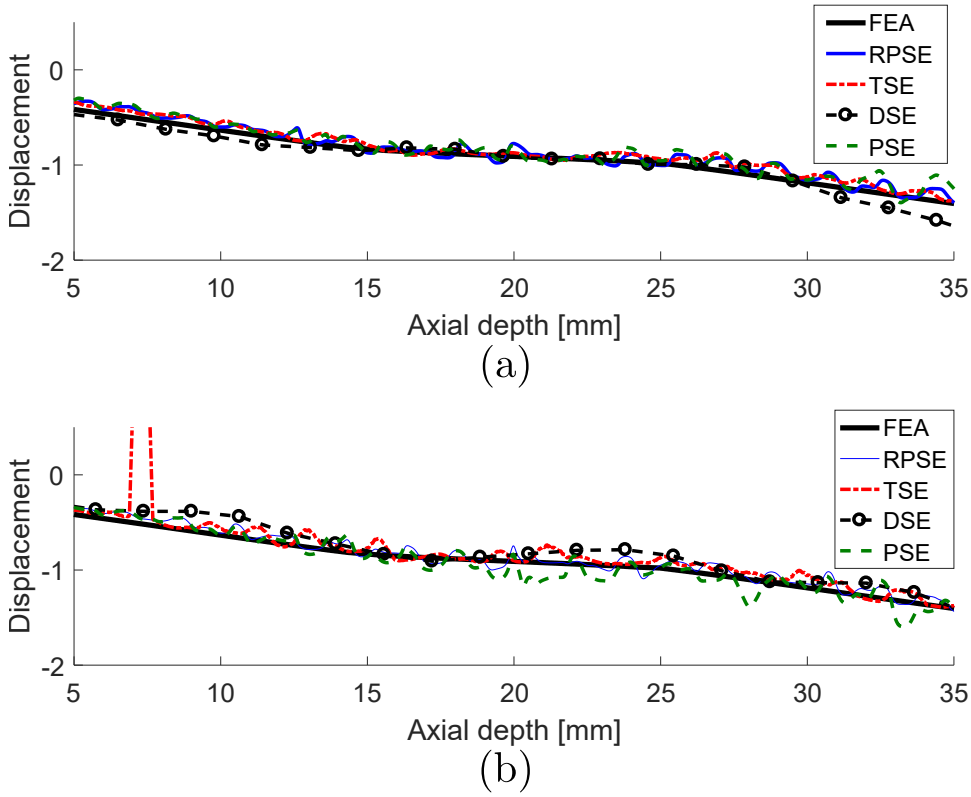

Figure 3.7: Displacement plots along the vertical centerline of (a) NP-64 and (b) NP-24 estimated by FEA, RPSE, TSE, DSE and PSE, respectively.

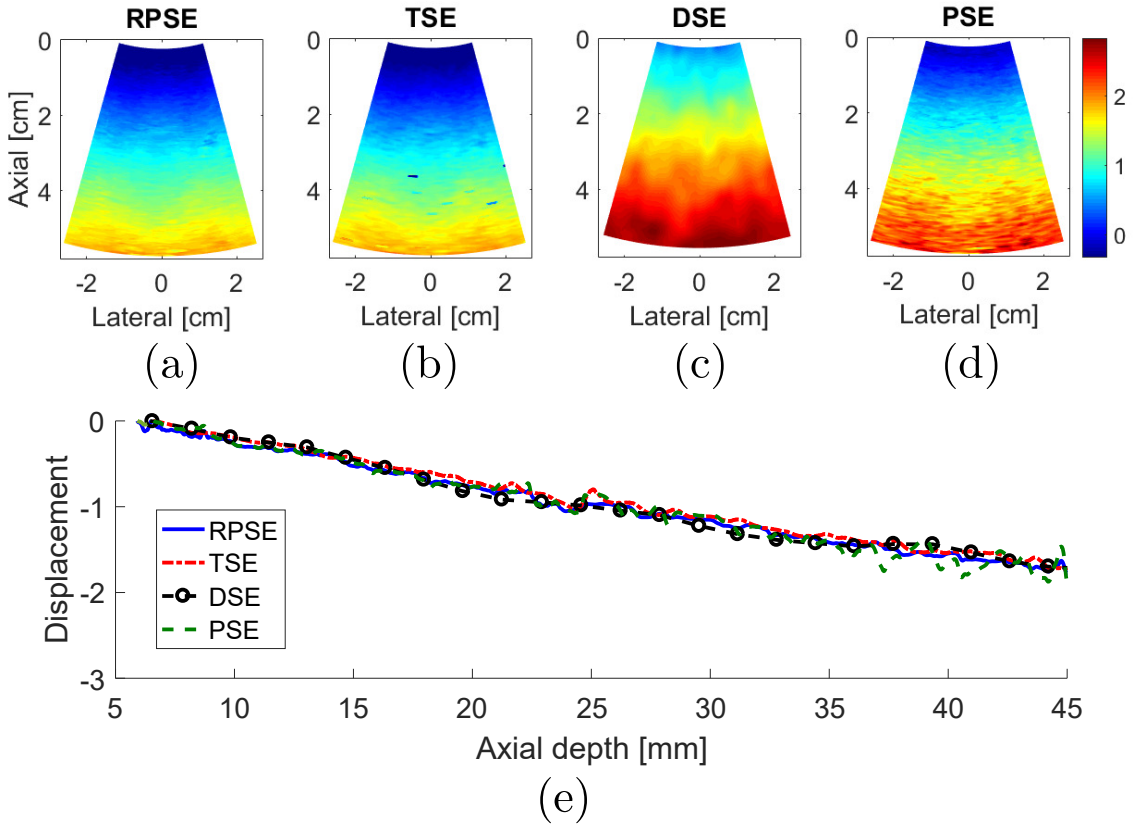

Figure 3.8: Displacement field of the gelatin phantom estimated by: (a) RPSE, (b) TSE, (c) DSE and (d) PSE, and (e) the displacement plots along the vertical centerline from RPSE, TSE, DSE and PSE, respectively

3.4.2 Elastograms

Elastograms depicting the axial strain fields generated by three different strain estimators were presented in Figure 3.9. The elastograms from RPSE (Figure 3.9(a) and 3.9(e)) successfully describe the shape of the inclusion as a low strain region in the center. Furthermore, the strains inside the inclusion and in the outer matrix are almost constant, respectively, which is in accordance with the FEA result. The elastogram from NP-64 seems more delicate and smoother, but the one from NP-24 also demonstrates clearly discernable patterns. In TSE elastograms (Figure 3.9(b) and 3.9(f)), the inclusion is readily detectable; however, the shape of the inclusion is distorted and the matrix strain is inconsistent and noisy. The elastogram from NP-64 (Figure 3.9(b)) shows reasonably preserved pattern, but that from NP-24 (Figure 3.9(f)) is much more degraded, particularly in matrix region. In DSE elastograms (Figure 3.9(c) and 3.9(g)), low strain region corresponding to the inclusion is observed in the center, but the patterns are significantly dispersed and degraded. PSE elastograms (Figure 3.9(d) and 3.9(h)) also show the existence of the inclusion; however, the shape of the inclusion and the matrix strain are much more distorted and noisier than RPSE.

Strain plots along the vertical centerline of numerical phantoms (Figure 3.10) show the comparison between the FEA results and those from three estimators. For NP-64 (Figure 3.10(a)), both RPSE and TSE plots show good agreement with the FEA plot, and clearly indicate the existence of stiff inclusion in the depth between 15 mm to 25 mm. DSE plot is over-smoothed, and the shape and size of the inclusion are hard to be identified. PSE plot shows similar trend to FEA plot, however, it varies significantly within the inclusion and in the matrix, particularly in the deep region between 30 mm and 35 mm depth. In the strain plots of NP-24 in Figure 3.10(b), the plots from strain estimators present generally large deviations from the FEA plot; RPSE plot still follows the true strain relatively well, while large differences are found in TSE plot, particularly in the matrix region under the inclusion. Over-smoothing is observed in DSE plot, with much more serious manner than for that in Figure 3.10(a)), while PSE shows very noisy and degraded results.

As for the elastograms for gelatin phantom, RPSE (Figure 3.11(a)) describes the shape of the inclusion relatively well. TSE also indicates the existence of the inclusion; however,

the strain patterns are highly noisy and scattered both in the inclusion and in the surrounding matrix. In DSE elastogram (Figure 3.11(c)), the shape of the inclusion is unclear and dispersed; furthermore, there are many degraded spots in the surrounding matrix. The elastogram from PSE (Figure 3.11(d)) fails to describe the inclusion and only shows highly noisy pattern. In the strain plots along the vertical centerline (Figure 3.11(e)), the strain levels inside the inclusion and the matrix are supposed to be constant, respectively; however, both RPSE and TSE plots show significant variations. Since both plots present similar trends, there is a possibility that gelatin phantom was not cured uniformly and material properties were not homogeneous. Meanwhile, DSE plot also shows significant variations in an over-smoothed manner compared to the other plots. PSE plot seems to deviate from the trend of the other plots across the entire depth.

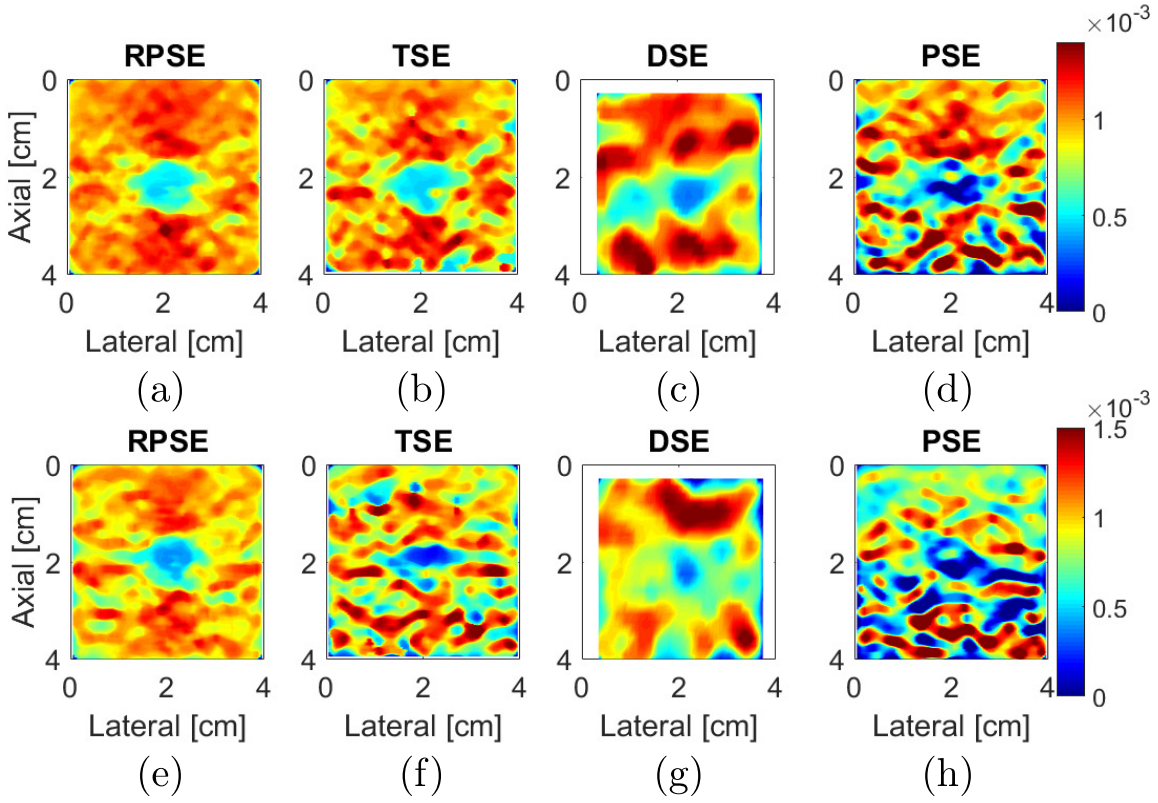

Figure 3.9: Elastograms from NP-64 numerical phantom generated by: (a) RPSE, (b) TSE, (c) DSE and (d) PSE; elastograms of NP-24 generated by: (e) RPSE, (f) TSE, (g) DSE and (h) PSE, respectively.

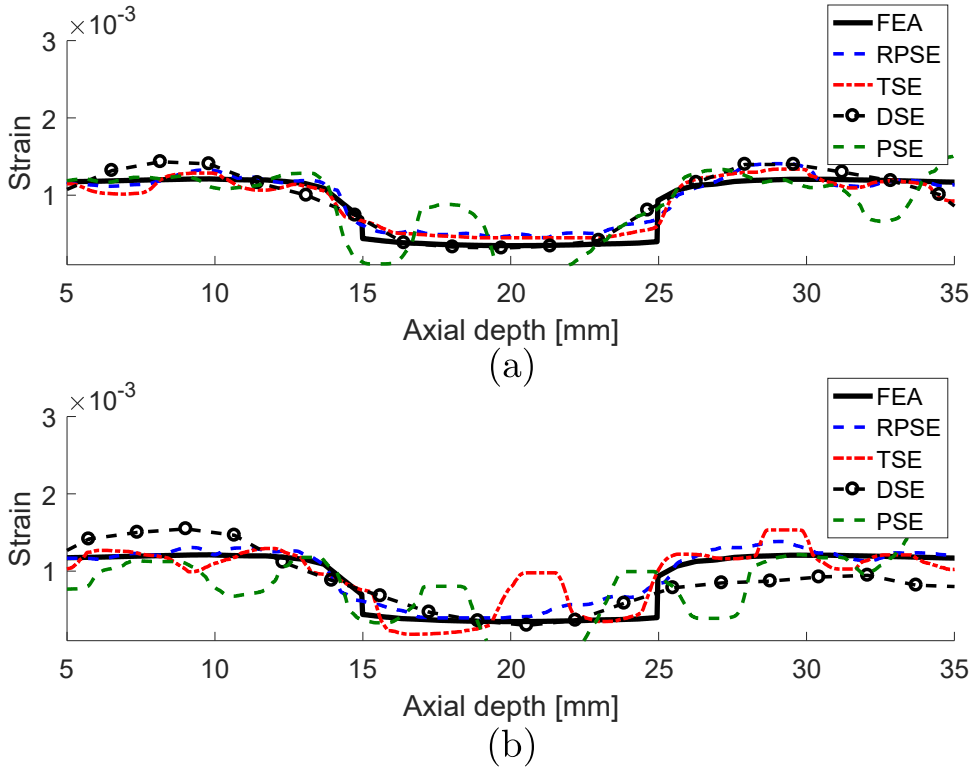

Figure 3.10: Strain plots along the vertical centerline of (a) NP-64 and (b) NP-24 estimated by FEA, RPSE, TSE, DSE and PSE, respectively.

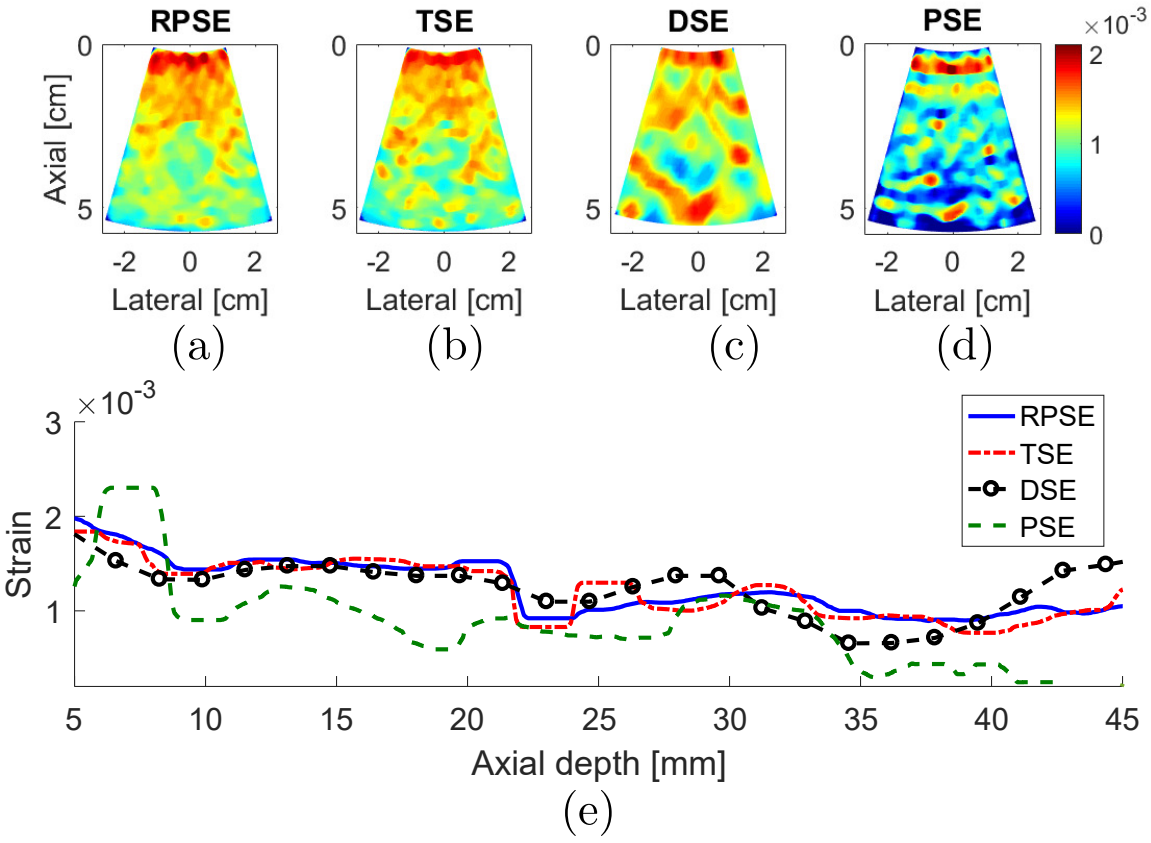

Figure 3.11: Elastograms from the gelatin phantom generated by: (a) RPSE, (b) TSE, (c) DSE and (d) PSE; (e) the strain plots along the vertical centerline estimated by RPSE, TSE, DSE and PSE, respectively.

3.4.3 Image Quality Measures

Two image quality measures, SNRe and CNRe, were evaluated on 11 frames of elastograms produced by RPSE, TSE, DSE and PSE, as presented in Figure 3.12 using box plots. Note that the width of the band plots along vertical direction represents the dispersion of the measures over the frames. For NP-64 numerical phantom (Figure 3.12(a)), SNRe plot associated with the RPSE elastograms yields the highest median of 6.15, but the dispersion is the largest. The SNRe plot for TSE forms very narrow band with the medians of 4.93, while that of DSE is slightly more dispersed and the median is around 3.1. The lowest SNRe is delivered by PSE at around 2.5. In regard to CNRe plots, RPSE produces the highest median of 53.52 dB followed by TSE (45.33 dB), PSE (34.87 dB) and DSE (30.1 dB). The widths of the CNRe bands for RPSE, PSE and DSE are approximately the same, while that of TSE is widely dispersed. Overall, RPSE shows the best SNRe and CNRe combination with the highest median, while the repeatability over 11 frames is approximately the same.

For the elastograms of NP-24 (Figure 3.12(b)), the SNRe for RPSE also shows the highest median at around 5.22 followed by TSE (3.27), DSE (2.74), and PSE (1.81). The width of SNRe band is the narrowest for both RPSE and PSE and becomes wider in the order of TSE and DSE. As for CNRe, PSE yields slightly higher median at around 49.14 than RPSE (47.62dB), followed by TSE (33.03 dB) and DSE (23.07 dB). In regard to the dispersion of CNRe, RPSE shows the narrowest level and the others are almost same.

For the elastograms of gelatin phantom (Figure 3.12(c)), the SNRe for TSE shows slightly higher median at around 4.61 than RPSE (4.39); however, its dispersion is larger than that for RPSE. PSE produces the lowest SNRe (1.98) and DSE (3.88) shows the largest dispersion. As for CNRe, both RPSE and TSE produce similar medians at around 40.65 dB and 40.44 dB, respectively, with almost equivalent band width. PSE produces slightly lower CNRe (30.43 dB), while DSE is associated with the lowest median (16.77 dB) and much wider band width. Overall, both RPSE and TSE show similar level of image qualities while RPSE demonstrates slightly better repeatability.

In conclusion, the results of image quality measures suggest that RPSE produces the best elastogram from the numerical data sets; however, for the experimental data set from gelatin phantom containing relatively high level of noise, RPSE and TSE shows similar

performance, while PSE and DSE produces much lower SNRe and CNRe in all cases.

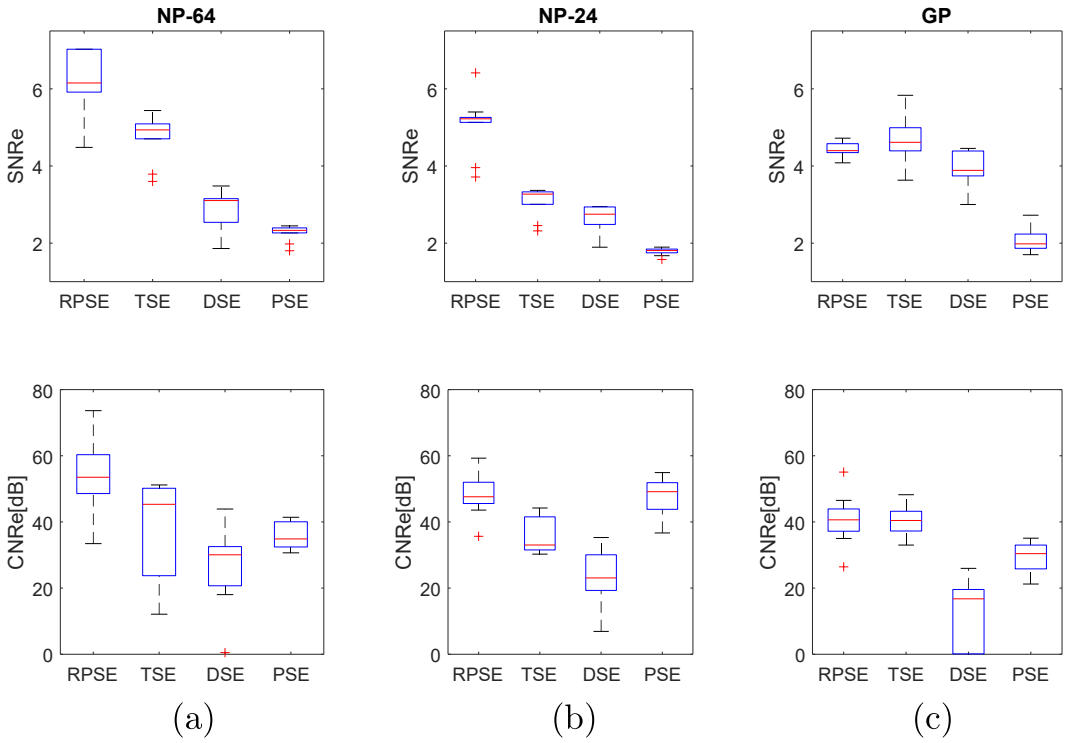

Figure 3.12: SNRe and CNRe for the elastograms from: (a) NP-64, (b) NP-24, and (c) the gelatin phantoms.

3.4.4 Computational Efficiency

Since the correlation function for strain estimation imposes high computational load while portable ultrasound device has limited resources, computational efficiency is one of the critical factors in assessing the strain estimators for portable ultrasound. Computation times were measured on a Windows 7 computer (2.3 GHz, i7-3610 CPU with 12 GB RAM, ASUS-K55VD) using in-house developed MATLAB code.

Figure 3.13presents the computational times for the strain estimators to generate elastograms from numerical and gelatin phantom data sets. Overall, both phase-based strain estimation methods (RPSE and PSE) delivered much higher computational efficiency than correlation-based methods (TSE and DSE) by a significant margin. In order to perform the calculations for the strain estimation over 11 frames from NP-64 numerical data set of the size 1600 (length) $\times$ 80 (scanline) per each frame (Figure 3.13(a)), RPSE and PSE spent only 0.64 and 0.53 seconds, respectively, while 65.95 and 77.92 seconds were taken by TSE and DSE, respectively. For each RF frame, RPSE and PSE recorded only 0.06 and 0.05 second computation times, while TSE and DSE spent around 6 and 8 seconds. Similar amount of computation times were required for the elastogram from NP-24 phantom (Figure 3.13(b)) by each method, with RPSE and PSE taking much less time (around 0.6 seconds) than TSE and DSE (63.57 and 85.56 seconds, respectively). The computations of each frame were 0.06, 0.05, 5.78, and 7.78 seconds by RPSE, PSE, TSE, and DSE, respectively.

The gelatin phantom data set is composed of 11 frames with each frame size of 2000 (length) $\times$ 66 (scanline). The computation of the whole frames took only 0.69 seconds for RPSE and 0.59 seconds for PSE, while TSE and DSE recorded 66.25 and 99.46 seconds, respectively. Both RPSE and PSE also show almost 100 times faster computational performance than TSE and DSE in the strain estimation of each frame (0.06 seconds vs. 6.3$\sim$7.68 seconds). Computation time for each frame using RPSE can be converted to 16.6 fps (frame per second) that can be regarded as quasi-real-time processing. This implies that RPSE, without using C programming and MEX interface in MATLAB, may be an efficient strain estimation algorithm for portable ultrasound, and although not as fast as high-end console style ultrasound device implemented with dedicated hardware (around

30 fps), RPSE running on a general personal computer have the potential to provide near-real-time elastography.

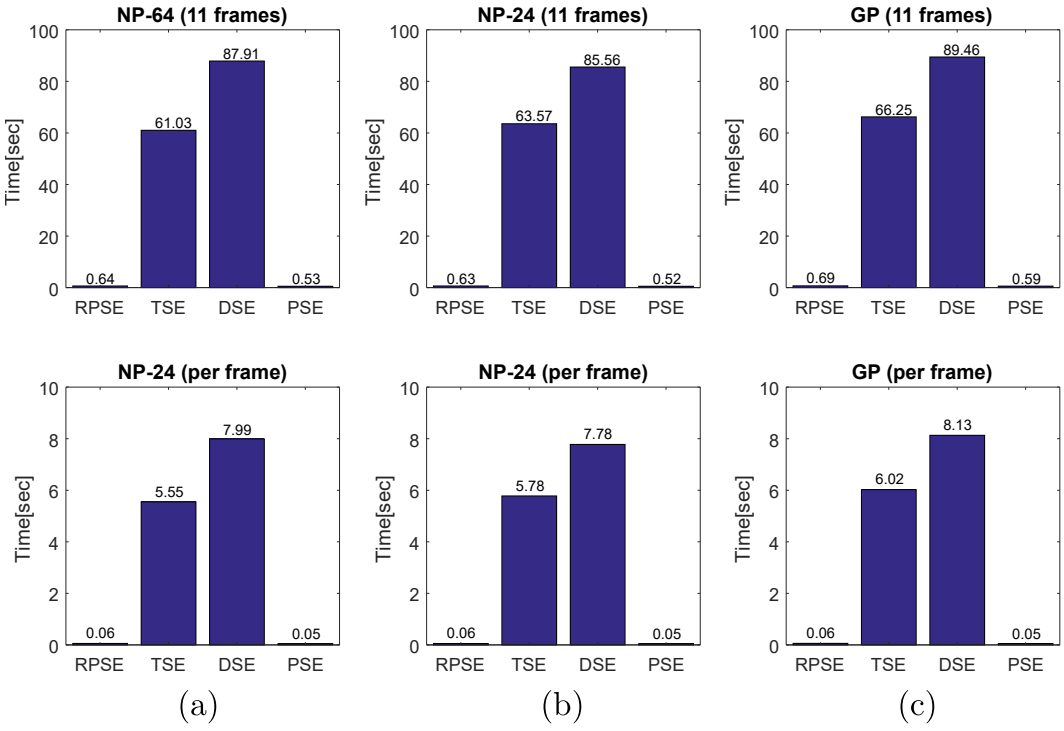

Figure 3.13: Computational times spent by RPSE, TSE and DSE methods for generating the elastogram(s) from: (a) NP-64 numerical phantom, (b) NP-24 numerical phantom, and (c) the gelatin phantom.

3.4.5 Comparison of the Strain Estimators

Strengths and weaknesses of each strain estimator identified through the above evaluation processes can be summarized as below. The strengths of RPSE lie in good accuracy of elastogram, high computational efficiency, and easy parameter setting. As discussed above, RPSE demonstrated the best image quality measures for numerical phantoms and the faster computation speed than those of both TSE and DSE. Moreover, parameter setting for RPSE is straightforward because it directly estimates the displacement from the phase delay between a pair of RF data sets, and does not require any searching process. On the other hand, RPSE has the phase limitation that it cannot estimate the displacement larger than a half ultrasound wavelength. However when the frame rate of ultrasound devices is over 15 fps, the displacement between consecutive frames in elastography practice is mostly within this limitation. Therefore, the phase limitation of RPSE is not a significant concern to implement the elastography in the portable US device. However, if the frame rate is very low, or the movement of the target object is fast, this can cause a problem.

The strengths of TSE are decent accuracy of elastogram and the robustness in estimating the large displacement. Unlike the RPSE with phase limitation, TSE does not have the displacement limitation because the correlation function finds the maximum correlation value throughout the searching region of which the size can be easily adjusted to increase the measurement range. However, due to the correlation algorithm involving intensive computation, TSE requires higher computational cost and more sensitive parameter settings than those for RPSE.

The benefit of DSE is that it uses B-mode images, and does not require raw RF data sets. Since most of commercial US scanners provide B-mode images, DSE can be an affordable option to generate the elastograms from various types of medical imaging modalities. However, the accuracy of DSE is relatively low and the computational cost is extremely high due to its 2D block matching algorithm. Also, the parameter settings in DSE for its 2D correlation is very sensitive and requires multiple empirical trials to obtain acceptable quality elastogram images.

The PSE demonstrates the best computational efficiency among all methods tested. However PSE delivers the highest error levels (lowest SNRe values) because it is sensitive

to the variation of acoustic parameters. Moreover, PSE cannot be directly applied to the current portable ultrasound device, because pulse repetition period, an essential parameter for velocity estimation, is not constant, but varies with data size and communication environment.

3.5 Conclusion

In order to overcome the limited computational performance of portable ultrasound device in realizing elastography function, a robust phase-based strain estimator (RPSE) which is independent of the speed of sound, sampling frequency and pulse repetition period was proposed. Through the comparative study with other representative strain estimation methods including time-delay and displacement-gradient strain estimators, it was found that the RPSE method can deliver the acceptable level of elastography in terms of elastogram quality and computational efficiency. For the numerical phantom data, RPSE showed the best SNRe and CNEe values than the other methods. TSE also generated decent quality of elastograms; however, due to its high sensitivity to signal noise, estimated strain values were locally deviated from the true strains estimated by FEA. As for the experimental data set from the gelatin phantom, RPSE and TSE demonstrated similar performance, while PSE and DSE delivered much worse SNRe and CNRe levels in all cases, respectively. One of the greatest strength of RPSE lies in the computational efficiency; it demonstrated almost 100 times faster computation speed than TSE and DSE in strain estimation. Although PSE can perform the computation almost the same as or even faster than RPSE, its accuracy is much lower than RPSE. The results suggest that the RPSE be a suitable algorithm to perform real-time elastography processing for portable ultrasound. However, RPSE has the limited displacement range between the frames, corresponding to a half ultrasound wavelength; thus, it may not be an optimum strain estimator for fast-moving tissues.

Chapter 4

Overview of Compressive Sensing

4.1 Compressive Sensing

Shannon-Nyquist theorem, also known as the sampling theorem, has had a great impact on digital signal processing field [62, 63, 64]. This theorem plays a major role in offering the minimal frequency required to sample and reconstruct a continuous-time signal (often called analog signal) in the digital signal processing. In other words, the sampling theorem provides a fundamental bridge between analog signals and digital signals in order to fully recover the analog signals. Based on Shannon-Nyquist theorem, an analog band-limited signal can be fully reconstructed from its samples if the sampling rate is greater than twice the maximum frequency presented in the recorded signal, the so called Nyquist rate [65]. Furthermore, the digital signal processing following Nyquist rate has entirely replaced analog signal processing methods and offered high fidelity, inexpensive, and robust measurement system.

With recent incredible advance of digital technology demonstrating high density images, the sampling rate of the digital signal processing required to compute, record, and communicate the considerable amount of data have significantly increased. Moreover, the cost of the digital signal processing in many emerging digital applications has become extremely expensive. Also, the digital signal processing following the conventional Nyquist

rate [65] is often unable to create high fidelity for the large data in recent emerging applications. Lossy compression, a data encoding method, has been used to reduce data size for recording, processing, and communicating signal. Since lossy compression preserves only the large coefficients of a signal, certain level of fidelity loss would be inevitable. The process used in lossy compression is also called sparse signal approximation, and this concept is most commonly used in common compression standards for multimedia data such as JPEG, JPEG2000, MPEG, and others [66]. Although lossy compression enables to reduce storage space, computation times, and communication load, the acquisition process should satisfy the conventional sampling requirement according to Nyquist sampling rate.

Recently compressive sensing (CS) theory [67, 68] has been rigorously studied as a means to break the conventional Nyquist sampling rate and thus can significantly decease the amount of measurement signals without remarkably sacrificing signal quality. According to CS theory, discrete signals admitting a sparse representation in the domain of an adequate linear transform can be significantly compressed from far fewer samples and then be recovered accurately through the use of reconstruction methods. With the obvious benefit of data reduction, CS theory has been typically exploited for the medical imaging applications where the numerous amounts of signal processing are required. For example, dynamic magnetic resonance imaging (MRI) [69, 70, 71], computed tomography (CT) [72] and photoacoustic tomography (PAT) [73] are the most representative CS applications. The performances of a CS framework such as compression rate and fidelity would vary relying on its signal sparsity and reconstruction algorithm. Thus, the optimal CS performances are achieved by selecting the adequate sparse representation basis and reconstruction algorithm, and implementing the best combination of them. CS model basis showing a sufficient sparse representation of a signal has been well researched, and based on early results [74, 67, 75, 76], a unique solution for the specific signal reconstruction problem can be provided by selecting a suitable CS model basis. Solution of a optimization problem maximizing the sparsity of the measurement signal has been often exploited to reconstruct the original signal. In early researches, convex optimization algorithm such as L_1 minimization [74, 75, 76] and greedy methods [77, 78] are popularly used as a deterministic reconstruction method. Recently, the CS reconstruction problem has been also represented as a stochastic algorithm using Bayesian rule [79, 80].

4.2 Sparsity Representation

Sparsity in CS exploits the idea that the information rate of an analog signal may be much smaller than suggested by its bandwidth, or that a number of non-zero signal in a digital measurement signal is incomparably smaller than its signal length [68]. Therefore, many natural signals could be represented as a concise linear transform when expressed in the appropriate basis, in the sense that the natural signals are usually significantly compressible.

Mathematically, CS enables the reconstruction of a signal $x \in \mathbb{R}^n$ with sparse representations from a small number of physical measurements $y \in \mathbb{R}^m, m \ll n$. The compressed measurement data y is acquired using the so-called sensing basis Φ, thus it can be expressed:

$$y = \Phi x, \tag{4.1}$$

where Φ is an $m \times n$ matrix. Random Gaussian ensemble or Bernoulli matrices, which are highly incoherent to the sparse representation achieved by basis matrix Ψ, are often used as a sensing basis Φ which is designed such that compressible signals x can be recovered exactly from the compressed data y.

As mentioned, most natural signals have concise representations when expressed in a convenient basis and the natural signals are generally considerably compressible [68]. Consider any signal $x \in \mathbb{R}^n$ that can be represented in some model basis Ψ (where Ψ is an $n \times n$ matrix with $\Psi_1, \ldots, \Psi_n$ as column), which can be an orthonormal basis, a Fourier transform basis, or other basis depending on the measurement signal. The sparse representation of signal x is:

$$x = \sum_{i}^{n} v_i \Psi_i = \Psi v, \tag{4.2}$$

where v is an $n \times 1$ column vector and x and v are the same representation of a signal with x in the time domain and v in the Ψ domain. In the sparse representation, v has only $k < m \ll n$ non-zero coefficients (so-called k-sparse) and the signal x is a linear combination of just k basis vectors. When using a random matrix as the sensing matrix Ψ, CS can closely reconstruct the k-sparse vector $x \in \mathbb{R}^n$ with high probability with just

$m \geq k \log \frac{n}{k}$ random measurement. By combining Eq. (4.1) and (4.2), the measurements can be written as:

$$y = \Phi\Psi v = Av, \tag{4.3}$$

where A is an $m \times n$ full rank matrix (the m rows of A are independent), and obeys the so-called restricted isometry property (RIP) which proves the general robustness of CS as a sufficient condition [68]. The isometry constant δ_k of a matrix A as the smallest number is defined as:

$$(1 - \delta_k) \|v\|_{l_2}^2 \leq \|Av\|_{l_2}^2 \leq (1 + \delta_k) \|v\|_{l_2}^2 \text{, for each k} = 1, 2, \ldots. \tag{4.4}$$

The sufficient condition (RIP) guarantees that the solution of $\|Av\|_{l_2}^2$ (signal energy) in Eq. (4.4) is bounded between an upper bound and a lower bound. When A satisfies the RIP condition, A approximately preserves the Euclidean length of k-sparse signals. This property implies that k-sparse vectors cannot be in the null space of matrix A. To reach the maximum incoherence between Φ and Ψ, both sensing matrix Φ and model basis Ψ should be chosen carefully, so that the sparse representation by the model basis Ψ achieves the minimum k-sparse vectors. Schematic diagram of the typical compressive sensing sampling processes using random Gaussian sensing matrix Φ and discrete cosine transform matrix Ψ is illustrated in Fig 4.1.

4.3 Compressive Sensing Reconstruction Methods

Two classes of the optimization algorithms have been mainly employed to reconstruct the optimal values of sparse signal v in Eq. (4.3). The first one uses deterministic optimization algorithms including L1 minimization (L1) algorithms [74, 75, 76], and another uses stochastic algorithms using the Bayesian learning framework, such as block sparse Bayesian learning (BSBL) [79, 81].

The deterministic optimization algorithms using convex optimization or Greedy methods have been used in early researches [74, 67, 75, 76]. Candès et al. [82] proposed ℓ_0 norm as a good sparsity operator for solving the following ℓ_0-minimization problem:

$$\hat{v} = \arg\min_{v \in \mathbb{R}^n} \|v\|_{\ell_0} \text{ subject to } y = Av. \tag{4.5}$$

The ℓ_0-minimization problem in Eq. (4.5) produces a unique solution for the sparse signal v if A is a proper over-complete orthogonal basis [75]. Unfortunately, computational cost of solving Eq. (4.5) is extremely expensive because the solution would require searching among all possible combinations of columns of A (so called non-deterministic polynomial time (NP) hard). Using sub-optimal greedy algorithm [83], this solution also has been solved by successively adding non-zero components to a sparse approximation of v.

A basis pursuit (BP) problem, also called L1 minimization, which exploits ℓ_1 norm [84, 85], was proposed to solve the following modified optimization problem:

$$\hat{v} = \arg\min_{v \in \mathbb{R}^n} \|v\|_{\ell_1} \text{ subject to } y = Av. \tag{4.6}$$

The L1 minimization based on BP optimization problem provides a significant advantage. Unlike ℓ_p norm ($0 < p < 1$ that is non-convex), the ℓ_1 norm is a convex function offering a global minimum. Compared to exact sparse solutions based on ℓ_0 norm, L1 minimization problem is much simpler problem. Using the RIP condition, the equivalence of optimization algorithms based on both ℓ_0 and ℓ_1 has been proved in [85] and then CS reconstruction algorithm based on L1 minimization is popularly used as the standard CS reconstruction algorithm.

On the other hand, the unknown sparse signal v can also be reconstructed by exploiting the principle of Bayesian inference as a stochastic algorithm. In the stochastic approach, a priori probability density functions (pdf's) are associated with each of the unknown variables v, and the Bayes law is used to find the posteriori probability to be maximized, such that:

$$p(v|y) \propto p(y|v)p(v), \tag{4.7}$$

where $p(y|v)$ represents the likelihood and $p(v)$ contains prior information about the unknown sparse v. Assume that the A matrix is known and the noise z is approximated by an additive Gaussian noise with zero mean and unknown variance σ^2. Then the sparse coefficients v and the noise variance σ^2 are the quantities of CS estimate based on Bayesian framework. The associated Gaussian likelihood model is given by [81]:

$$p(y|v, \sigma^2) = (\pi\sigma^2)^{-n} \exp\left(-\frac{1}{\sigma^2} \|y - Av\|_{l_2}^2\right). \tag{4.8}$$

By introducing an a priori on the coefficients to be recovered $p_0(v)$, the sparsity model is modeled as follows:

$$p_0(v) \propto \exp\left(\|v\|_{l_0}\right). \tag{4.9}$$

This Bayesian approach converts the CS reconstruction problem recovering the sparse coefficients of v into a Bayesian linear-regression problem with the prior constraint which v is sparse.

Recently, "Block Sparse Bayesian learning" (BSBL) algorithms have been proposed to further improve reconstruction performance of wireless electrocardiogram (ECG) applications [79, 86]. By exploring and exploiting the intra-block correlation that correlates the entries in each block, the recovery performance of BSBL was greatly improved compared to other methods ignoring the intra-block correlation.

4.4 Evaluation Metrics for CS

To quantify the compression rate, the subsampling rate (SR) is defined as

$$\text{SR}\% = \left(1 - \frac{m}{n}\right) \times 100, \tag{4.10}$$

where n and m are the number of the original and undersampled measurements, respectively.

The accuracy of the B-mode and elastograms images from CS reconstruction are quantified by comparing them with the images from the original data through the mean absolute error (MAE) given by

$$\text{MAE} = \frac{1}{n}\sum_{i=1}^{n} |I_{o_i} - I_{r_i}|, \tag{4.11}$$

where n is the total number of the image data, and I_{o_i} and I_{r_i} are the intensities of both original and reconstructed images, respectively.

As previously described in Section 2.4, the elastographic image quality measures including SNRe and CNRe are also used to evaluate image quality of the elastograms reconstructed by a CS framework.

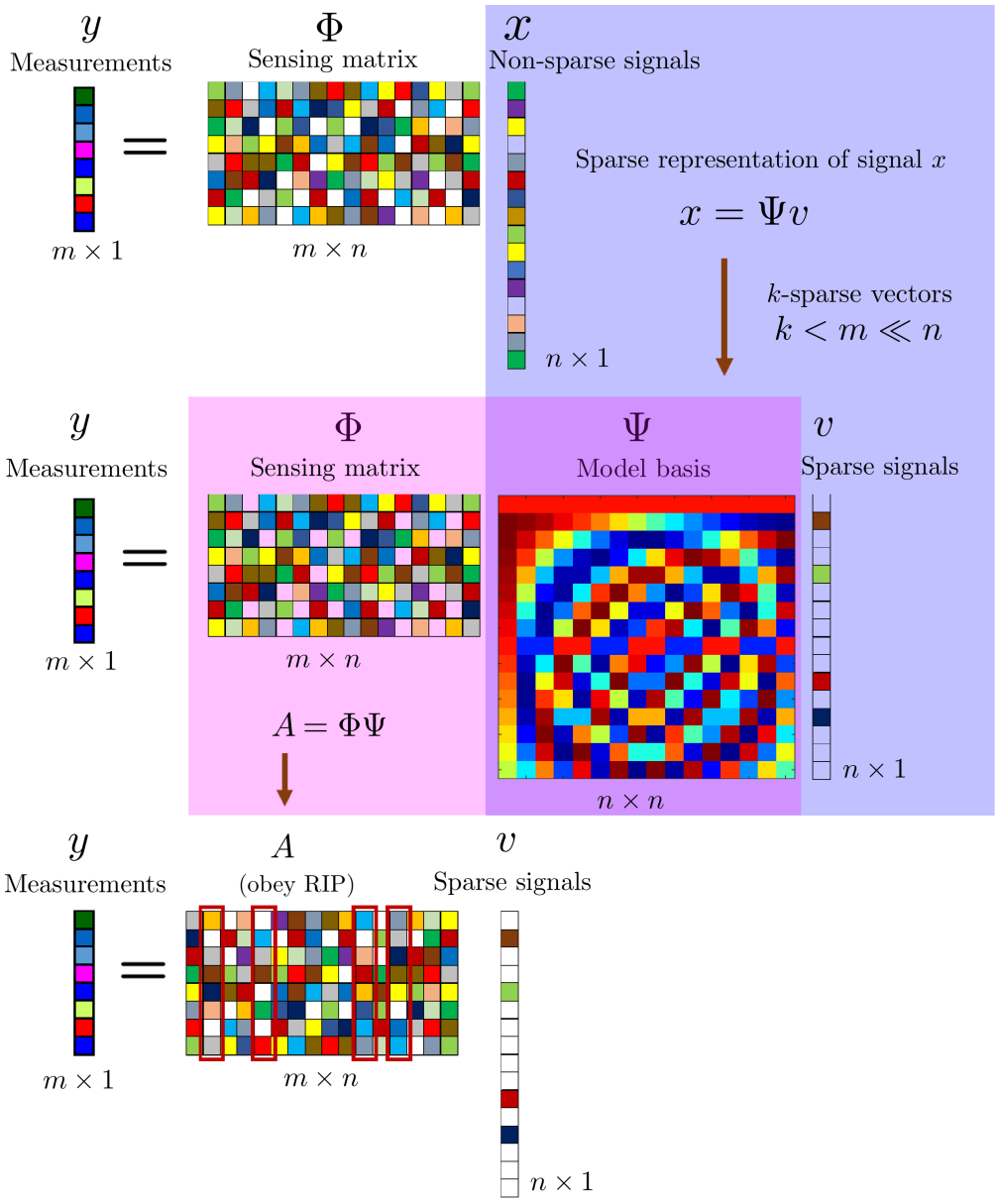

Figure 4.1: Compressive sensing sampling processes with random Gaussian matrix Φ and discrete cosine transform matrix Ψ. The sparse vector v is sparse with $k = 4$. The four columns corresponding to non-zero value k_i are highlighted on matrix $A = \Phi\Psi$ and the compressed measurement vector $y \in \mathbb{R}^{m \ll n}$ is a linear combination of these four columns.

Chapter 5

Compressive Sensing for Elastography

5.1 Introduction

Insufficient data transfer speed of the wireless portable ultrasound device is one of challenges that make the portable devices difficult to achieve the elastography functionality as described in Section 1.3. Recently compressive sensing (CS) theory has been actively studied, as a means to overcome the limitation of the conventional Nyquist rate [65, 62, 63] by leveraging the inherent compressibility of most natural signals to allow recovery from far fewer measurements than the Nyquist rate would suggest. CS allows significant reduction of the measurement data, and thus of time for signal processing and data communication while maintaining output signal quality. Moreover, CS can reduce image artifacts and noise power when using the same number of measurements. Given all the benefits of CS, I hypothesize that CS could be a feasible solution to overcome the limitations of portable ultrasound in realizing elastography function. On the other hand, CS construction imposes a new computational load to the paired computing device (lab top or tablet PC); however, I also hypothesize that with the increase of computing power of such devices, the benefits of CS outweigh the disadvantages. Although medical imaging is one of areas can benefit from CS, the adoption of CS in ultrasound imaging is relatively new [80]. Also, most of

the related studies have been focusing on conventional pulse-echo B-mode imaging or suggesting several random sampling strategies [79]. To the best of author's knowledge, none of them has attempted to apply CS to elastography, particularly for portable ultrasound where the reduction of measurement data to be transferred through wireless communication is crucial. Therefore, the objective of this section is to examine the feasibility of CS for elastography and to find the most efficient CS framework for implementing elastography function on portable ultrasound. Since the CS framework can also be used for B-mode reconstruction using sub-sampled RF data for reducing wireless communication data, the performance of the frameworks for reconstruction of B-mode images is also investigated. It needs to be mentioned that the quality of CS reconstruction highly depends on both the reconstruction algorithms and the sparsity of the signal representation. Therefore, this study includes composing various CS frameworks associated with different model bases and reconstruction algorithms and assessing the quality of the B-mode images and elastograms from the RF data sub-sampled and reconstructed by each framework.

5.2 CS Frameworks

CS framework applied to portable ultrasound device in this research follows the procedure as illustrated in Figure 5.1. First, a pair of original RF data sets from CS sampling are collected and compressed by the portable US device (Figure 5.1, above). The undersampled (compressed) RF data sets are then transmitted to a laptop or mobile device through the Wi-Fi network established between them. The laptop computer (or mobile device) recovers the compressed data sets using a CS reconstruction algorithm, and then generates the elastogram using the RPSE method which is described in the Section 3.2 (Figure 5.1, bottom).

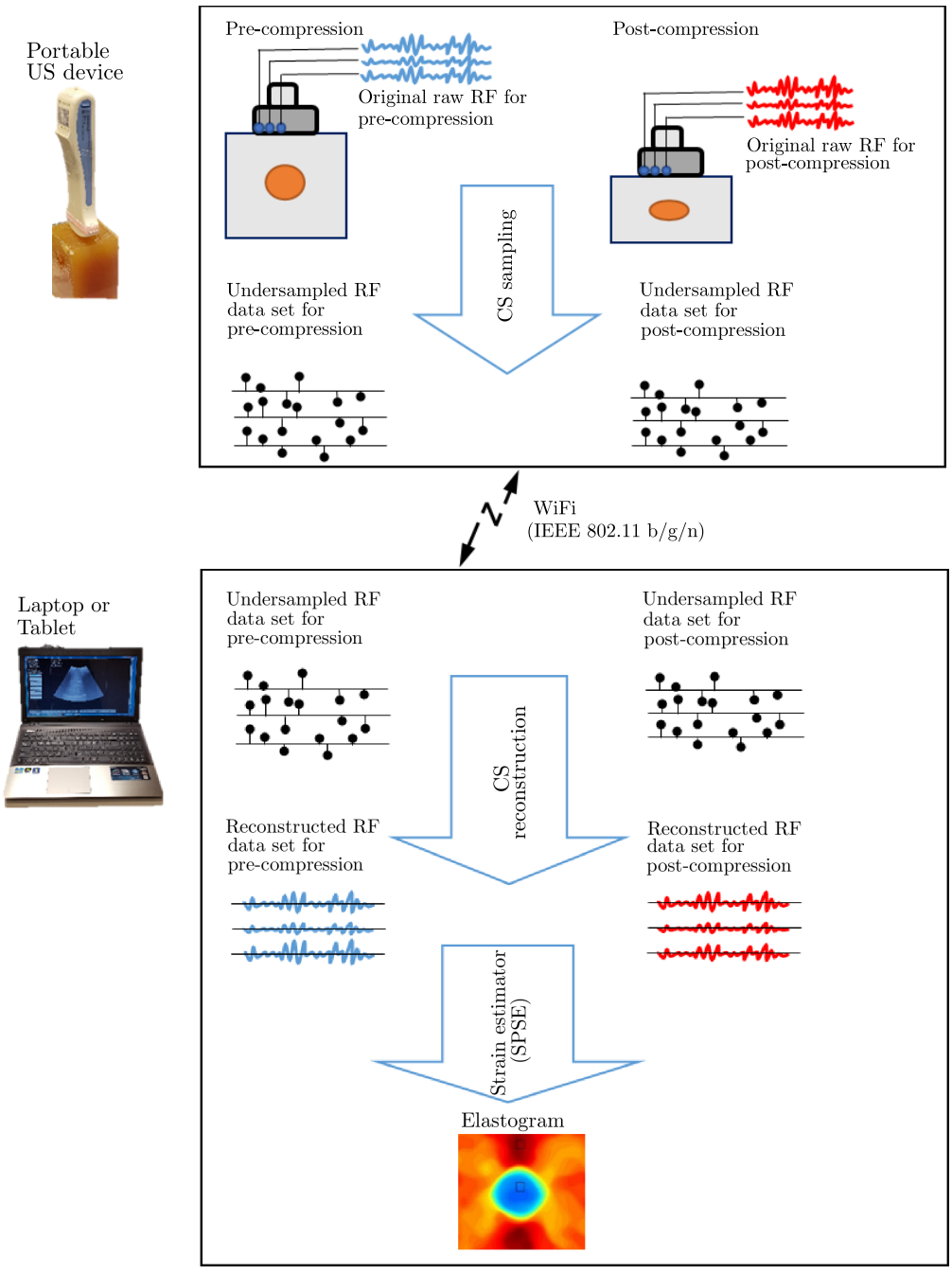

Figure 5.1: Schematic of the CS procedure for generating elastogram in portable US device

5.2.1 Model Bases for CS sampling

CS performance strongly depends on signal sparsity representation in the reconstruction model basis Ψ [81]; however, since the raw RF data in ultrasound shows an oscillatory pattern, it is not trivial to find the adequate sparsity representation with any basis. In CS, discrete Fourier transform (FT), discrete cosine transform (DCT), and wavelets have been often considered as candidates for signal sparsity representation. When natural signals are represented in FT or DCT domain, most of FT or DCT coefficients are zero or small enough to consider zero values. Therefore, both FT and DCT model bases are often considered as a signal sparsity representation in the conventional CS framework. If a natural signal is spare in FT domain, the FT model basis is an $n \times n$ orthogonal matrix whose sparse representation in frequency domain is given by

$$v^{FT}(u) = \mathbf{FT}\left[x(t)\right] = \sqrt{n}\sum_{t=1}^{n-1} x(t)e^{-i2\pi ut/n}, 0 \leq t, u \leq n-1, \tag{5.1}$$

FT sparse signals are only those which are superpositions of sinusoids with frequencies appearing in the lattice of those in FT [87]. In addition, DCT, the most widely used transform for image and video compression systems, is another preferred tool for CS sparse representation. The DCT model basis [88] is also an $n \times n$ orthogonal matrix whose sparse representation in cosine transform domain is given by

$$\begin{aligned} v^{DCT}(u) &= \mathbf{DCT}\left[x(t)\right], \\ &= \sqrt{\frac{1}{n}}, && u = 0, \\ &= \sqrt{\frac{2}{n}}\sum_{t=1}^{n-1} x(t)\cos\frac{\pi(2t+1)u}{2n}, && 1 \leq u \leq n-1, \end{aligned} \tag{5.2}$$

where the function $x(t)$ is the value of $t-$th samples of input signals, and the function $v(u)$, the coefficients of this linear combination, represents DCT coefficients which are the real-valued unlike FT coefficients.

Wave atoms transform (WA), proposed by Demanent and Ying [89], represents the time-dependent Green's function and enables to provide a tight frame of multiscale, directional wave packets obeying a parabolic balance between oscillations and support size,

namely wavelength $\sim$ (diameter)^2 [90]. In other words, the WA offers the exact relationship between the directional wavelets and the Gabor transform which is a special case of the short-time Fourier transform. The name "wave atoms" comes from the property of the transform which also provides an optimally sparse representation of wave propagators [90].

In order to classify various wave-packet transforms as phase-space tiling, two parameters should suffice to index a lot of known wave packet architectures: α to index multiscale nature of the transforms, from 0 (uniform) to 1 (dyadic); and β to indicate the wave packet's directional selectivity, from 0 (best selectivity) to 1 (poor selectivity).In wave atoms, both α and β are defined to be 0.5 [89].

In 1D WA, $f(x)$ and $f(\omega)$ are considered as a 1D Fourier transform pair, where x and ω correspond to the coordinates in the time domain and the frequency domain, respectively. $\varphi_\mu(x)$ denotes the wave atoms, where $\mu = (j, m, n)$ and the integer-valued j, m, n indicate scale, wave number, and location, respectively. Then the indexed point (x_μ, ω_μ) in phase domain is [89, 90]

$$x_\mu = 2^{-j}m, \omega_\mu = \pi 2^j n. \tag{5.3}$$

The elements of a frame of wave packets φ_μ are called wave atoms when

$$|\hat{\varphi}(\omega)| \leq C_M 2^{-j}(1 + 2^{-j}|\omega - \omega_\mu|)^{-M} + C_M 2^{-j}(1 + 2^{-j}|\omega + \omega_\mu|)^{-M}, \text{for all } M > 0, \tag{5.4}$$

and

$$|\varphi(x)| \leq C_M 2^j (1 + 2^j |x - x_\mu|)^{-M} \text{for all } M > 0. \tag{5.5}$$

Generally, wavelets provide a multiscale representation that indexed by scale and location. Similarly, WA produces a multiscale transform with frame elements indexed by scale, location, and orientation parameters. Among the multiscale feature in WA, the index parameter for orientation is useful for adapting to arbitrary local directions of oscillatory patterns [80]. Meanwhile, DCT expresses a finite sequence of data points in terms of a sum of cosine functions (real-valued) oscillating at different frequencies, while FT represents scaled-and-shifted complex vectors in the frequency domain.

In the CS frameworks, reconstruction performance of the CS adopting WA, DCT, and FT model bases were compared to find a relevant sparse representation of the raw RF data

in ultrasound. Since the elastogram used in this study depicts the axial strain field, each basis function is applied to one-dimensional RF signal, and then the measurement signal x is converted to the sparse representation v in the Ψ domain as described in Eq. (4.2). For WA model base, the WA package based on [89] was employed to conduct the forward and inverse WA transform. For DCT and FT, one-dimensional built-in function sets in MATLAB were utilized, with the signal segment size set to 256 for all model bases.

5.2.2 CS Reconstruction Methods

The simulated RF data sets produced from the numerical elastography phantom were sub-sampled by removing 10%-80% of the original samples using a uniform random law. For example, 70% subsampling rate means that 70% of the of the original samples are removed and only 30% are are maintained in the compressed vector y. CS reconstruction was then performed on the sub-sampled RF data by solving the CS minimization problem in Eq. (5.6). Two types of optimization algorithms were adopted: L1 and BSBL.

L1 based reconstruction

In practical applications, the physical measurements are often corrupted by noise and the measurements with additive noise are rewritten as:

$$y = Av + z, \tag{5.6}$$

where z is a unknown error term and bounds the amount of noise in the data ($\|z\|_{l_2} \leq \epsilon$). In order to recover sparse data v in Eq. (5.6), L1 minimization problem in Eq. (4.6) is recasted as [68, 91]:

$$P : \hat{v} = \arg\min_{v \in R^n} \|v\|_{l_1} \textbf{ subject to } \|y - Av\|_{l_2} \leq \epsilon. \tag{5.7}$$

The L1 minimization problem with error terms in Eq. (5.7) is often called as the LASSO [92]. In solving Eq. (5.7), a sparse reconstruction algorithm estimates the optimal values of v in Eq. (5.6), and then the measurement signal x can be converted from Eq. (4.2).

Dantzig selector [93] or a combinatorial optimization algorithm proposed by Haupt and Nowak [94] can be used to solve the L1 minimization problem Eq. (5.7) and can produce provable results if the noise is Gaussian with bounded variance. In the L1 experiments using the l_1-Magic package [91], the accuracy threshold ϵ, signal segment size, and the number of maximum iteration were set to 0.003, 256, and 50, respectively.

Bayesian Learning based reconstruction

CS based on block sparse Bayesian learning (BSBL) framework have been proposed to further improve reconstruction performance of wireless electrocardiogram (ECG) applications [79, 86]. By employing the BSBL framework, the abnormal signal can be partitioned into a concatenation on non-overlapping blocks. Consider a sparse signal v which can be viewed as a concatenation of a number of blocks, such that [95]:

$$v = [\underbrace{v_1, \ldots, v_{d_1}}_{\mathbf{v}_1^T}, \ldots, \underbrace{v_{d_{g-1}+1}, \ldots, v_{d_g}}_{\mathbf{v}_g^T}]^T, \tag{5.8}$$

where $\mathbf{v}_i \in \mathbb{R}^{d_i}$, and d_i $(i = 1, , g)$ are not necessarily identical. Among these blocks, only a few blocks in the signal structure are non-zero, a signal with this structure can be a block sparse signal.

In the BSBL framework, each block $\mathbf{v}_i \in \mathbb{R}^{d_i}$ is assumed to meet a parameterized multivariate Gaussian distribution [95]:

$$p(v_i; \gamma_i, \mathbf{B}_i) \sim \mathcal{N}(0, \gamma_i \mathbf{B}_i), i = 1, \ldots, g, \tag{5.9}$$

with the unknown parameters γ_i and $\mathbf{B}_i$. The first parameter γ_i controls the sparsity of each block in the signal v. When γ_i=0, the corresponding block becomes zero and most γ_i tends to be zero during the learning sequence. It ends up encouraging the better sparsity at the block level because most of signals tend to be zero and to remain a few non-zero values. $\mathbf{B}_i \in \mathbb{R}^{d_i \times d_i}$ is a positive definite matrix, capturing the intra-block correlation structure of the corresponding block i. With the assumption that blocks are mutually uncorrelated, the prior of v is $p(v_i; \{\gamma_i, \mathbf{B}_i\}_i) \sim \mathcal{N}(0, \Sigma_0)$, where Σ_0 is a block-diagonal matrix of $\gamma_i \mathbf{B}_i$. The approach also assumed that the noise vector follows a multivariate Gaussian distribution,

namely $p(z, \sigma^2) \sim \mathcal{N}(0, \sigma^2 I)$. By applying Bayes' rule, the posterior density of v is given by [95]:

$$p(v|y, \sigma^2, \{\gamma_i, \mathbf{B}_i\}_{i=1}^g) \sim \mathcal{N}(\mu_v, \Sigma_v), \tag{5.10}$$

with the mean and co-variance given by:

$$\begin{aligned} \mu_v &= \Sigma_0 A^T (\sigma^2 I + A \Sigma_0 A^T)^{-1} y \\ \Sigma_v &= (\Sigma_0^{-1} + \frac{1}{\sigma^2} A^T A)^{-1}. \end{aligned} \tag{5.11}$$

Once the parameters $\sigma^2, \{\gamma_i, \mathbf{B}_i\}_{i=1}^g$ are estimated by the Type II maximum likelihood procedure [95], the maximum a posteriori (MAP) of v, denoted by $\hat{v}$, can be directly obtained from the mean of the posterior, i.e., $\hat{v} = \mu_v$. Several algorithms [89, 57] have been derived to reconstruct v.

In this work, the bound-optimization based block spare Bayesian learning (BSBL-BO) [95] is selected to show the CS reconstruction performance in generating elastography for portable ultrasound. In the BSBL-BO, the reconstruction of non-sparse signals is accomplished by setting a γ_i-pruning the threshold to a small value. The threshold value is used to prune out small γ_i during iterations of the algorithm. In the BSBL experiments using the BSBL-BO package [95], the segment length and block size, the accuracy threshold ϵ, and the maximum iteration were set to 256, 12, 10^8 and 7, respectively.

5.3 Numerical Phantoms

Numerical phantoms were developed to perform the virtual ultrasound experiment to evaluate the performance of various CS frameworks on image reconstruction. Two types of numerical phantoms were modeled: echoic and elastography phantoms.

5.3.1 Echoic Phantom

An echoic phantom contains arrays of hyperechoic and hypoechoic inclusions [80] to assess the performance of CS on the recovery of B-mode images. Using Field II [59, 60], an

open-source MATLAB-based ultrasound simulation code, RF signals from a numerical phantom of size $50 \times 10 \times 55$ mm^3 were simulated. A 192-element linear array probe with the center frequency 3.5 MHz was modeled to generate the regular ultrasound B-mode images. The numerical phantom was composed of a total of 100,000 point scatterers, four hyperechoic, and four hypoechoic inclusions of the diameter of 6 mm. The hyperechoic inclusions mimicked the malignant tumour with round hyperdensities (BiRads 4 or 5), while hypoechoic inclusions simulated benign cysts filled with liquid without any scatterers (BiRads 1 or 2). The standard deviation of the scatterers' amplitude distribution inside the hyperechoic inclusions was ten times that of the background. The spatial distribution of the scatterers in the hyperechoic inclusions and the background was modeled as uniform, and the amplitude of these regions followed a zero mean Gaussian distribution, respectively.

5.3.2 Elastographic Phantom

An elastography phantom was constructed by combining a finite element analysis (FEA) model and Field II code. Using commercial FEA code (Abaqus/CAE 6.10) (Figure 5.2, upper left), a linear elastic phantom of the size $40 \times 50 \times 10$ mm^3 was modeled to have a stiff cylindrical inclusion (10 mm) in the soft matrix. To acquire the acceptable level of ultrasound echo signal, the FEA model was meshed with approximately 427,000 3D quadratic tetrahedron elements and 77,000 nodes. The elastic moduli of the matrix and the inclusion were set to 20 kPa and 100 kPa, respectively, mimicking a carcinoma in breast tissue. Poisson's ratio of 0.49 was applied to the whole phantom. The vertical movement of the bottom surface of the phantom was constrained while 0.1% axial compressive strain was applied to the top surface. The coordinates of each node were determined and recorded by FEA as the deformation field data sets. Then Field II code was used to add random scatterers to the nodal displacements and generate the corresponding pre- and post-deformation RF signal data (Figure 5.2, upper center). The amplitudes of the random scatterers were kept constant throughout the phantom, thus the inclusion could not be detected in the RF signal or in the B-mode image. In order to simulate the portable ultrasound device, a linear probe having 152 ultrasound elements and 24 active elements was virtually modeled with Field II. The center frequency of the transducer was placed at 3.5 MHz and the sampling

rate of RF signals was set to 28 MHz. The speed of sound through the phantom was set to 1,540 m/s. With this setting, Field II generated 128 simulated RF lines (A-lines) with each line containing 2,589 samples across the phantom depth. Parameters for both echoic and elastography phantoms are listed in Table 5.1. The robust phase-based strain estimator (RPSE) was applied to the RF data sets from CS reconstruction (Figure 5.2, upper and lower right) and the strain fields were estimated from the reconstructed RF dataset (Figure 5.2, lower center). The differences between the strain estimates and the true strains computed by the FEM were regarded as estimation errors (Figure 5.2, lower left).

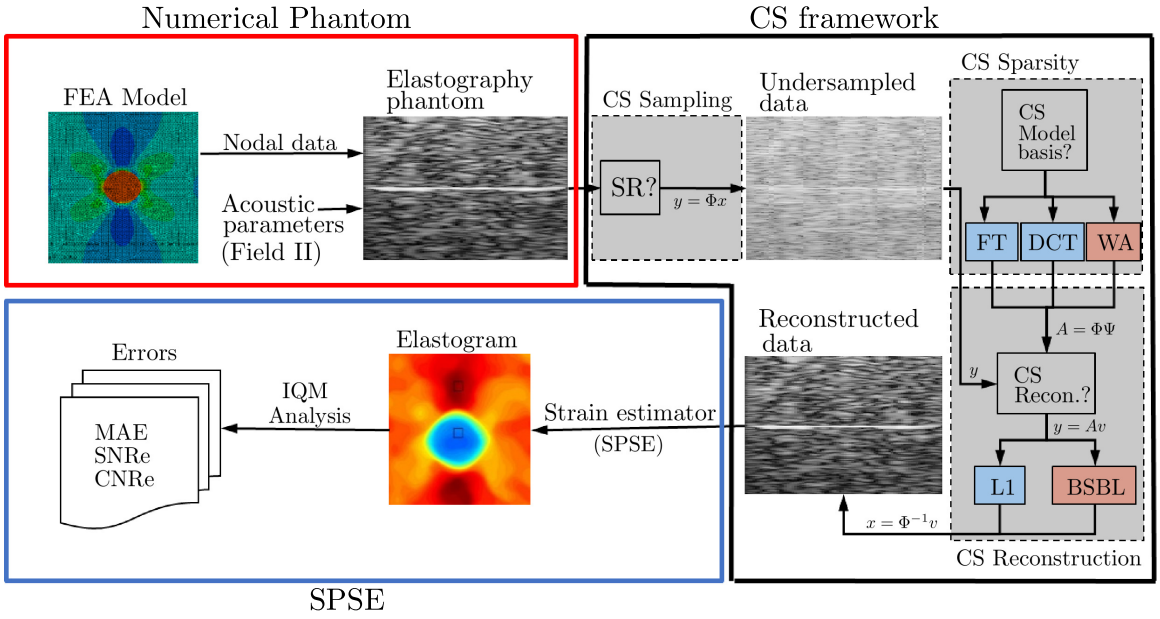

Figure 5.2: Schematic of the procedure to construct a virtual elastograpy phantom and to produce elastogram from the undersampled RF data of the phantom using CS reconstruction.

Table 5.1: Acoustic parameters for numerical phantoms

Parameter	Echoic phantom	Elastography phantom
Phantom size	$50 \times 10 \times 55$ mm^3	$40 \times 50 \times 10$ mm^3
Center frequency	3.5 MHz	3.5 MHz
Sampling frequency	28 MHz	28 MHz
Width	0.44 mm	0.44 mm
Height	5 mm	5 mm
Kerf	0.022 mm	0.022 mm
Number of elements	192	152
Transmit elements	64	24
Receive signals considered	128	128
Transmit/receive focus	50 mm	50 mm

5.4 Results and Discussion

5.4.1 Evaluation of B-mode reconstruction

B-mode images the produced by various CS frameworks formed by combining one of the two reconstruction algorithms (L1 and BSBL) and one of three model bases (FT, DCT and WA), respectively, were evaluated as shown in Figure 5.3 and 5.4 to demonstrate the general CS application in medical ultrasound. To compare the quality of reconstructed B-mode images, I selected a 50% subsampling rate in all cases when generating the elastograms.

As for the echoic phantom containing four hyper- and hypoechoic inclusions (Figure 5.3), both L1 (Figure 5.3(a)) and BSBL (Figure 5.3(b)) algorithms were able to recover the detailed patterns of the phantom, and their hyper- and hypoechoic inclusions are clearly discernable, except the framework combining L1 with FT basis (L1-FT). Among the B-mode images reconstructed by L1 (Figure 5.3(a)), both L1-DCT and L1-WA show comparable image quality and similar MAE values of 0.082. L1-FT produces the lowest image quality with the highest MAE value (0.242). Hyper- and hypoechoic inclusions on L1-FT image are blurred and dispersed, which make them difficult to discern. On the other hand, B-mode images reconstructed by BSBL present better image quality and lower MAE than those by L1, as shown in Figure 5.3(b). BSBL-DCT produces the lowest MAE of 0.022, while the MAEs of BSBL-FT and BSBL-WA are slightly higher at 0.029 and 0.037, respectively.

B-mode images of the elastography phantom containing a stiff inclusion from various CS frameworks are shown in Figure 5.4. Since the standard deviation of the scatterers' amplitude distribution is the same as that of background, the inclusion is not visible on the B-mode images. Among the B-mode images reconstructed by L1 (Figure 5.4(a)), both L1-DCT and L1-WA are associated with the same level of MAE at 0.066, whereas L1-FT yields the highest MAE of 0.111 with unexpected vertical black patterns appearing on the reconstructed image. Meanwhile, B-mode images reconstructed by the BSBL (Figure 5.4(b)) preserve the patterns intact with excellent accordance with the original image. Comparing MAE values associated with the same model bases, BSBL-based frameworks yield much lower values than L1-based ones. Among the BSBL images in Figure 5.4(b),

BSBL-FT is associated with the lowest MAE of 0.017, followed by BSBL-DCT and BSBL-WA with the MAE of 0.022 and 0.034, respectively.

Plots of MAE values for various CS frameworks are presented in Figure 5.5 as a function of removed data (subsampling rate) from 10% to 80%. Quite consistently, the errors increase with the number of samples removed, for all CS frameworks. For the echoic phantom (Figure 5.5(a)), the MAE values increase linearly until 50% subsampling for all model bases, and then rapidly rise, except for L1-FT, which shows a linear trend with much higher error than the other two bases. It is also notable that BSBL-based frameworks yield lower MAE values than L1-based ones with little variation between model bases, which is consistent with the trends in B-mode images (Figure 5.3 and 5.4). The MAE plots for L1-DCT and L1-WA are almost equivalent, while all BSBL-based plots agree well with each other. In case of the elastography phantom (Figure 5.5(b)), the trends of MAE are similar to those of the echoic phantom, apart from L1-FT which is still higher than the others, but follows much closer trend than that in echoic phantom. Overall MAE values associated with BSBL-based frameworks are lower than those of L1-based ones with little variation across model bases.

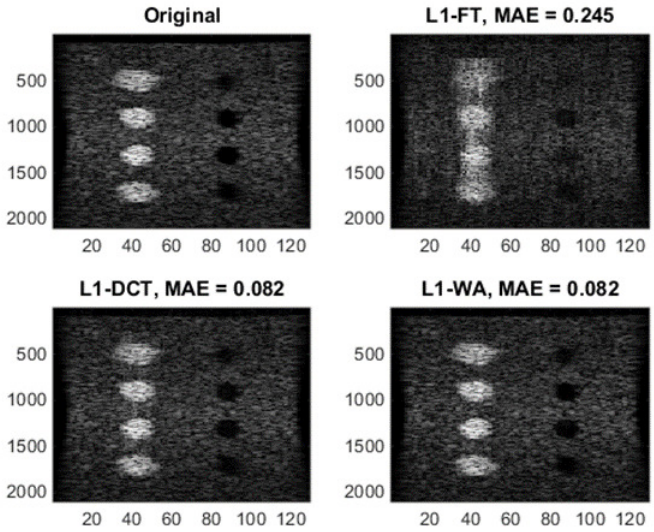

(a)

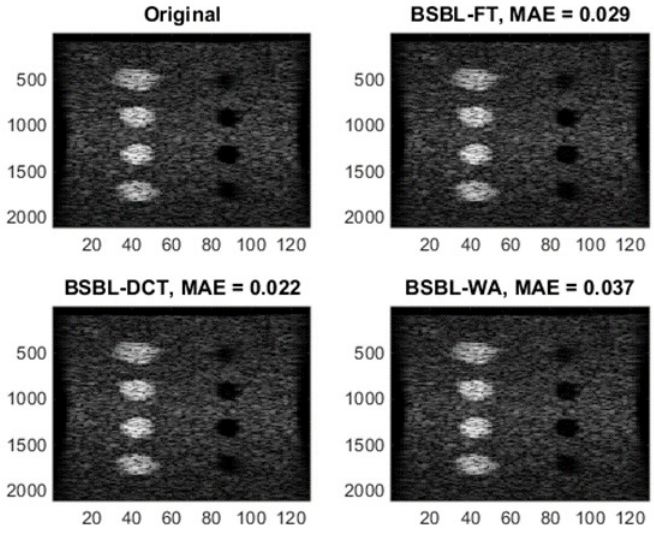

(b)

Figure 5.3: B-mode images of the echoic phantom containing hyper- and hypo- echoic inclusions produced from the original data and the reconstructed data by (a) L1-based and (b) BSBL-based CS reconstruction frameworks, combined with FT, DCT, and WA model bases, respectively. Data were reconstructed using 50% subsampling.

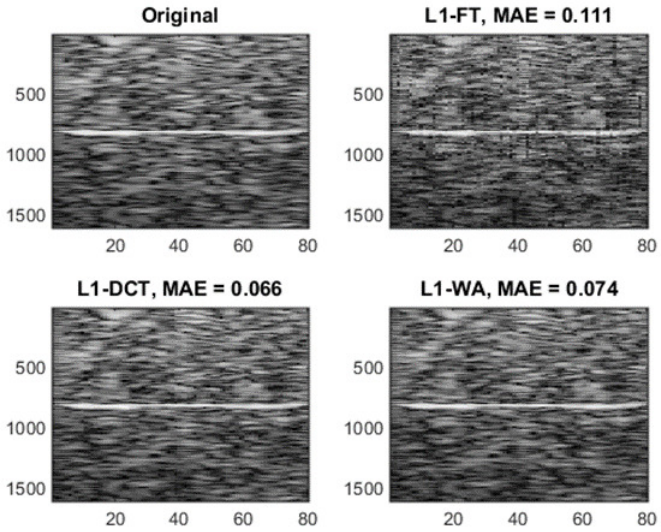

(a)

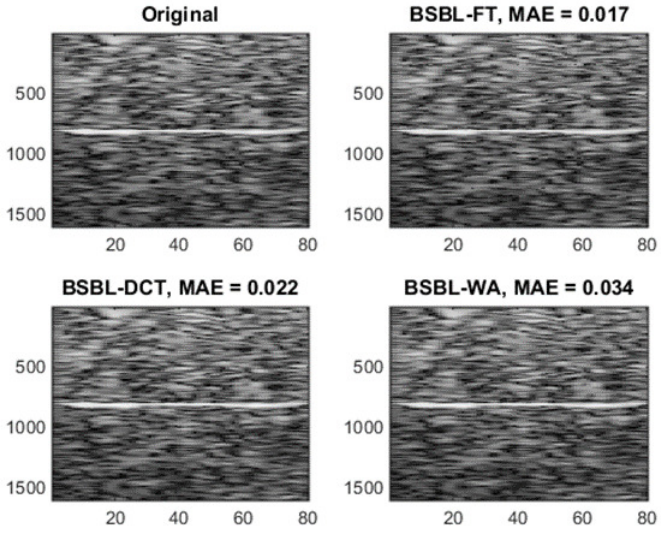

(b)

Figure 5.4: B-mode images of the elastography phantom produced from the original data and the reconstructed data by (a) the L1-based and (b) the BSBL-based based CS reconstruction frameworks, combined with FT, DCT, and WA model bases, respectively. Data were reconstructed using 50% subsampling.

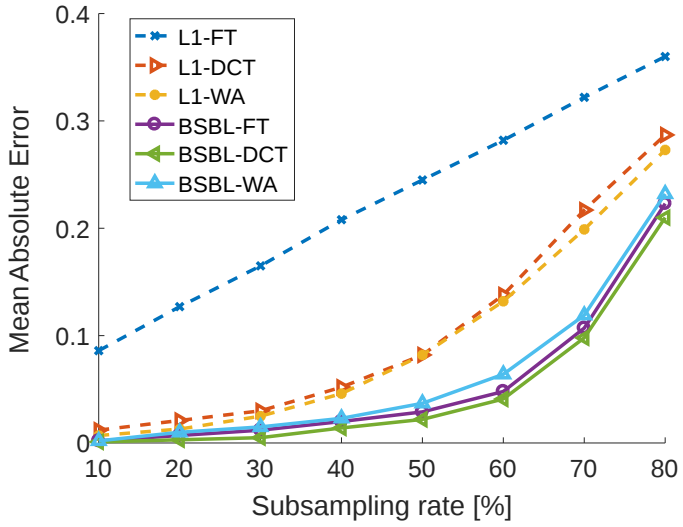

(a)

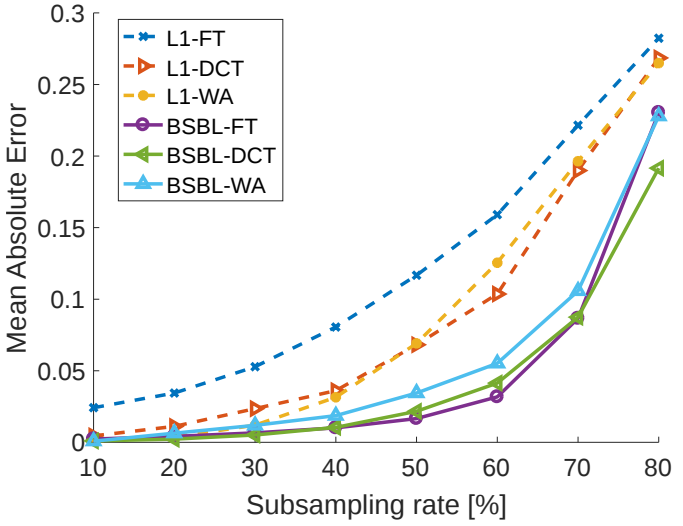

(b)

Figure 5.5: MAE plots associated with various CS frameworks as functions of subsampling rate, measured on: (a) the echoic phantom, (b) the elastography phantom.

5.4.2 Evaluation of Elastographic Phantom

By applying the RPSE method to the RF data of elastography phantom from CS reconstruction, elastograms are generated to describe the strain fields under compressive deformation. Image quality of the elastograms from various CS frameworks are comparatively investigated.

The elastograms from L1-based frameworks for the subsampling rate from 30% to 50% are compared in Figure 5.6. The elastograms for all bases for 30% subsampling rate preserve the original patterns very well, and the stiff inclusion in the center is clearly discernable. At 40% subsampling rate (Figure 5.6(b)), both L1-DCT and L1-WA elastograms still show discernable inclusion and consistent matrix strain which are close to the original image, while degradations in the inclusion and the matrix start occurring in L1-FT elastogram. When the subsampling rate is increased to 50% (Figure 5.6(c)) the shapes of the stiff inclusion for all three bases are hardly discernable and the strain fields in the matrix show inconsistent and locally varying behavior. Over all, L1-DCT and L1-WA preserve the strain patterns of similar quality until 40%, while L1-FT tends to lose the patterns much earlier than the others. From the observation, 40% subsampling rate seems to be the threshold compression ratio to effectively detect the inclusion for the elastograms from L1-based CS frameworks.

Strain values measured along the vertical centerline across the L1-based elastograms are plotted in Figure 5.7. The strain fields for three bases over the subsampling rate from 30% to 50% are compared with the strains from the FEA as a ground truth. At 30% subsampling rate (Figure 5.7(a)), both plots from L1-DCT and L1-WA show good agreement with the FEA strains. For 40% (Figure 5.7(b)), L1-DCT and L1-WA still follow the trend of FEA, but the strains start oscillating both in the inclusion and the matrix where strains are regarded as constant. The oscillations in these regions are significantly amplified with further increase of subsampling rate (Figure 5.7(c)). Beyond 50%, the strain plots become too noisy to identify the shape of the inclusion, which also indicates that sampling rate around 40% should be the threshold for L1-based CS frameworks.

The elastograms from BSBL-based CS frameworks over the subsampling rate from 50% to 70% are presented in Figure 5.8. At 50% subsampling rate (Figure 5.8(a)), all

elastograms preserve the patterns superbly; they are almost equivalent to the original elastogram and accurately depict strain distribution in the inclusion and the matrix. At 60%, the inclusion is still discernable, regardless of slight strain degradation particularly in BSBL-WA (Figure 5.8(b)). Beyond 70% subsampling rate, all elastograms are significantly degraded and the original strain patterns are lost almost completely as shown in Figure 5.8(c). Qualitative observation suggests that BSBL-DCT elastograms best agree with the original ones, particularly for 50% and 60% subsampling rate.

The strain plots along the vertical centerline across the BSBL-based elastograms are presented in Figure 5.9. The strain plots for all three bases show excellent agreement with the ground truth (FEA results) for 50% subsampling rate (Figure 5.9(a)). With the increase of subsampling rate, reconstructed strain plots start to show oscillating behavior (Figure 5.9(b)). Eventually, all strain plots lose the track of the ground truth beyond 70% subsampling rate, as shown in Figure 5.9(c). It can be summarized that that BLBL-based CS reconstruction is highly reliable until 50%, and produces the acceptable elastograms up to 60% subsampling rate, for all three bases tested. Furthermore, the qualities of elastograms from BSBL-based CS frameworks are far less influenced by the model bases than those from L1-based ones.

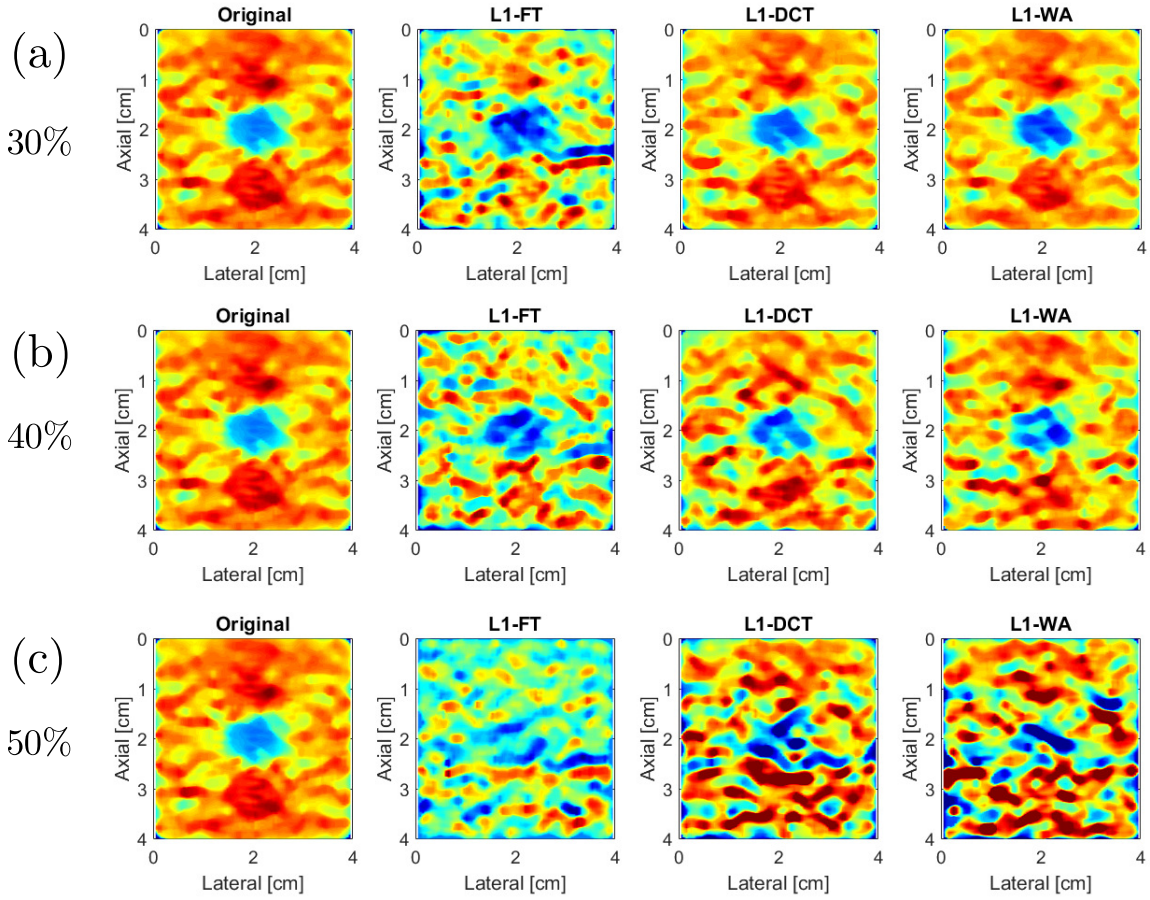

Figure 5.6: Elastograms of elastography phantom computed from the original data and from various CS reconstruction frameworks for the subsampling rate of: (a) 30%, (b) 40%, and (c) 50%.

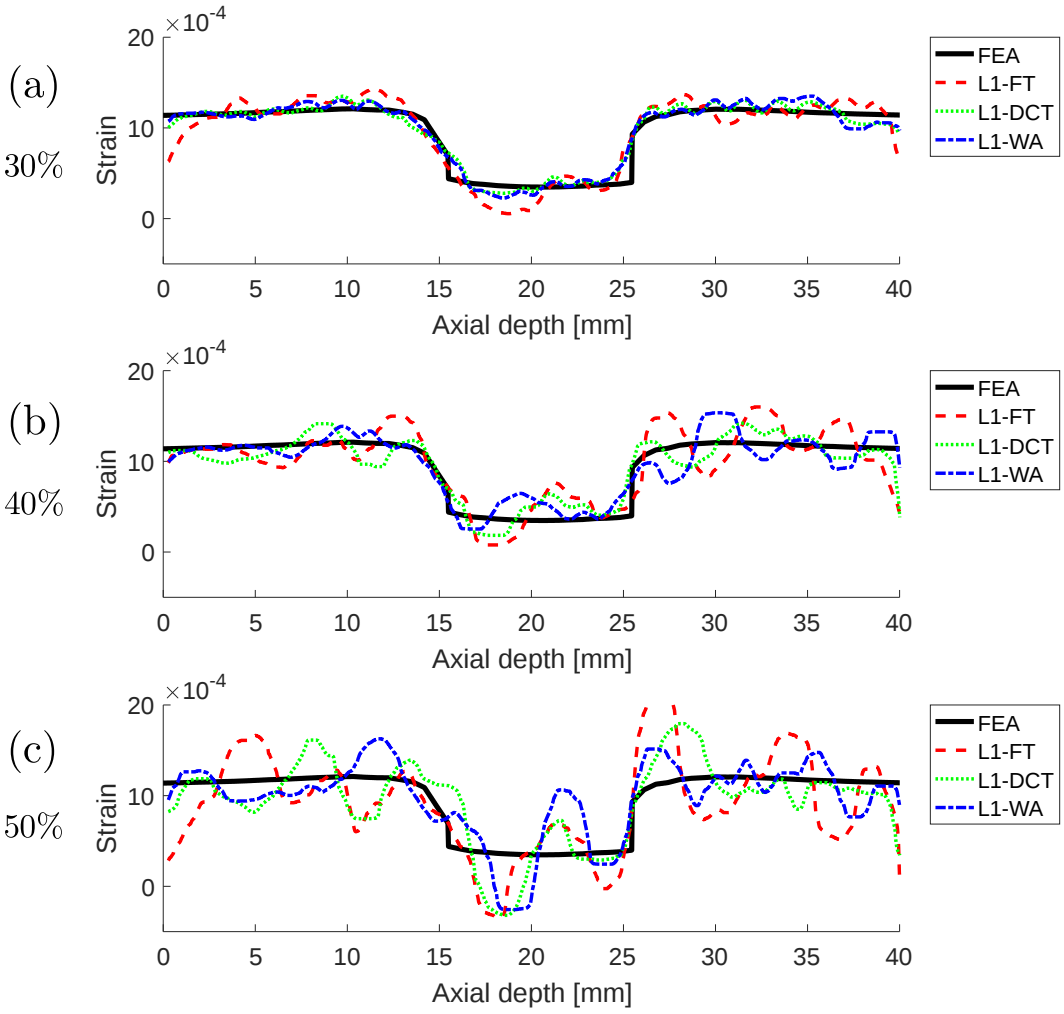

Figure 5.7: Strain values measured along the vertical centerline across the elastograms computed from the L1-based CS reconstruction frameworks for the subsampling rate of: (a) 30%, (b) 40%, (c) 50%. The FEA plots are the ground truth.

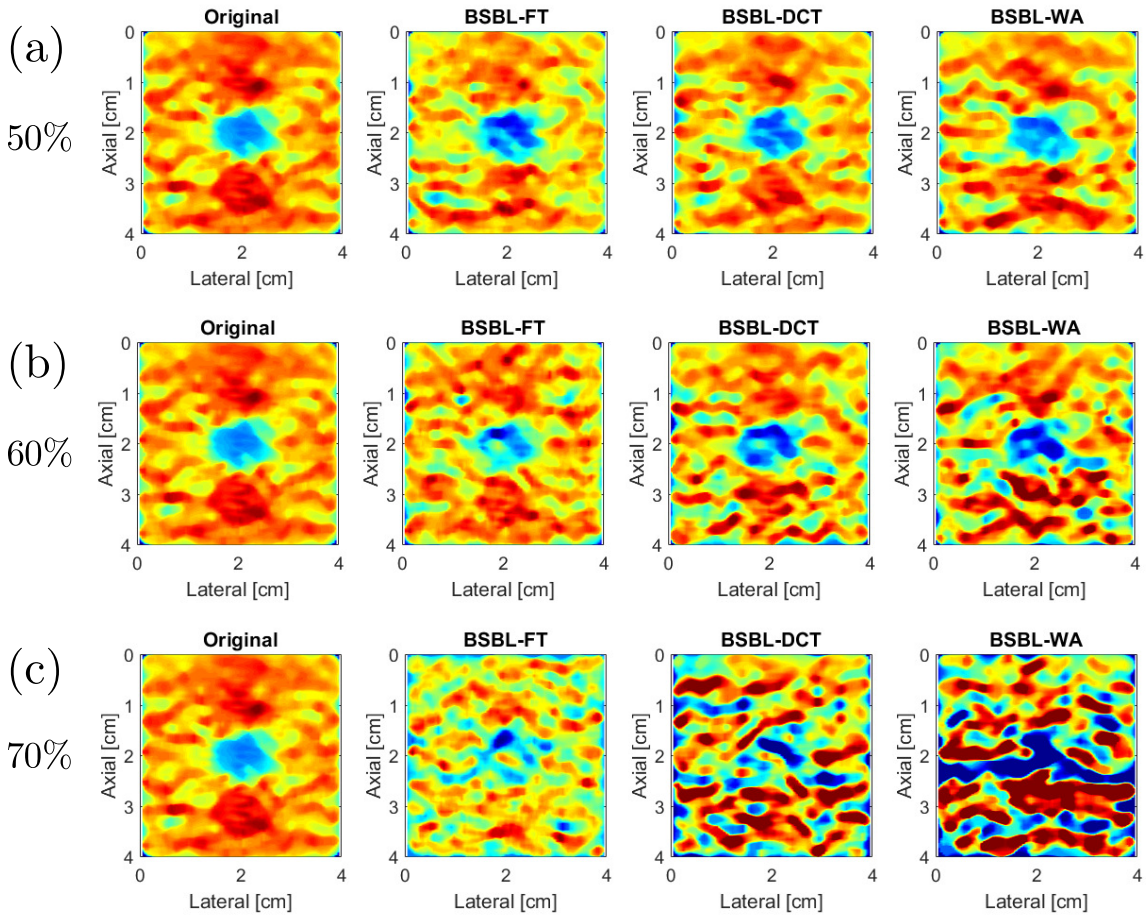

Figure 5.8: Elastograms of the elastography phantom computed from the original data and from the BSBL-based CS reconstruction frameworks for the subsampling rate of: (a) 30%, (b) 40%, and (c) 50%.

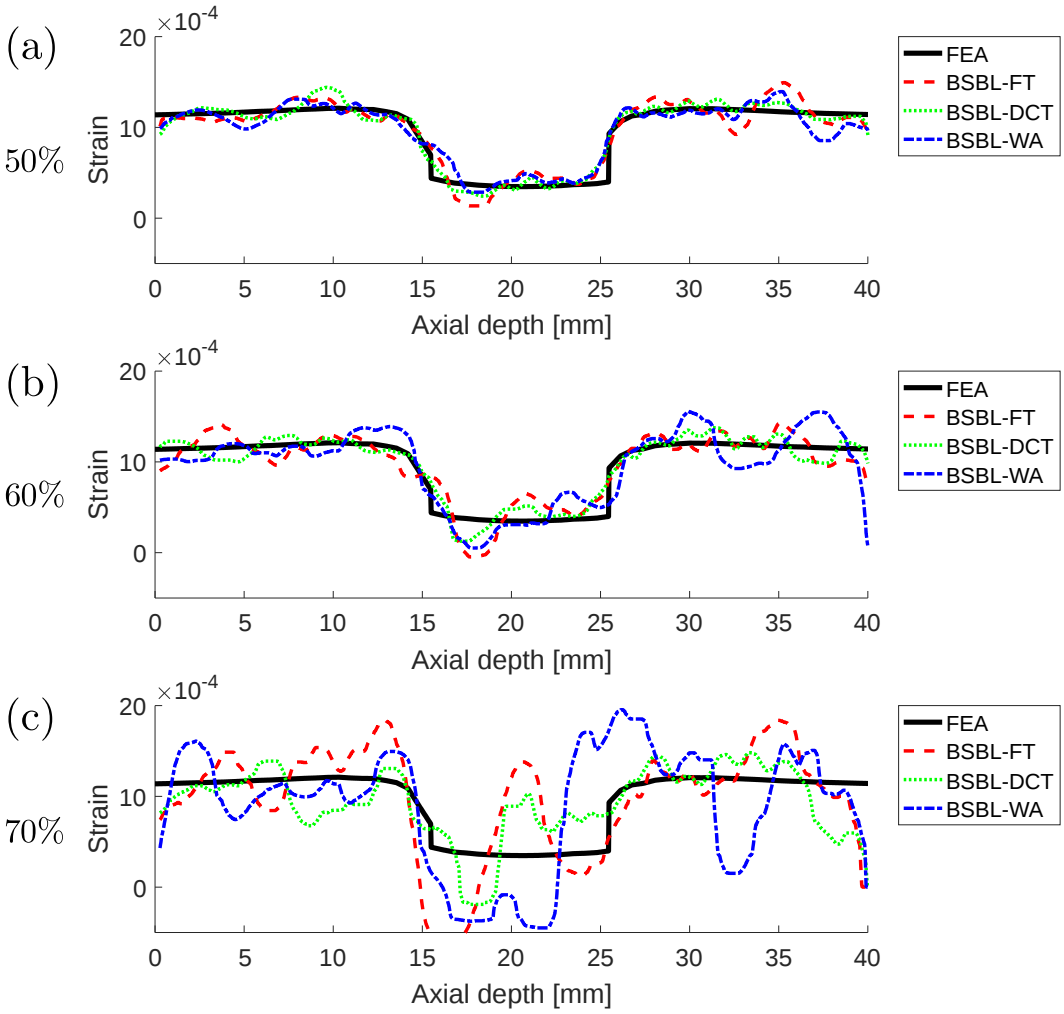

Figure 5.9: Strain values measured along the vertical centerline across the elastograms computed from the BSBL-based CS reconstruction frameworks for the subsampling rate of: (a) 50%, (b) 60%, (c) 70%.

5.4.3 Evaluation of Image Quality Measures

Image qualities of the elastograms are evaluated with three image quality measures (MAE, SNRe, and CNRe) to determine the optimal CS scheme for generating the ultrasound elastograms. All the image measures are collected over the subsampling rate from 10% to 80%.

The MAE plots of elastograms (Figure 5.10) from various CS frameworks are compared with the reference strain error (black solid line) that corresponds to 15% of the applied strain (0.1%). The reference error plays as the error criterion based on the observation that MAE plots rise rapidly once they reach this level. Since MAE can be regarded as a monotonic function of subsampling rate, the threshold subsampling rate of each framework is estimated from the intersection between the MAE and the error criterion.

Among the MAE plots for L1-based frameworks (dashed lines in Figure 5.10), the L1-FT yields the highest error level and intersects the error criterion at around 33% subsampling rate, while L1-DCT and L1-WA are slowly increasing until 40% subsampling rate from which they start rising rapidly. Overall, among L1-based frameworks, L1-WA presents the best result until it reaches the error criterion.

All BSBL-based CS frameworks generate similar level of MAE lower than error criterion until 50%, regardless of associated model bases. Threshold subsampling rate is identified to be around 60% for BSBL-WA and BSBL-FT and around 63% for BSBL-DCT. The comparison between L1- and BSLB-based plots in Figure 5.10 suggest that BSBL-based CS frameworks yield more reliable results than L1-based ones. Particularly BSBL-DCT yields the lowest error level over the subsampling range tested.

The elastographic SNRe and CNRe identifying the precision and the discernibility of the elastograms are quantified in Figure 5.11. All SNRe plots in Figure 5.11(a) present slowly decreasing trend at first, but start to drop rapidly with increase of subsampling rate. BSBL-based frameworks yield higher SNRe than L1-based ones across all subsampling range tested. In Figure 5.11(b), CNRe plots from CS frameworks are almost equivalent to those from original elastogram (meaning excellent discernibility) in low subsampling range; however, they start to drop rapidly with increase of subsampling rate. Over all, both SNRe

and CNRe plots from BSBL-based frameworks present higher values than those from L1-based ones over the entire subsampling range. Furthermore, results from BSBL-based frameworks are less influenced by the model bases because its block-wise approach might maximize the signal sparsity of ultrasound echo signal. All the image quality measures (MAE, SNRe, and CNRe) imply that the feasible level of the subsampling rate without significant loss of patterns is 40% for L1-based and 60% for BSBL-based frameworks, respectively.

Computation times of the CS reconstruction methods were also measured on a Windows 10 computer (2.3MHz, i7-3670 CPU with 12 GB RAM, ASUS-K55VD) using the in-house developed MATLAB code. Overall, L1-WA showed the fastest computation time (16.732 seconds) while L1-FT spent 105.909 seconds due to the calculation of its complex array. On the other hand, BSBL-based frameworks presented relatively similar computation times among different bases. BSBL-WA took only 38.454 seconds, while BSBL-DCT and BSBL-FT recorded 41.864 and 55.479 seconds, respectively. As for the number of average iterations, L1-FT recorded 42.61, while L1-DCT and L1-WA took 12.95 and 12.73 iterations, respectively. For the BSBL-based frameworks, all methods required around 7 iterations. Threshold subsampling rates and the corresponding MAEs, SNRe, CNRe, and computation times for different CS frameworks are summarized in Table 5.2.

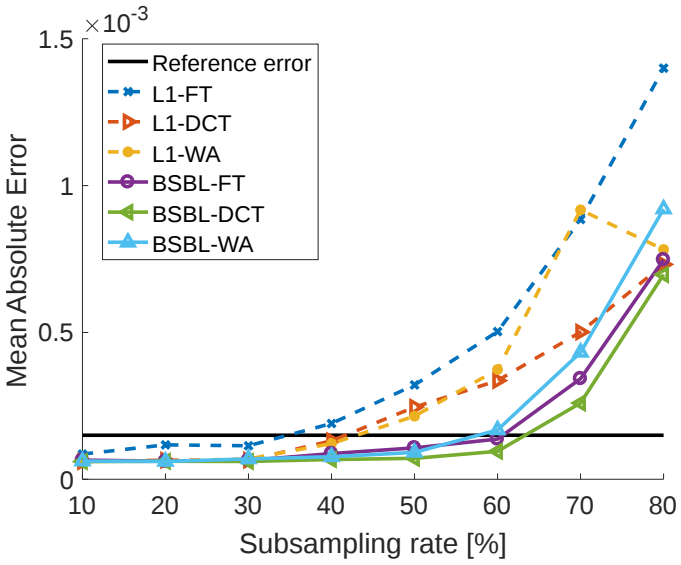

Figure 5.10: MAE of the elastograms as a function of subsampling rate. The error is computed on the elastograms produced from the various CS reconstruction frameworks. Reference error is 15% of the applied strain.

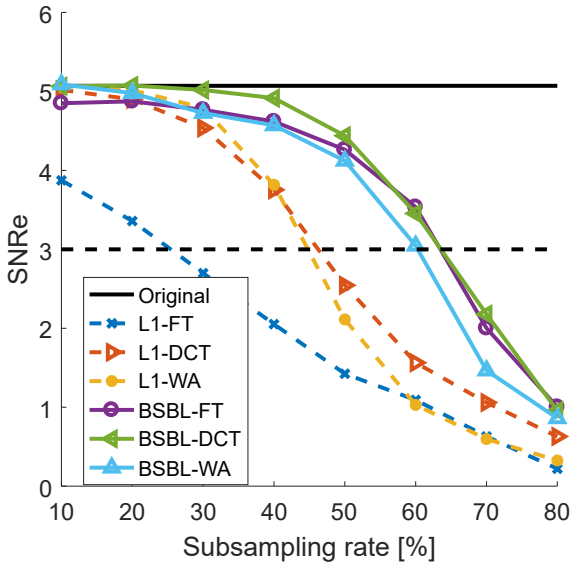

(a)

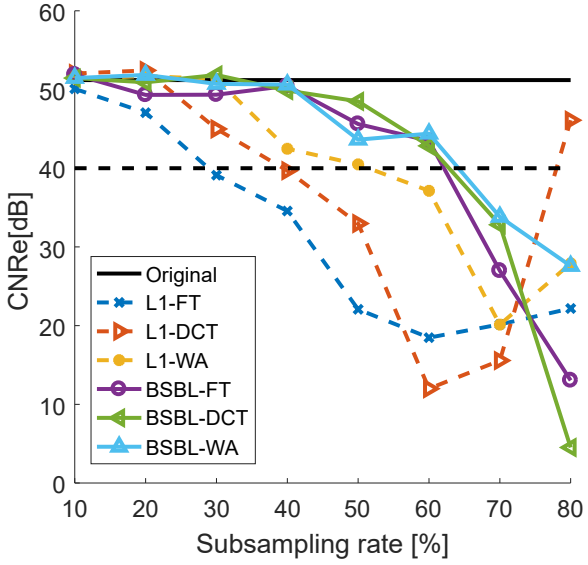

(b)

Figure 5.11: (a) SNRe and (b) CNRe of the elastograms as a function of subsampling rate. The image quality measures are computed on the elastograms produced from the original data and from various CS reconstruction frameworks.

Table 5.2: Image quality measures (MAE, SNRe, CNRe), CPU time, and average number of iteration at the threshold subsampling rate (SR) associated with various CS reconstruction frameworks.

CS Reconstruction	CS model basis	Threshold SR(%)	MAE	SNRe	CNRe (dB)	CPU (sec)	Avg. iteration
L1	FT	40	1.899e-4	2.052	34.564	105.91	42.61
L1	DCT	40	1.312e-4	3.754	39.694	28.492	12.95
L1	WA	40	1.216e-4	3.817	42.474	16.731	12.73
BSBL	FT	60	1.369e-4	3.534	43.489	55.479	7
BSBL	DCT	60	9.538e-5	3.455	42.839	41.864	7
BSBL	WA	60	1.681e-4	3.045	44.391	38.454	7

5.5 Conclusion

Large amount of ultrasound echo data to be transferred through wireless communication is one of the major limitations in implementing ultrasound elastography function on portable ultrasound. As a means to reduce the size of the measurement data, this thesis addresses the feasibility of applying compressive sensing (CS) method to elastography. Since CS reconstruction performance is highly affected by the model basis representing the sparse expansion of the data, as well as reconstruction algorithm to solve the minimization problem, three bases, discrete Fourier transform (FT), discrete cosine transform (DCT), and the recently introduced wave atoms (WA), and two reconstruction algorithms, L1 minimization (L1) and Block sparse Bayesian learning (BSBL) were tested to find the most feasible CS framework.

The quality of the reconstructions was quantified using the B-mode and elastogram images of simulated numerical phantoms through three image quality measures, mean absolute error (MAE), signal-to-noise ratio (SNRe) and contrast-to-noise ratio (CNRe) at varying subsampling rates. The results indicate that BSBL-based CS frameworks generally delivered the superior performance to L1-based ones. Particularly, the CS framework adopting BSBL-DCT combination yielded the lowest MAE and the highest SNRe and CNRe among all combinations, and achieved the optimal CS reconstruction framework for producing elastograms in the portable ultrasound device. The results also suggest that the maximum data reduction (subsampling) rate for generating discernible elastograms is 60% for BSBL-DCT framework.

Chapter 6

Summary of Contributions and Future Work

6.1 Summary of Contributions

The limitations of computational performance and data transfer speed via wireless communication are two major obstacles to realizing the elastography functionality in wireless portable ultrasound device. In this work, two research approaches seeking for the feasible solutions for realizing the elastography functionality in the portable ultrasound device have been performed to overcome the obstacles.

A new robust phase-based strain estimator (RPSE), which is computationally efficient and robust to the variations of ultrasound measurement parameters, has been proposed as an optimum strain estimator which is suitable for the portable ultrasound with limited computational performance. The image quality and computational efficiency of RPSE have been evaluated by performing the comparative study with other representative strain estimators. The results suggest that the RPSE can produce comparable and/or superior level of elastography to other strain estimators, as described in Chapter 3. Since the ultrasound measurement parameters including speed of sound, sampling intervals along depth and frame slightly vary during the ultrasound RF signal acquisition and affect the

accuracy of elastography, the robustness of the RPSE to the measurement parameters is particularly beneficial to the implementation of the elastography function in the portable device.

As a solution to reduce the size of ultrasound echo data transferred via wireless communication, the feasibility of applying compressive sensing (CS) method to elastography has been considered. This thesis has proposed and tested various CS frameworks consisting of three different model bases and two kinds of reconstruction algorithms. In terms of three image quality measures (MAE, SNRe, and CNRe), CS reconstruction performances of both B-mode and elastogram images have been evaluated as described in Chapter 5. Evaluation results have showed that BSBL-based CS frameworks generally deliver the better image quality and higher subsampling rate compared to L1-based ones. Particularly, the CS framework adopting BSBL-DCT combination has showed the best CS performance among all tested combinations. The results also have suggested that the maximum data reduction (subsampling) rates which can reasonably preserve the strain value are 40% for L1-based framework and 60 % for BSBL-based framework, respectively.

It can be concluded that the RPSE algorithm can substantially reduce the computation load and time and should be the best fit for portable ultrasound elastography, while CS method adopting BSBL-DCT framework can minimize the data transfer load and of great help to achieve real-time portable ultrasound elastography.

6.2 Future Work

6.2.1 RPSE with an Advanced Phase Unwrapping Method

Although RPSE uses phase unwrapping function in MATLAB, it still has the limited displacement range between the frames, corresponding to a half ultrasound wavelength; thus, it may not be an optimum strain estimator for fast-moving tissues. In addition, most phase-based strain estimators are suffering from line errors called dropout because the phase shift estimation of current point relies on the accuracy of the previous point's estimation. Consequently, an entire line on strain map can be easily corrupted by an error at the previous

point in the line. As described in the Section 2.2.3, several studies [46, 96] have been introduced to expand the displacement range and remove the line errors. By developing or adopting more advanced and accurate advance phase unwrapping method, RPSE can further improve its accuracy and displacement bandwidth without much computational overhead.

6.2.2 Real-time CS Framework

Currently the computation for CS reconstruction is so heavy that real-time processing is difficult to be achieved. Improving the algorithm for efficient and fast computation is essential for the application of CS to portable ultrasound. CS real-time implementation may be achieved by using a better computation framework such as a GPU's parallel computing methods or a C++ code implementation. Another important improvement involves investigating other reconstruction algorithms and model bases, specifically adapted to ultrasound RF data. Such improvement would make it possible to build an even sparser representation than current BSBL-DCT combination, thus allows better reconstruction for a given subsampling rate.

APPENDICES

Appendix A

Mathematical Operations

A.1 Correlation and Convolution

Correlation and convolution are basic operations to extract information from two functions or signals. The correlation of continuous functions f and g is defined by

$$f \circ g(x) = \int_{-\infty}^{\infty} f(p)g(x+p)dp, \tag{A.1}$$

whereas the convolution is defined by

$$f * g(x) = \int_{-\infty}^{\infty} f(p)g(x-p)dp. \tag{A.2}$$

For discrete data sets, correlation is the process of moving a filter mask over the data set and computing the sum of products at each location. The mechanics of convolution are the same, except that the filter is first rotated by 180°. For the data set g of size $M \times N$, correlation with a filter f of size $m \times n$ is given by

$$h(x,y) = f \circ g = \sum_{s=-\frac{m-1}{2}}^{\frac{m-1}{2}} \sum_{t=-\frac{n-1}{2}}^{\frac{n-1}{2}} f(s,t)g(x+s,y+t), \tag{A.3}$$

where x and y varied so that in f visits every point in g.

Correlation is useful in comparing two deterministic signals and it provides a measure of similarity between the first signal and a time-delayed version of the second signal (or the first signal). Figure A.1 illustrates the correlation using a 3×3 filter. At any point (x, y) in the data set, the correlation, $h(x, y)$, of the filter is the sum of the products of the filter and the data set encompassed by the filter. The location where maximum correlation value is produced is where the highest similarity occurs.

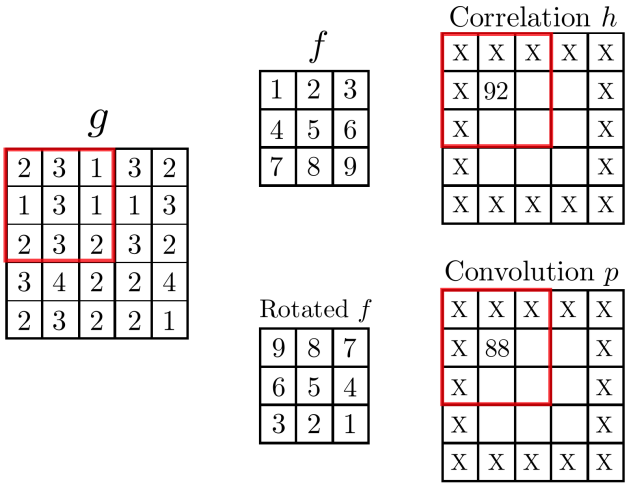

$$h(2,2) = 2\times1+3\times2+1\times3+1\times4+3\times5+1\times6+2\times7+3\times8+2\times9 = 92$$
$$p(2,2) = 2\times9+3\times8+1\times7+1\times6+3\times5+1\times4+2\times3+3\times2+2\times1 = 88$$

Figure A.1: Calculation mechanism of correlation and convolution

In a same manner, the convolution of f and g is given by

$$p(x, y) = f * g = \sum_{s=-\frac{m-1}{2}}^{\frac{m-1}{2}} \sum_{t=-\frac{n-1}{2}}^{\frac{n-1}{2}} f(s, t)g(x - s, y - t), \tag{A.4}$$

where the minus signs of the right flip g (i.e. rotate it by 180). Flipping and shifting f instead of g produces the same result, as shown in Figure A.1. As with correlation, this is evaluated for all values of x and y so that every element of f visits every point in g.

A.2 Autocorrelation

Autocorrelation is the cross-correlation of a signal with itself at different points in time. Autocorrelation describes the similarity of coherence between the given function or the signal and its delayed or its advanced version. The autocorrelation function of an aperiodic signal $x(t)$ is defined by [97]

$$\gamma(\tau) = \int_{-\infty}^{\infty} x(t)x(t+\tau)dt = \int_{-\infty}^{\infty} x(t)x(t-\tau)dt = x(t) * x(t-\tau). \tag{A.5}$$

For a complex signal $x(t)$, the autocorrelation is defined by [98]

$$\gamma(\tau) = \int_{-\infty}^{\infty} x(t)x^*(t+\tau)dt = \int_{-\infty}^{\infty} x(t)x^*(t-\tau)dt, \tag{A.6}$$

where x^* denotes the complex conjugate. If $\{x(t)\}_{t=0}^{N-1}$ is a periodic signal, the autocorrelation can be written as

$$\gamma(\tau) = \sum_{t=0}^{N-1} x(t)x^*(t+\tau). \tag{A.7}$$

For a periodic array $x(m,n)$ with $0 \leq m \leq M-1$ and $0 \leq n \leq N-1$, the autocorrelation is the $M \times N$ matrix given by

$$\gamma(\tau_x, \tau_y) = \sum_{m=0}^{M-1} \sum_{n=0}^{N-1} x(m,n)x^*(m+\tau_x, n+\tau_y). \tag{A.8}$$

In this thesis, ultrasound radio-frequency (RF) data acquired from the ultrasound probe is assumed a two dimensional matrix with M depth samples and N adjacent lateral scan lines in a time-series with K "slow time" frames. Each ultrasound data set can be represented by the cordinates $[m, n, k]$ in time-space. Following the notation of Loupas. et al [57], M and K specify the "range gate length", the number of depth samples, and the "ensemble length", the number of pulse transmissions, respectively. In the same manner, the term lateral gate length will be defined as N.

The RF data from the set of 2D frames are represented as a real, discrete three dimensional signal, and it will be expressed $x[m, n, k]$, where m, n, k are the depth index, the beam

number and the frame number of a single data set. A set of K matrices $X_0, X_1, \cdots, X_{K-1}$ with M rows and N columns is represented as X_{frame} given by [42]:

$$X_0 = \begin{bmatrix} x[0,0,0] & x[0,1,0] & \cdots & x[0,N-1,0] \\ x[1,0,0] & x[1,1,0] & \cdots & x[1,N-1,0] \\ \vdots & \vdots & \ddots & \vdots \\ x[M-1,0,0] & x[M-1,1,0] & \cdots & x[M-1,N-1,0] \end{bmatrix}$$

$$\vdots \tag{A.9}$$

$$X_{K-1} = \begin{bmatrix} x[0,0,K-1] & x[0,1,K-1] & \cdots & x[0,N-1,K-1] \\ x[1,0,K-1] & x[1,1,K-1] & \cdots & x[1,N-1,K-1] \\ \vdots & \vdots & \ddots & \vdots \\ x[M-1,0,K-1] & x[M-1,1,K-1] & \cdots & x[M-1,N-1,K-1] \end{bmatrix}$$

The autocorrelation function between the pre- and post-frame of ultrasound RF data is defined as [42]:

$$\gamma(m,k) = \sum_{u=0}^{M-m-1} \sum_{v=0}^{N-1} \sum_{w=0}^{K-k-1} x_+[u,v,w] x_+^*[u+m, v, w+k], \tag{A.10}$$

where x_+ is the analytical signal along the axial dimension which is a complex-valued function that has no negative frequency components, and defined as:

$$x_+[m,n,k] = x[m,n,k] + j \cdot \mathbf{H}\{x[m,n,k]\}, \tag{A.11}$$

where $\mathbf{H}\{x[m,n,k]\}$ is the Hilbert transform.

Appendix B

Displacement Estimation Techniques

B.1 Correspondence Functions for 1D Displacement Estimation

Signal correspondence functions can be used to determine the time delay (or shift) between a given pair of the ultrasonic data. Afterward the time delay estimate can be converted to the displacement occurred while capturing ultrasonic data. In this section, the most common signal correspondence functions for estimating 1D displacement from the time delay between two 1D RF signals is briefly discussed.

Normalized Cross Correlation

A normalized cross correlation (NCC) between a pair of windowed time-segments is utilized for calculating time delays following compression. Given a pair of pre- and post-compression signals (s_1 and s_2), the normalized cross correlation is defined as [28]:

$$NCC_{12}(\tau) = \frac{\sum_{i=-T/2}^{T/2} s_1(i)s_2(i+\tau)}{\sqrt{\sum_{i=-T/2}^{T/2} s_1^2(i) \sum_{i=-T/2}^{T/2} s_2^2(i+\tau)}}, \tag{B.1}$$

where T represents the kernel window length. NCC includes the energy of both signal pairs in its mathematical formulation. Therefore, NCC compensates for local variations in the mean and standard deviation of the signals [99]. As a result, NCC can produce robust and accurate delay estimates. However, high computational cost of this algorithm is a significant drawback for implementing real-time estimator.

Sum Absolute Difference

Sum of absolute differences (SAD) is one of the simplest similarity measures which is computed by subtracting signals, aggregating the absolute differences within the kernel window, and optimizing the summed value by the winner-take-all (WTA) strategy. If the reference and the delayed signals exactly match, the resultant will be zero. Time delay estimate is obtained using the value for which the SAD is a minimum. SAD for a given pair of pre- and post-compression signals (s_1 and s_2) is defined as [25]:

$$SAD_{12}(\tau) = \sum_{i=-T/2}^{T/2} |s_1(i) - s_2(i+\tau)|. \tag{B.2}$$

Sum Squared Differences

In sum of squared differences (SSD), the differences between a given pair of signals are squared and summed within a kernel window. Afterward, like SAD the sum of squared differences is optimized by WTA strategy. SSD based estimator has a higher computational complexity compared to SAD based estimator due to numerous multiplication operations involved. SSD for given a pair of pre- and post-compression signals (s_1 and s_2) is defined as [28]:

$$SSD_{12}(\tau) = \sum_{i=-T/2}^{T/2} (s_1(i) - s_2(i+\tau))^2. \tag{B.3}$$

Since both SAD and SSD based time delay estimators do not compensate for local variations in the mean and variance of the signals, these estimators typically result in lower SNR than cross-correlation based time delay estimation.

FFT-based Correlation

Signal correspondence can be also estimated by calculating an analytical correlation function in the frequency domain. Fast Fourier Transform (FFT)-based correlation estimates a phase and a group delay. The phase and group delays are summed algebraically to yield a continuous time delay estimate. Periodic discrete cross-correlation for a periodic signal with a period of N_p samples is defined as:

$$sc_{12}(n) = \sum_{k=1}^{N_p} s_1(k)s_2(k+n), \tag{B.4}$$

where s_1 and s_2 are pre- and post-compression signals in discrete-time domain, respectively, and n is the lag between the signals. Using the FFT, circular convolution can be carried out more efficiently, especially for large N_p [100]:

$$SC_{12}(n) = S_1(n)S_2(n), \tag{B.5}$$

where SC_{12}, S_1, and S_2 are the Discrete Fourier Transforms of sc_{12}, s_1 and s_2.

B.2 Fast Normalized Cross-Correlation for 2D

Signal correspondence between two 2D data can be estimated directly from 2D domain by applying digital image correlation method to a pair of ultrasound B-mode images. Digital image correlation method uses 2D normalized cross correlation (NCC) as a block matching algorithm.

Normalized cross correlation (NCC) yields a value of 1 when two data sets are exactly matched and a value close to 0 when no match is made. Mathematically, NCC with data shift τ is defined as:

$$NCC_{12}(\tau) = \frac{\sum_{i=0}^{N-1}(s_1(i) - \bar{s}_1)(s_2(i+\tau) - \bar{s}_2)}{\sqrt{\sum_{i=0}^{N-1}(s_1(i) - \bar{s}_1)^2 \sum_{i=0}^{N-1}(s_2(i+\tau) - \bar{s}_2)^2}}, \tag{B.6}$$

where $\bar{s_1}$ and $\bar{s_2}$ are the mean of s_1 and s_2, respectively.

Heavy computation load of NCC is always problematic. Fast normalized cross correlation (FNCC) adopting the sum table method in computation was proposed to relieve the heavy computation of NCC [37]. In FNCC, sum table is the pre-calculated look-up table over the whole region of function s_2, and is refered to whenever a local sum is calculated. Looking into the numerator and the second half of the denominator of Eq. (B.6), respectively, we have,

$$\sum_{i=0}^{N-1}(s_1(i)-\bar{s}_1)(s_2(i+\tau)-\bar{s}_2)=\sum_{i=0}^{N-1}s_1(i)s_2(i+\tau)-\bar{s}_1\sum_{i=0}^{N-1}s_2(i+\tau), \tag{B.7}$$

$$\sum_{i=0}^{N-1}(s_2(i+\tau)-\bar{s}_2)^2=\sum_{i=0}^{N-1}s_2(i+\tau)^2-\frac{1}{N}\left(\sum_{i=0}^{N-1}s_2(i+\tau)\right)^2. \tag{B.8}$$

Local sum of s_2 and s_2^2 for each n can be computed by using the sum table which is pre-calculated look-up table and is referred to each moment local sum is calculated. Comparing to NCC which calculates local sum for every n, FNCC can save huge computational resource and time.

The concepts of FNCC can be expanded to 2D function. B-mode images and data frames from RF signals are usually expressed positive 2D matrix. Applying the above algorithms one can track points of interest by searching the optimal cross-correlation value effectively while sliding latter images over the previous image with high efficiency.

References

[1] Thomas A Krouskop, Thomas M Wheeler, Faouzi Kallel, Brian S Garra, and Timothy Hall. Elastic moduli of breast and prostate tissues under compression. *Ultrasonic Imaging*, 20(4):260–274, 1998.

[2] Jonathan Ophir, Ignacio Cespedes, Hm Ponnekanti, Y Yazdi, and X Li. Elastography: a quantitative method for imaging the elasticity of biological tissues. *Ultrasonic Imaging*, 13(2):111–134, 1991.

[3] Jonathan Ophir, Seshadri Srinivasan, Raffaella Righetti, and Arun Thittai. Elastography: a decade of progress (2000-2010). *Current Medical Imaging Reviews*, 7(4):292–312, 2011.

[4] Yougun Han, Dong-Woo Kim, and Hyock-Ju Kwon. Application of digital image cross-correlation and smoothing function to the diagnosis of breast cancer. *Journal of the Mechanical Behavior of Biomedical Materials*, 14:7–18, 2012.

[5] Bonghun Shin, Darindra Gopaul, Samantha Fienberg, and Hyock Ju Kwon. Application of Eshelby's solution to elastography for diagnosis of breast cancer. *Ultrasonic Imaging*, 38(2):115–136, 2016.

[6] Ako Itoh, Ei Ueno, Eriko Tohno, Hiroshi Kamma, Hideto Takahashi, Tsuyoshi Shiina, Makoto Yamakawa, and Takeshi Matsumura. Breast disease: clinical application of us elastography for diagnosis 1. *Radiology*, 239(2):341–350, 2006.

[7] Anke Thomas, Friedrich Degenhardt, André Farrokh, Sebastian Wojcinski, Torsten Slowinski, and Thomas Fischer. Significant differentiation of focal breast lesions:

calculation of strain ratio in breast sonoelastography. *Academic Radiology*, 17(5):558–563, 2010.

[8] Hui Zhi, Xiao-Yun Xiao, Hai-Yun Yang, Bing Ou, Yan-Ling Wen, and Bao-Ming Luo. Ultrasonic elastography in breast cancer diagnosis: strain ratio vs 5-point scale. *Academic Radiology*, 17(10):1227–1233, 2010.

[9] Yin Mon Myint, Khin Wee Lai, Maheza Irna Mohamad Salim, Yan Chai Hum, and Nugraha Priya Utama. Ultrasonic elastography and breast imaging. In *Advances in Medical Diagnostic Technology*, pages 1–22. Springer, 2014.

[10] Andreas Lorenz, H-J Sommerfeld, Miguel Garcia-Schürmann, Stathis Philippou, Theodor Senge, and Helmut Ermert. A new system for the acquisition of ultrasonic multicompression strain images of the human prostate in vivo. *Ultrasonics, Ferroelectrics, and Frequency Control, IEEE Transactions on*, 46(5):1147–1154, 1999.

[11] Seyed Reza Mousavi, Iman Khalaji, Ali Sadeghi Naini, Kaamran Raahemifar, and Abbas Samani. Statistical finite element method for real-time tissue mechanics analysis. *Computer Methods in Biomechanics and Biomedical Engineering*, 15(6):595–608, 2012.

[12] Seyed Reza Mousavi, Ali Sadeghi-Naini, Gregory J Czarnota, and Abbas Samani. Towards clinical prostate ultrasound elastography using full inversion approach. *Medical Physics*, 41(3), 2014.

[13] Hassan Rivaz, Ioana Fleming, Lia Assumpcao, Gabor Fichtinger, Ulrike Hamper, Michael Choti, Gregory Hager, and Emad Boctor. Ablation monitoring with elastography: 2d in-vivo and 3d ex-vivo studies. In *Medical Image Computing and Computer-Assisted Intervention–MICCAI 2008*, pages 458–466. Springer, 2008.

[14] Laura A Chernak and Darryl G Thelen. Tendon motion and strain patterns evaluated with two-dimensional ultrasound elastography. *Journal of Biomechanics*, 45(15):2618–2623, 2012.

[15] Joline E Brandenburg, Sarah F Eby, Pengfei Song, Heng Zhao, Jeffrey S Brault, Shigao Chen, and Kai-Nan An. Ultrasound elastography: the new frontier in direct measurement of muscle stiffness. *Archives of Physical Medicine and Rehabilitation*, 95(11):2207–2219, 2014.

[16] Takayuki Muraki, Hiroaki Ishikawa, Shuhei Morise, Nobuyuki Yamamoto, Hirotaka Sano, Eiji Itoi, and Shin-ichi Izumi. Ultrasound elastography-based assessment of the elasticity of the supraspinatus muscle and tendon during muscle contraction. *Journal of Shoulder and Elbow Surgery*, 24(1):120–126, 2015.

[17] BP Nelson and A Sanghvi. Out of hospital point of care ultrasound: current use models and future directions. *European Journal of Trauma and Emergency Surgery*, pages 1–12, 2015.

[18] Juin-Jet Hwang, Jens Quistgaard, Jacques Souquet, Lawrence Crum, et al. Portable ultrasound device for battlefield trauma. In *Ultrasonics Symposium, 1998. Proceedings., 1998 IEEE*, volume 2, pages 1663–1667. IEEE, 1998.

[19] John Taylor, Kyle McLaughlin, Andrew McRae, Eddy Lang, and Andrew Anton. Use of prehospital ultrasound in north america: a survey of emergency medical services medical directors. *BMC Emergency Medicine*, 14(1):6, 2014.

[20] Travis C Russell and Paul F Crawford. Ultrasound in the austere environment: a review of the history, indications, and specifications. *Military Medicine*, 178(1):21–28, 2013.

[21] Brian Michael Lempriere. *Ultrasound and Elastic waves: Frequently asked Questions*. Academic Press, 2003.

[22] James A Zagzebski. *Essentials of ultrasound physics*. Mosby, 1996.

[23] David H Evans, Jørgen Arendt Jensen, and Michael Bachmann Nielsen. Ultrasonic colour doppler imaging. *Interface Focus*, 1(4):490–502, 2011.

[24] Reza Zahiri-Azar and Septimiu E Salcudean. Motion estimation in ultrasound images using time domain cross correlation with prior estimates. *Biomedical Engineering, IEEE Transactions on*, 53(10):1990–2000, 2006.

[25] Pawan Chaturvedi, Michael F Insana, and Timothy J Hall. 2-d companding for noise reduction in strain imaging. *Ultrasonics, Ferroelectrics, and Frequency Control, IEEE Transactions on*, 45(1):179–191, 1998.

[26] Fai Yeung, Stephen F Levinson, and Kevin J Parker. Multilevel and motion model-based ultrasonic speckle tracking algorithms. *Ultrasound in Medicine & Biology*, 24(3):427–441, 1998.

[27] I Céspedes, Y Huang, J Ophir, and S Spratt. Methods for estimation of subsample time delays of digitized echo signals. *Ultrasonic Imaging*, 17(2):142–171, 1995.

[28] Francesco Viola and William F Walker. A spline-based algorithm for continuous time-delay estimation using sampled data. *Ultrasonics, Ferroelectrics, and Frequency Control, IEEE Transactions on*, 52(1):80–93, 2005.

[29] S Srinivasan, J Ophir, and SK Alam. Elastographic imaging using staggered strain estimates. *Ultrasonic Imaging*, 24(4):229–245, 2002.

[30] Faouzi Kallel and Jonathan Ophir. A least-squares strain estimator for elastography. *Ultrasonic Imaging*, 19(3):195–208, 1997.

[31] S Kaisar Alam and Jonathan Ophir. Reduction of signal decorrelation from mechanical compression of tissues by temporal stretching: Applications to elastography. *Ultrasound in Medicine & Biology*, 23(1):95–105, 1997.

[32] T Varghese, J Ophir, and I Cespedes. Noise reduction in elastograms using temporal stretching with multicompression averaging. *Ultrasound in Medicine & Biology*, 22(8):1043–1052, 1996.

[33] Tomy Varghese and Jonathan Ophir. Enhancement of echo-signal correlation in elastography using temporal stretching. *Ultrasonics, Ferroelectrics, and Frequency Control, IEEE Transactions on*, 44(1):173–180, 1997.

[34] Hyock-Ju Kwon, Allan D Rogalsky, Christopher Kovalchick, and Guruswami Ravichandran. Application of digital image correlation method to biogel. *Polymer Engineering & Science*, 50(8):1585–1593, 2010.

[35] Dongsheng Zhang and Dwayne D Arola. Applications of digital image correlation to biological tissues. *Journal of Biomedical Optics*, 9(4):691–699, 2004.

[36] Francesco Viola and William F Walker. A comparison of the performance of time-delay estimators in medical ultrasound. *Ultrasonics, Ferroelectrics, and Frequency Control, IEEE Transactions on*, 50(4):392–401, 2003.

[37] John P Lewis. Fast template matching. In *Vision Interface*, volume 95, pages 15–19. Canadian Image Processing and Pattern Recognition Society, 1995.

[38] Hyock-Ju Kwon and Jiwon Lee. Low-cost quasi-real-time elastography using b-mode ultrasound images. *Bio-Medical Materials and Engineering*, 24(4):1673–92, 2014.

[39] PNT Wells. Doppler ultrasound in medical diagnosis. *The British journal of radiology*, 62(737):399–420, 1989.

[40] David H Evans. *Doppler Ultrasound: Physics, Instrumentation, and Clinical Applications*. John Wiley & Sons, 1989.

[41] Andreas Heimdal, Asbjørn Støylen, Hans Torp, and Terje Skjærpe. Real-time strain rate imaging of the left ventricle by ultrasound. *Journal of the American Society of Echocardiography*, 11(11):1013–1019, 1998.

[42] Thomas Kristoffersen Børstad. Intraoperative ultrasound strain imaging of brain tumors. 2011.

[43] Jørgen Grythe. Improving elastography using surf imaging for suppression of reverberations. 2010.

[44] Andreas Pesavento, Christian Perrey, Martin Krueger, and Helmut Ermert. A time-efficient and accurate strain estimation concept for ultrasonic elastography using iterative phase zero estimation. *Ultrasonics, Ferroelectrics, and Frequency Control, IEEE Transactions on*, 46(5):1057–1067, 1999.

[45] TDMM Shiina, MM Doyley, and JC Bamber. Strain imaging using combined rf and envelope autocorrelation processing. In *Ultrasonics Symposium, 1996. Proceedings., 1996 IEEE*, volume 2, pages 1331–1336. IEEE, 1996.

[46] Unmin Bae and Yongmin Kim. Angular strain estimation method for elastography. *Ultrasonics, Ferroelectrics, and Frequency Control, IEEE Transactions on*, 54(12), 2007.

[47] M O'Donnell, AR Skovoroda, and BM Shapo. Measurement of arterial wall motion using Fourier bases speckle tracking algorithms. In *Ultrasonics Symposium*, volume 1, pages 1101–1101. Citeseer, 1991.

[48] GM Treece, JE Lindop, AH Gee, and RW Prager. Efficient elimination of dropouts in displacement tracking. *Ultrasonic Measurement and Imaging of Tissue Elasticity*, 2006.

[49] Yougun Han. Development of methodologies for strain measurement and surface energy characterization. Master's thesis, University of Waterloo, 2011.

[50] Jonathan Ophir, Faouzi Kallel, Tomy Varghese, Michel Bertrand, Ignacio Cespedes, and Hari Ponnekanti. Elastography: A systems approach. *International Journal of Imaging Systems and Technology*, 8(1):89–103, 1997.

[51] Tomy Varghese and Jonathan Ophir. A theoretical framework for performance characterization of elastography: The strain filter. *Ultrasonics, Ferroelectrics, and Frequency Control, IEEE Transactions on*, 44(1):164–172, 1997.

[52] Jonathan Ophir, S Kaisar Alam, Brian Garra, F Kallel, E Konofagou, T Krouskop, and T Varghese. Elastography: ultrasonic estimation and imaging of the elastic properties of tissues. *Proceedings of the Institution of Mechanical Engineers, Part H: Journal of Engineering in Medicine*, 213(3):203–233, 1999.

[53] Mehmet Bilgen and Michael F Insana. Error analysis in acoustic elastography. ii. strain estimation and snr analysis. *The Journal of the Acoustical Society of America*, 101(2):1147–1154, 1997.

[54] William D Barber, Jeffrey W Eberhard, and Steven G Karr. A new time domain technique for velocity measurements using doppler ultrasound. *Biomedical Engineering, IEEE Transactions on*, BME-32(3):213–229, 1985.

[55] J-Y David, Steven A Jones, and Don P Giddens. Modern spectral analysis techniques for blood flow velocity and spectral measurements with pulsed doppler ultrasound. *IEEE transactions on Biomedical Engineering*, 38(6):589–596, 1991.

[56] LS Wilson. Description of broad-band pulsed doppler ultrasound processing using the two-dimensional Fourier transform. *Ultrasonic Imaging*, 13(4):301–315, 1991.

[57] Thanasis Loupas, JT Powers, and Robert W Gill. An axial velocity estimator for ultrasound blood flow imaging, based on a full evaluation of the doppler equation by means of a two-dimensional autocorrelation approach. *Ultrasonics, Ferroelectrics, and Frequency Control, IEEE Transactions on*, 42(4):672–688, 1995.

[58] Thanasis Loupas and Robert W Gill. Multifrequency doppler: improving the quality of spectral estimation by making full use of the information present in the backscattered rf echoes. *Ultrasonics, Ferroelectrics, and Frequency Control, IEEE Transactions on*, 41(4):522–531, 1994.

[59] Jørgen Arendt Jensen and Niels Bruun Svendsen. Calculation of pressure fields from arbitrarily shaped, apodized, and excited ultrasound transducers. *Ultrasonics, Ferroelectrics, and Frequency Control, IEEE Transactions on*, 39(2):262–267, 1992.

[60] Jørgen Arendt Jensen. Field: A program for simulating ultrasound systems. In *10TH NORDICBALTIC CONFERENCE ON BIOMEDICAL IMAGING, VOL. 4, SUPPLEMENT 1, PART 1*, pages 351–353. Citeseer, 1996.

[61] Ernest L Madsen, James A Zagzebski, and Gary R Frank. An anthropomorphic ultrasound breast phantom containing intermediate-sized scatteres. *Ultrasound Med. Bio.*, 8(4):381–392, 1982.

[62] Claude Elwood Shannon. Communication in the presence of noise. *Proceedings of the IRE*, 37(1):10–21, 1949.

[63] Michael Unser. Sampling-50 years after shannon. *Proceedings of the IEEE*, 88(4):569–587, 2000.

[64] Tal Shimon Schwartz. Data-guided statistical sparse measurements modeling for compressive sensing. 2013.

[65] Harry Nyquist. Certain topics in telegraph transmission theory. *Transactions of the American Institute of Electrical Engineers*, 47(2):617–644, 1928.

[66] Mark A Davenport, Marco F Duarte, Yonina C Eldar, and Gitta Kutyniok. Introduction to compressed sensing. *Preprint*, 93(1):2, 2011.

[67] Emmanuel J Candes, Justin K Romberg, and Terence Tao. Stable signal recovery from incomplete and inaccurate measurements. *Communications on Pure and Applied Mathematics*, 59(8):1207–1223, 2006.

[68] Emmanuel J Candès and Michael B Wakin. An introduction to compressive sampling. *IEEE Signal Processing Magazine*, 25(2):21–30, 2008.

[69] Michael Lustig, Juan M Santos, Jin-Hyung Lee, David L Donoho, and John M Pauly. Application of compressed sensing for rapid mr imaging. *SPARS,(Rennes, France)*, 2005.

[70] Joshua Trzasko and Armando Manduca. Highly undersampled magnetic resonance image reconstruction via homotopic l0-minimization. *IEEE Transactions on Medical imaging*, 28(1):106–121, 2009.

[71] Sara Klingenberg Mollenbach and Jorgen Arendt Jensen. Duplex scanning using sparse data sequences. In *Ultrasonics Symposium, 2008. IUS 2008. IEEE*, pages 5–8. IEEE, 2008.

[72] Guang-Hong Chen, Jie Tang, and Shuai Leng. Prior image constrained compressed sensing (piccs): a method to accurately reconstruct dynamic ct images from highly undersampled projection data sets. *Medical Physics*, 35(2):660–663, 2008.

[73] Zijian Guo, Changhui Li, Liang Song, and Lihong V Wang. Compressed sensing in photoacoustic tomography in vivo. *Journal of Biomedical Optics*, 15(2):021311–021311, 2010.

[74] Alfred M Bruckstein, Michael Elad, and Michael Zibulevsky. On the uniqueness of nonnegative sparse solutions to underdetermined systems of equations. *IEEE Transactions on Information Theory*, 54(11):4813–4820, 2008.

[75] David L Donoho and Xiaoming Huo. Uncertainty principles and ideal atomic decomposition. *IEEE Transactions on Information Theory*, 47(7):2845–2862, 2001.

[76] Michael Elad and Alfred M Bruckstein. A generalized uncertainty principle and sparse representation in pairs of bases. *IEEE Transactions on Information Theory*, 48(9):2558–2567, 2002.

[77] Joel A Tropp. Greed is good: Algorithmic results for sparse approximation. *IEEE Transactions on Information Theory*, 50(10):2231–2242, 2004.

[78] Joel A Tropp. Just relax: Convex programming methods for identifying sparse signals in noise. *IEEE Transactions on Information Theory*, 52(3):1030–1051, 2006.

[79] Mohammadreza Balouchestani, Kaamran Raahemifar, and Sridhar Krishnan. New sampling approach for wireless ecg systems with compressed sensing theory. In *Medical Measurements and Applications Proceedings (MeMeA), 2013 IEEE International Symposium on*, pages 213–218. IEEE, 2013.

[80] Hervé Liebgott, Rémy Prost, and Denis Friboulet. Pre-beamformed rf signal reconstruction in medical ultrasound using compressive sensing. *Ultrasonics*, 53(2):525–533, 2013.

[81] Oana Lorintiu, Hervé Liebgott, and Denis Friboulet. Compressed sensing doppler ultrasound reconstruction using block sparse bayesian learning. *IEEE Transactions on Medical Imaging*, 35(4):978–987, 2016.

[82] Emmanuel J Candès, Justin Romberg, and Terence Tao. Robust uncertainty principles: Exact signal reconstruction from highly incomplete frequency information. *IEEE Transactions on Information Theory*, 52(2):489–509, 2006.

[83] Joel A Tropp and Anna C Gilbert. Signal recovery from random measurements via orthogonal matching pursuit. *IEEE Transactions on Information Theory*, 53(12):4655–4666, 2007.

[84] Emmanuel J Candès and Terence Tao. Decoding by linear programming. *IEEE Transactions on Information Theory*, 51(12):4203–4215, 2005.

[85] Emmanuel J Candès. The restricted isometry property and its implications for compressed sensing. *Comptes Rendus Mathematique*, 346(9-10):589–592, 2008.

[86] Zhilin Zhang, Tzyy-Ping Jung, Scott Makeig, and Bhaskar D Rao. Compressed sensing for energy-efficient wireless telemonitoring of noninvasive fetal ecg via block sparse bayesian learning. *IEEE Transactions on Biomedical Engineering*, 60(2):300–309, 2013.

[87] Emmanuel J Candes, Yonina C Eldar, Deanna Needell, and Paige Randall. Compressed sensing with coherent and redundant dictionaries. *Applied and Computational Harmonic Analysis*, 31(1):59–73, 2011.

[88] Mohammed M Abo-Zahhad, Aziza I Hussein, and Abdelfatah M Mohamed. Compressive sensing algorithms for signal processing applications: A survey. *International Journal of Communications, Network and System Sciences*, 8(06):197, 2015.

[89] Laurent Demanet and Lexing Ying. Wave atoms and sparsity of oscillatory patterns. *Applied and Computational Harmonic Analysis*, 23(3):368–387, 2007.

[90] Laurent Demanet and Lexing Ying. Wave atoms and time upscaling of wave equations. *Numerische Mathematik*, 113(1):1–71, 2009.

[91] Emmanuel Candes and Justin Romberg. l1-magic: Recovery of sparse signals via convex programming. *URL: www. acm. caltech. edu/l1magic/downloads/l1magic. pdf*, 4:14, 2005.

[92] Robert Tibshirani. Regression shrinkage and selection via the lasso. *Journal of the Royal Statistical Society. Series B (Methodological)*, pages 267–288, 1996.

[93] Emmanuel Candes and Terence Tao. The dantzig selector: Statistical estimation when p is much larger than n. *The Annals of Statistics*, pages 2313–2351, 2007.

[94] Jarvis Haupt and Robert Nowak. Signal reconstruction from noisy random projections. *IEEE Transactions on Information Theory*, 52(9):4036–4048, 2006.

[95] Zhilin Zhang and Bhaskar D Rao. Extension of sbl algorithms for the recovery of block sparse signals with intra-block correlation. *IEEE Transactions on Signal Processing*, 61(8):2009–2015, 2013.

[96] Lili Yuan and Peder C Pedersen. Analytical phase-tracking-based strain estimation for ultrasound elasticity. *Ultrasonics, Ferroelectrics, and Frequency Control, IEEE Transactions on*, 62(1):185–207, 2015.

[97] RK Rao Yarlagadda, Radha Krishna Rao Yarlagadda, and Radha Krishna Rao Yarlagadda. *Analog and digital signals and systems*, volume 1. Springer, 2010.

[98] Daniel Zwillinger. *CRC standard mathematical tables and formulae*. CRC press, 2002.

[99] Bany H Friemel, Laurence N Bohs, and Gregg E Trahey. Relative performance of two-dimensional speckle-tracking techniques: normalized correlation, non-normalized correlation and sum-absolute-difference. In *Ultrasonics Symposium, 1995. Proceedings., 1995 IEEE*, volume 2, pages 1481–1484. IEEE, 1995.

[100] Travis Wiens and Stuart Bradley. A comparison of time delay estimation methods for periodic signals. *Digital Signal Processing, submitted September*, 2009.

[101] Jonathan Ophir, S Kaisar Alam, Brian S Garra, Faouzi Kallel, Elisa E Konofagou, Thomas Krouskop, Christopher RB Merritt, Raffaella Righetti, Remi Souchon, Seshadri Srinivasan, et al. Elastography: imaging the elastic properties of soft tissues with ultrasound. *Journal of Medical Ultrasonics*, 29(4):155–171, 2002.

[102] AR Skovoroda, AN Klishko, DA Gusakyan, Ye I Mayevskii, VD Yermilova, GA Oranskaya, and AP Sarvazyan. Quantitative analysis of the mechanical characteristics of pathologically changed soft biological tissues. *Biophysics*, 6(40):1359–1364, 1995.

[103] Graham Treece, Joel Lindop, Lujie Chen, James Housden, Richard Prager, and Andrew Gee. Real-time quasi-static ultrasound elastography. *Interface focus*, 1(4):540–552, 2011.

[104] Jonathan F Carlsen, Caroline Ewertsen, Lars Lönn, and Michael B Nielsen. Strain elastography ultrasound: an overview with emphasis on breast cancer diagnosis. *Diagnostics*, 3(1):117–125, 2013.

[105] Stian Langeland, Jan Dhooge, H Torp, Bart Bijnens, and Paul Suetens. Comparison of time-domain displacement estimators for two-dimensional rf tracking. *Ultrasound in Medicine & Biology*, 29(8):1177–1186, 2003.

[106] Peter NT Wells and Hai-Dong Liang. Medical ultrasound: imaging of soft tissue strain and elasticity. *Journal of the Royal Society Interface*, 8(64):1521–1549, 2011.

[107] Pawan Chaturvedi, Michael F Insana, and Timothy J Hall. Testing the limitations of 2-d companding for strain imaging using phantoms. *Ultrasonics, Ferroelectrics, and Frequency Control, IEEE Transactions on*, 45(4):1022–1031, 1998.

[108] Ignacio Céspedes and Jonathan Ophir. Reduction of image noise in elastography. *Ultrasonic Imaging*, 15(2):89–102, 1993.

[109] Peter Hoskins and Aline Criton. Colour flow and tissue imaging. *Diagnostic ultrasound physics and equipment, 2nd edn. Cambridge University Press, Cambridge*, pages 121–141, 2010.

[110] Hua Xie, Thomas Gauthier, and Anna T Fernandez. The role of local center frequency estimation in doppler-based strain imaging. In *Ultrasonics Symposium, 2007. IEEE*, pages 1965–1968. IEEE, 2007.

[111] A Papoulis. Probability, random variables and stochastic theory, 1984.

[112] Erwin Kreyszig. Advanced engineering mathematics. *Integration*, 9:4, 2008.

[113] Srikar Adhikari, Michael Blaivas, Matthew Lyon, and Stephen Shiver. Transfer of real-time ultrasound video of fast examinations from a simulated disaster scene via a mobile phone. *Prehospital and Disaster Medicine*, 29(03):290–293, 2014.

[114] João M Sanches, Jacinto C Nascimento, and Jorge S Marques. Medical image noise reduction using the sylvester–lyapunov equation. *Image Processing, IEEE Transactions on*, 17(9):1522–1539, 2008.

[115] S Sudha, GR Suresh, and R Sukanesh. Speckle noise reduction in ultrasound images by wavelet thresholding based on weighted variance. *International Journal of Computer Theory and Engineering*, 1(1):7–12, 2009.

[116] Damien Garcia. Robust smoothing of gridded data in one and higher dimensions with missing values. *Computational Statistics & Data Analysis*, 54(4):1167–1178, 2010.

[117] Grace Wahba. *Spline models for observational data*, volume 59. Siam, 1990.

[118] Howard L Weinert. Efficient computation for whittaker–henderson smoothing. *Computational Statistics & Data Analysis*, 52(2):959–974, 2007.

[119] Gilbert Strang. The discrete cosine transform. *SIAM review*, 41(1):135–147, 1999.

[120] Ali Baghani. A wave equation approach to ultrasound elastography. 2010.

[121] Ronald O Bude and Ronald S Adler. An easily made, low-cost, tissue-like ultrasound phantom material. *Journal of Clinical Ultrasound*, 23(4):271–273, 1995.

[122] Thomas L Szabo. *Diagnostic ultrasound imaging: inside out*. Academic Press, 2004.